Title
Coordination of escape circuits orchestrates versatile flight and controls escape vigor from multimodal threats

Author
Schuette, Peter Joseph

Publication Date
2022

Peer reviewed|Thesis/dissertation

UNIVERSITY OF CALIFORNIA

Los Angeles

Coordination of escape circuits orchestrates versatile flight and controls escape vigor from multimodal threats

A dissertation submitted in partial satisfaction of the

requirements for the degree Doctor of Philosophy

in Neuroscience

by

Peter Joseph Schuette

2022

ABSTRACT OF THE DISSERTATION

Coordination of escape circuits orchestrates

versatile flight and controls escape vigor from multimodal threats.

by

Peter Joseph Schuette

Doctor of Philosophy in Neuroscience

University of California, Los Angeles, 2022

Professor Avishek Adhikari, Co-Chair

Professor Jonathan Kao, Co-Chair

Naturalistic escape requires versatile context-specific flight with rapid evaluation of local geometry to identify and use efficient escape routes. It is unknown how spatial navigation and escape circuits are recruited to produce context-specific flight. Using mice, we show activity in cholecystokinin-expressing hypothalamic dorsal premammillary cells (PMd-cck) is sufficient and necessary for context-specific escape that adapts to each environment's layout. Contrastingly, numerous other nuclei implicated in flight only induced stereotyped panic-related escape. We reasoned the PMd can induce context-specific escape because it projects to both escape and spatial navigation nuclei. Indeed, activity in PMd-cck projections to thalamic spatial navigation circuits are only necessary for context-specific escape induced by moderate threats, but not panic-related stereotyped escape caused by perceived asphyxiation. Conversely, the PMd projection to the escape-inducing dorsal periaqueductal gray projection is necessary for all

escapes tested. Thus, PMd-cck controls versatile flight, engaging spatial navigation and escape circuits.

It is additionally unknown if a single circuit controls escape vigor from innate and conditioned threats. We further demonstrate that PMd-cck cells are activated during escape, but not other defensive behaviors. PMd-cck ensemble activity can also predict future escape. Furthermore, PMd inhibition decreases escape speed from both innate and conditioned threats. Inhibition of the PMd-cck projection to the dlPAG also decreased escape speed. Intriguingly, PMd-cck and dlPAG activity in mice showed higher mutual information during exposure to innate and conditioned threats. In parallel, human fMRI data show that a posterior hypothalamic-to-dlPAG pathway increased activity during exposure to aversive images, indicating that a similar pathway may possibly have a related role in humans. Our data identify the PMd-dlPAG circuit as a central node, controlling escape vigor elicited by both innate and conditioned threats.

The dissertation of Peter Joseph Schuette is approved.

Michael S. Fanselow

Sotiris Masmanidis

Alcino Jose Silva

Avishek Adhikari, Committee Co-Chair

Jonathan Kao, Committee Co-Chair

University of California, Los Angeles

2022

DEDICATION

This work is dedicated to my parents, Mary Jean and George Schuette, who have unflaggingly encouraged me through all of my pursuits–from the visual arts to music and science. They undertook heroic commutes on the New Jersey Turnpike to watch my newborn while I attended my first classes in experimental psychology at Hunter College. They transplanted from Baltimore to Los Angeles at the birth of my second son, and allowed me the extra time I needed to spend at the lab or the library. The list extends, endless and infinite, as does my love for each of them.

I dedicate this work to my wife, Madeline Davy, for inspiring me to follow my passions, as seemingly impractical as they might have seemed at the moment. I thank her for trusting me through the academic process and agreeing to this strange adventure on the west side of Los Angeles. And I am forever grateful for the time she spent with our two children when the world shut down. This research would have been impossible without her.

Lastly, I dedicate this work to my two sons, Samuel and Luca Schuette, for sharing their sublime humanity and reminding me that, sometimes, it's okay to stop making sense.

TABLE OF CONTENTS

LIST OF FIGURES

Chapter 1

ACKNOWLEDGEMENTS

I give my sincerest thanks to my co-advisors, Avi Adhikari and Jonathan Kao, who jointly guided me over the hurdles inherent to the publication process and taught me to be a scientist, finding meaning in mountains of data. With equal parts patience and persistence, Avi coached me in the many crucial facets of scientific discovery–from the initial 'poking' of the data to the clear and concise description of the results in text and figures. Jonathan showed tireless dedication to my analytical growth, always meeting me at my level of understanding and building from there.

I offer my deepest gratitude to my many collaborators in the Adhikari and Kao labs. Thanks to Weisheng Wang, Fernando Reis, Mimi La-Vu and Anita Torossian for the meticulous data collection and conceptual rigor you brought to our co-authored publications. I thank my committee members–Alcino Silva, Michael Fanselow and Sotiris Masmanidis–for their thoughtful comments and encouragement.

Regarding the dissertation manuscript, I would like to acknowledge that Chapters 1 and 2 are modified versions of the following published articles. All authors have consented to the inclusion of the work in this dissertation:

Wang W*, Schuette PJ*, Nagai J, Tobias BC, Cuccovia V Reis FM, Ji S, de Lima MAX, La-Vu MQ, Maesta-Pereira S, Chakerian M, Leonard SJ, Lin L, Severino AL, Cahill CM, Canteras NS, Khakh BS, Kao JC, Adhikari A. Coordination of escape and spatial navigation circuits orchestrates versatile flight from threats. Neuron. 2021 Jun 2;109(11):1848-1860. doi: 10.1016/j.neuron.2021.03.033.

Weisheng Wang*, Peter J. Schuette*, Mimi Q. La-Vu, Anita Torossian, Brooke Christine Tobias, Marta Čeko, Philip A. Kragel, Fernando Midea Cuccovia V. Reis, Shiyu Ji, Megha Sehgal, Sandra Maesta-Pereira, Meghmik Chakerian, Alcino J Silva, Newton S. Canteras, Tor D. Wager, Jonathan C. Kao, Avishek Adhikari. Dorsal premammillary projection to periaqueductal gray

controls escape vigor from innate and conditioned threats. Elife. 2021 Sep 1. doi: 10.7554/eLife.69178.

Finally, it is crucial to acknowledge the funding sources that made this work possible. The Interdepartmental Neuroscience Program at UCLA supported research and related travel. I received funding for this work from the National Science Foundation (NSF-GRFP DGE-1650604) and the UCLA Affiliates fellowship. Additionally, this work was supported by grants awarded to other lab members and affiliate labs, including the NIMH (R00 MH106649 and R01 MH119089, to Avi Adhikari), Brain and Behavior Research Foundation (Grants # 22663, 27654, 27780, and 29204 to respectively Avi Adhikari, Fernando Reis, Weisheng Wang and Jonathan Kao), the Achievements Rewards for College Scientists Foundation, NIMH (F31 MH121050-01A1 to Mimi La Vu) (MQL), the Hellman Foundation (to Avi Adhikari), and FAPESP (Research Grant #2014/05432–9 to Newton Canteras).

CURRICULUM VITAE

Education

Columbia University: B.A., visual arts major, 1998-2002

Hunter College: Postbaccalaureate studies in experimental psychology, 2013-2015

Academic Employment

09/15 – 09/17 Senior Research Associate

Laboratory of Neuromodulation and Neuroimaging; Director: Dr. Nanthia Suthana, UCLA, CA

09/14 – 7/15 Research Assistant

Laboratory of Visual Psychophysiology; Director: Dr. James Gordon, Hunter College, NY

Selected Publications

Peter J. Schuette*, Juliane M. Ikebara*, Sandra Maesta-Pereira, Anita Torossian , Ekayana Sethi , Alexandre H. Kihara, Jonathan C. Kao, Fernando MCV Reis, Avishek Adhikari. GABAergic CA1 neurons are more stable following context changes than glutamatergic cells. Submitted to Scientific Reports.

Wang W*, Schuette PJ*, Nagai J, Tobias BC, Cuccovia V Reis FM, Ji S, de Lima MAX, La-Vu MQ, Maesta-Pereira S, Chakerian M, Leonard SJ, Lin L, Severino AL, Cahill CM, Canteras NS, Khakh BS, Kao JC, Adhikari A. Coordination of escape and spatial navigation circuits orchestrates versatile flight from threats. Neuron. 2021 Jun 2;109(11):1848-1860.

Weisheng Wang*, Peter J. Schuette*, Mimi Q. La-Vu, Anita Torossian, Brooke Christine Tobias, Marta Čeko, Philip A. Kragel, Fernando Midea Cuccovia V. Reis, Shiyu Ji, Megha Sehgal, Sandra Maesta-Pereira, Meghmik Chakerian, Alcino J Silva, Newton S. Canteras, Tor D.

Wager, Jonathan C. Kao, Avishek Adhikari. Dorsal premammillary projection to periaqueductal gray controls escape vigor from innate and conditioned threats, Elife. 2021 Sep 1.

Fernando M.C.V. Reis*, Jinhan Liu*, Peter J. Schuette, Johannes Y Lee, Sandra Maesta-Pereira, Meghmik Chakerian, Weisheng Wang, Newton S Canteras, Jonathan C. Kao, Avishek Adhikari. Shared dorsal periaqueductal gray activation patterns during exposure to innate and conditioned threats, Journal of Neuroscience, 41 (25) 5399-5420.

Fernando MCV Reis*, Johannes Y Lee*, Sandra Maesta-Pereira, Peter J Schuette, Meghmik Chakerian, Jinhan Liu, Mimi Q La-Vu, Brooke C Tobias, Newton S Canteras, Jonathan C Kao, Avishek Adhikari. Dorsal Periaqueductal gray ensembles represent approach and avoidance states, eLife 2021; 10:e64934.

Peter J. Schuette*, Fernando M. C. V. Reis*, Sandra Maesta-Pereira, Meghmik Chakerian, Anita Torossian, Garrett J. Blair, Weisheng Wang, Hugh T. Blair, Michael S. Fanselow, Jonathan C. Kao, Avishek Adhikari, Long-Term Characterization of Hippocampal Remapping during Contextual Fear Acquisition and Extinction, Journal of Neuroscience 21 October 2020, 40 (43) 8329-8342.

Awards

Samuel Eiduson Student Lecture Award (2022)

Life Sciences Excellence in Research Award for a PhD Candidate (2021)

NSF Graduate Research Fellowships Program (2018)

UCLA Affiliates Fellowship (2018)

Graduated *cum laude*, Columbia University (2002)

INTRODUCTION

Chapter 1. Coordination of escape and spatial navigation circuits orchestrate versatile flight from threats.

Animals rapidly escape from imminent threats (Perusini and Fanselow 2015). Escape frequently occurs in complex contexts, in which animals quickly assess the local layout to find efficient flight paths (Blank 2018; Woodbury 1986; Hedenström and Rosén 2001; Heithaus et al. 2009). These escapes require context-specific plans and precise coordination of spatial navigation and flight to identify and use effective escape routes. For example, escaping a burning building requires rapid evaluation of the floor's architecture to locate and use the most direct route to safety (Kobes et al. 2010). Stereotyped actions such as aimless jumping and running do not allow escape in such situations. However, the majority of escape studies use simple environments (Xiong et al. 2015; Li et al. 2018; Lecca et al. 2017; Chou et al. 2018; Shang et al. 2018). In these assays, stereotyped actions such as running in any direction away from threat is often sufficient to reach safety. For instance, mice escaping a loud sound (Xiong et al. 2015) or a looming stimulus (Shang et al. 2018) in an empty box only have to run away from these stimuli in any direction. Contrary to escapes that require context-specific plans, flight in simple environments such as an empty box does not require sophisticated spatial navigation skills or any knowledge of the environment's layout. As escape is generally studied in simple environments, it is unknown how spatial navigation is integrated with escape to produce context-specific escape requiring flexible decision-making to identify efficient flight routes in complex environments.

The region most strongly implicated with escape is the brainstem dorsolateral gray (dlPAG) (Evans et al. 2018; Deng, Xiao, and Wang 2016). DLPAG activation causes flight, (Deng, Xiao, and Wang 2016), and dlPAG inhibition profoundly impairs threat-induced escape (Aguiar and Guimarães 2009). Excitatory inputs to the dlPAG, such as the superior colliculus also are critical for vital and rapid stimulus-driven escape (Evans et al. 2018; Kragel et al. 2019), but this behavior

does not require complex spatial navigation skills which are often necessary in flight occuring in naturalistic settings. Hypothalamic PAG inputs, such as the ventromedial and dorsomedial hypothalamus, also control flight (Johnson and Shekhar 2012; Johnson et al. 2008; L. Wang, Chen, and Lin 2015). However, the strongest hypothalamic projection to the dlPAG has not been investigated.

The largest hypothalamic input to glutamatergic flight-inducing dlPAG cells is the dorsal premammillary nucleus (PMd) (Tovote et al. 2016). PMd lesions impair predator-induced defense, and this region is strongly activated by escape-inducing threats (Cezario et al. 2008). The PMd's most remarkable feature is its unique connectivity, as it interfaces between spatial navigation and defensive circuits. Its two main outputs are the escape-inducing dlPAG and a navigation and memory -related structure named the anteromedial ventral thalamic nucleus (amv) (N. S. Canteras and Swanson 1992). Amv lesions impair spatial navigation and contextual memory (Jankowski et al. 2013). The amv also has cells that encode head direction (Bassett, Tullman, and Taube 2007) and projects to canonical navigation regions such as the entorhinal cortex and the subiculum (Jankowski et al. 2013). Considering the role of the PMd in defense, and its connectivity with defense and spatial navigation networks, we hypothesized the PMd orchestrates the coordination of contextual navigation and flight necessary for strategic context-specific escape.

In Chapter 1, we directly studied the role of cholecystokinin (cck)- expressing PMd cells in escape. We show PMd-cck cell activity is sufficient and necessary for both context-specific and stereotyped escape. In contrast, other hypothalamic nuclei only affected stereotyped defensive behaviors but not context-specific flight. Interestingly, PMd-cck cells recruit the amv only in tasks that require context-specific escape. In contrast, the PMd-cck projection to the dlPAG is necessary for both context-specific and stereotyped escapes. Thus, the PMd is the first identified

region that produces versatile context-specific flight by coordinated recruitment of escape and spatial navigation networks.

Chapter 2. Dorsal premammillary projection to periaqueductal gray controls escape vigor from innate and conditioned threats.

It has been shown that the dlPAG controls escape vigor, measured by escape velocity (Evans et al. 2018). However, inputs to the dlPAG that may control escape vigor have not been identified. The dorsomedial portion of the ventromedial hypothalamus (VMHdm) is a major excitatory dlPAG input, suggesting that the VMHdm projection may mediate escape. However, activation of the VMHdm projection to the dlPAG surprisingly causes freezing, not escape (L. Wang, Chen, and Lin 2015). The other main hypothalamic input to the dlPAG is the PMd (Tovote et al. 2016; N. S. Canteras and Swanson 1992). Surprisingly, despite being the strongest known input to the panicogenic dlPAG (Tovote et al. 2016; N. S. Canteras and Swanson 1992), the activity of this nucleus has not previously been directly manipulated or recorded.

The PMd is a key component of the hypothalamic defense system, and is strongly activated by various imminent threats (Cezario et al. 2008). Dangerous stimuli that activate the rodent PMd are extremely diverse, and include carbon dioxide (Johnson et al. 2011), several predators (cats, snakes and ferrets) (Mendes-Gomes et al. 2020) as well as aversive lights and noises (D. J. Kim et al. 2017). Additionally, the PMd is activated by contexts fear-conditioned with shocks (Newton S. Canteras et al. 2008) and social defeat (Faturi et al. 2014), indicating that it may play a role in coordinating defensive behaviors to both innate and conditioned threats. However, to date, the role of the PMd in escape vigor has not been directly studied. Furthermore, escape is generally studied during exposure to innate threats (Evans et al. 2018; Deng, Xiao, and Wang 2016). Consequently, it is not known if escape from innate and conditioned threats requires the same

circuit. Considering the PMd's involvement in innate and conditioned defense, as explained above, we predicted this region controlled escape from both threat modalities.

The vast majority of PMd cells are glutamatergic and express cholecystokinin (cck), and we show in Chapter 1 of this manuscript that these cells controlled versatile context-specific escape from innate threats (W. Wang et al. 2021). However, it is unknown if PMd-cck cells also control escape velocity. Considering the results discussed above, as well as prior reports showing the dlPAG controls escape vigor (Evans et al. 2018), we hypothesize that PMd-cck cells affect escape vigor via their projection to the dlPAG, but not the amv. Also, in Chapter 1 of this manuscript, we show that PMd-cck cells are active during escapes (W. Wang et al. 2021), but it remains unknown if these cells also encode or predict future occurrences of escape and other defensive behaviors, and whether they represent relevant metrics such as distance to threat. Lastly, it is unknown how this population is activated by conditioned threats and if PMd-cck cells affect defensive behaviors elicited by conditioned threats. To address these questions we explored if PMd-cck cell activity is necessary for defensive behaviors elicited by innate and conditioned threats (a live predatory rat and a shock grid, respectively) (Reis et al. 2021). We also characterized how PMd-cck cells represent these threats and defensive behaviors during threat exposure.

In Chapter 2, we show that PMd-cck cells encoded and predicted escape from innate and conditioned threats. Furthermore, inhibition of these cells or of their projection to the dlPAG decreased escape speed from a live predator and a conditioned threat (a shock grid). Lastly, fMRI data show that a hypothalamic-dlPAG pathway displays increased activation during exposure to aversive images, indicating that a similar pathway from a posterior medial hypothalamic nucleus to the brainstem may also exist in humans. These results show, for the first time, that the PMd is a vital node in coordinating escape from both innate and conditioned threats, and thus is likely to play key roles in minimizing exposure to danger.

RESULTS

Chapter 1. Coordination of escape and spatial navigation circuits orchestrate versatile flight from threats.

PMd controls context-specific escape.

In situ hybridizations show most PMd neurons expressed VGLUT2 (87%) and cholecystokinin (cck) (Figure 1.1A-D). GABAergic markers were not expressed in the PMd (1.1E-M). We used a cck-cre line to specifically target the PMd, as cck expression is more restricted to the PMd compared to VGLUT2. To bidirectionally control the activity of PMd-cck cells, we show that the ligand clozapine-n-oxide (CNO) respectively depolarized or hyperpolarized PMd-cck cells expressing hM3Dq or hM4Di (Figure 1.2A-B).

We next investigated if PMd activity modulates versatile context-specific escape induced by threats. We expressed DREADDs in PMd-cck cells (Figure 1.2C) and exposed mice to novel escape-inducing assays according to a planned timeline (Figure 1.2D). In the rat assay (Figure 1.2E), mice were placed in either the presence of an awake rat or a toy rat. To escape from the rat, mice found a ladder located in a corner and climbed it to access a safe burrow. After resting in the burrow for one-minute, mice were gently pushed to descend the ladder (Figure 1.2E). The number of escape climbs in 20 minutes were counted (the 20 minutes include the 1-min rest periods). We opted for climbing escape routes because, in order to escape, mice could only climb one specific location, requiring spatial navigation and a tridimensional understanding of the context. Mice are also less likely to use climbing routes by chance due to hyperlocomotion or other strategies without context-specific escape. Mice expressing hM3Dq, hM4Di or mcherry in PMd-cck cells were exposed twice to the rat and the toy rat after being treated with CNO or saline

in separate days. Chemogenetic inhibition and excitation of PMd-cck cells respectively decreased and increased the number of climbs away from the live rat (Figure 1.2F-G). These manipulations did not change behavior in the safe toy rat assay, indicating that PMd-cck cells are selectively controlling escape from threats, rather than generally increasing exploration (Figure 1.2F-G).

We next investigated how the PMd controlled escape induced by threats of different intensities in the same context. We developed two assays: exposure to a heated floor and CO_2. In the heated floor assay, mice climbed a cylinder wrapped in thin mesh to avoid a heated floor (43^{o}C) or an unheated control floor at room temperature (Figure 1.2H, left). Mice climbed down on their own. The number of climbs in 20 minutes was counted.

To measure panic-related stereotyped escape, (Blanchard, Griebel, and Blanchard 2001; Johnson et al. 2011) we counted the number of jumps in mice exposed to 15% CO_2 or air for 10 minutes (Figure 1.2H, right). Identical chambers containing the climbing escape route were used in the CO_2 and heated floor assays. We elicited panic with CO_2 rather than a higher heated temperature to avoid skin burns.

Mice mostly climbed in the rat and heated floor assays and jumped in the CO_2 test (Figure 1.2I). In the heated floor and rat assays, escaping from threats required knowledge of the contextual layout. Thus, climbing in the rat and heated floor assays was used as a measure of context-specific flight that requires spatial navigation in three dimensions. In contrast, jumping in the CO_2 assay did not use context-specific escape, as mice aimlessly jumped from anywhere. The interval between climbing escapes in rat and heated floor assays was higher than between jumps in CO_2, in agreement with the view that panic jumping may be a more reflexive escape than climbing. In both assays, climbing provided longer relief from the threat, as mice could decrease threat exposure for as long as they clinged on the climbing route and remained far from the heated floor

or from the highest CO_2 concentration at the bottom (Figure 1.2J). Indeed, in the CO_2 assay, climbs provided longer-lasting avoidance of threat than jumps (Figure 1.2K). Though climbing provided more effective threat avoidance, exposure to the panicogenic agent CO_2 shifted behavior from context-specific climbs in the heated floor assay to panic-related jumps in the CO_2 assay (Figure 1.2I).

Chemogenetic inhibition and excitation of PMd-cck cells respectively decreased and increased escape attempts in both heated floor and CO_2 assays (Figure 1.2L-O, see also detailed time course in Figure 1.3A). Thus, PMd-cck activity is necessary and sufficient to control versatile context-specific flight and panic-related stereotyped escapes, which are caused respectively by moderate and high intensity threats. These results could not be attributed to changes in pain perception, anxiety or overall locomotion (Figure 1.3B-D). Compared to the rat, the toy rat elicited fewer escapes and less avoidance, demonstrating that the toy rat is an appropriate safe control stimulus Figure 1.4A-B).

We next investigated if context-specific escape is specific to the PMd or if it is also present in other hypothalamic nuclei involved in escape. Thus, we chemogenetically excited the dorsomedial hypothalamus, a nucleus that mediates panic-related escape (Johnson and Shekhar 2012; Johnson et al. 2008). This manipulation did not change context-specific climbs (Figure 1.4C). However, dorsomedial hypothalamic excitation increased panic-related stereotyped jumping in the CO_2 assay (Figure 1.4C), indicating it only controls stereotyped flight. We then activated the dorsomedial portion of the ventromedial hypothalamus (VMHdm). This nucleus is highly interconnected with the PMd (N. S. Canteras and Swanson 1992; Comoli, Ribeiro-Barbosa, and Canteras 2000) and activation of SF1-expressing VMHdm cells induces freezing and flight (L. Wang, Chen, and Lin 2015). Excitation of VMH-SF1 cells did not alter escape in any assay (Figure 1.4D). However, exciting these cells, but not the PMd-cck or dorsomedial hypothalamus-syn cells,

increased freezing in the rat assay (Figure 1.5, right), in agreement with the role of the VMHdm in predator-induced defense (Martinez et al. 2008; Silva et al. 2016). Thus, excitation of the DMH and the VMHdm did not induce context-specific escapes.

Dorsal premammillary nucleus (PMd) activation induced context-specific escape,

We next investigated the effects of optogenetic activation of PMd-cck cells in contexts requiring distinct strategies to escape (Figure 1.6B). Optogenetic activation of PMd-cck cells (20 Hz, Figure 1.6A and Figure 1.6A-C) in an empty box elicited running and jumping (Figure 1.6C upper panel, Figure 1.7D-E), but not freezing, even at lower stimulation intensities (Figure 1.7E). When mice were placed in the same box in the presence of a rope or a series of blocks that could be climbed to allow escape (Figure 1.6B), PMd-cck stimulation did not cause jumping. Instead, it caused escape through the newly provided escape routes. All PMd-cck ChR2 mice escaped using these diverse new routes within 30 seconds of optogenetic stimulation without any prior training (Figure 1.6C, 2nd and 3rd panels). Thus, PMd-cck stimulation created context-specific flight, even in unfamiliar and complex environments. In contrast, activation of ChR2-expressing VMHdm SF1 cells increased escape jumps, but did not consistently produce escape from the complex upwards step box (Figure 1.4E-G).

To identify other regions that may control context-specific escape, we optogenetically activated numerous hypothalamic and brainstem nuclei that showed threat-induced increases in fos expression (Figure 1.8A-B). Activation of several nuclei induced jumping and freezing (Figure 1.8D and 1.9A-D). Remarkably, among 7 tested nuclei, only PMd optogenetic activation induced escape from the upwards step box (Figure 1.8F), even though animals had no prior exposure to this box (Figure 1.8E). In contrast, dlPAG activation did not induce escape from the complex upwards step box with low or high light power optogenetic stimulation (Figure 1.8G). In a box with

two context-specific escape routes, PMd stimulation induced actions that quickly adapted to allow escape, even if the number and type of escape routes were changed. Thus, PMd stimulation flexibly induced escape in rapidly changing environments.

PMd activation induced aversion and autonomic activation

To study if PMd-cck stimulation is aversive, we tested whether PMd-cck ChR2 mice nose-poked to stop optogenetic stimulation. Mice received optogenetic stimulation until they nose-poked. This halted stimulation for 5 seconds, after which stimulation resumed until another nose poke occured. Data was collected for 10 minutes following 2 minutes of habituation and without any pre-training. Blue light power in the nose poke test was lower than that used in escape assays (Figure 1.6C) to avoid overt escape (see Methods). Mice expressing ChR2-YFP, but not YFP, in PMd-cck cells learned to nose-poke to avoid PMd-cck stimulation (Figure 1.6D). Importantly, PMd-cck ChR2 mice did not nose poke more than YFP mice in an inactive nose poke that did not halt optogenetic stimulation (Figure 1.7G). PMd-cck stimulation also caused avoidance in a real-time place preference task (Figure 1.6E-F). This avoidance persisted for 10 minutes following the end of the stimulation, suggesting PMd-cck activation produced an aversive memory. Optogenetic activation of PMd-cck cells also increased pupil size, heart rate and respiration rate (Figure 1.6G-I). Thus, PMd-activation induced behavioral, psychological and physiological symptoms associated with threat exposure.

PMd-cck cells encode escape induced by multiple threat modalities

Our results show PMd-cck activity is necessary and sufficient for escape from numerous threats (Figure 1.2), suggesting these cells may encode escape. We thus performed one-photon imaging in PMd-cck cells expressing the Ca^{2+} indicator GCaMP6s (Figure 1.10A-C) to extract activity from

PMd-cck cell ensembles (Figure 1.10D-E). Importantly, the number of escapes observed in mice with microscope implants (Figure 1.10F) was not different from control unimplanted mice (rat p=0.723, heated plate p=0.439, CO_2 p=0.291).

We used a hidden Markov Model (HMM) to identify the two most prominent network states in these data. The HMM was chosen for its simplicity and ability to model the latent processes, or 'hidden states,' of sequential data. As an unsupervised technique, it identifies states that are strongly represented in the data without using a teaching signal. This method separated different time points of the neural data into distinct states without any input about escapes. The neural data was the only provided input to the model. Remarkably, this method detected ensemble states that were highly predictive of escape occurrence in all three escape assays (Figure 1.10G-H), indicating that the most prominent state motifs are related to escape behavior. Similar results were found with different methods and parameters, including *k*-means clustering, an unsupervised approach that is arguably simpler than HMM for its exclusion of data sequentiality, and 5-fold logistic regression, one of the simplest supervised modeling methods (Figure 1.11A-C). These converging results show the findings are robust across model selection and indicate escape-related state encoding is a prominent feature of PMd-cck ensemble activity. Indeed, cells were active both before and after escape in each assay (Figure 1.10I). Furthermore, a high fraction of cells were significantly activated during escape (Figure 1.10J). Cells were classified as escape-activated if their weight for escape in a generalized linear model was higher than expected by chance compared to a bootstrap distribution (see Methods, “Escape cell classification”). These cells were used in Figure 1.10J-M. Fluorescence traces from these significantly escape-activated cells peaked either before (green) or after (yellow) the onset of escape (Figure 1.10K-L). Strikingly, the proportion of peaks occurring prior to escape onset was higher for the rat and heated floor assays than during CO_2 exposure (Figure 1.10M). These data demonstrate that PMd-

cck cells are engaged more strongly prior to context-specific escapes than to panic-related jumping.

Miniscope-implanted mice did not consistently display climbing in control assays, precluding comparisons of cell activity during climbs in control and threat contexts. PMd activation was not observed during other behaviors, such as running or risk-assessment stretch-attend postures (Figure 1.11D), showing PMd activation is selectively linked to escape. Lastly, though jumps were more common, a few climbs were seen in the CO_2 assay. Forty-seven % of cells activated by climb in CO_2 were not activated during jumps. Moreover, exclusive climb-categorized cells tended to exhibit more pre- versus post-escape Ca^{2+} transients than exclusive jump-categorized cells (Fig 1.11E, right), indicating a population of PMd cells is selectively activated during context-specific escape.

PMd-cck synchronizes with dlPAG in all escapes and with thalamic amv nucleus only during context-specific escape

We next investigated the PMd-cck outputs that mediate escape. The two main targets of the PMd are the dorsolateral periaqueductal gray (dlPAG) and the anteromedial ventral thalamus (amv) (N. S. Canteras and Swanson 1992). The dlPAG controls escape in general (Del-Ben and Graeff 2009; Tovote et al. 2016). The amv has head direction cells (Bassett, Tullman, and Taube 2007), is involved in spatial navigation and projects to navigation regions such as the entorhinal cortex and subiculum (Jankowski et al. 2013). We thus hypothesized the PMd-dlPAG projection is necessary for all escapes, while the PMd projection to amv is involved in escape requiring spatial navigation, but not in panic-related jumping.

As prior PMd connectivity studies were performed without cell-type specificity, it is unclear if PMd-cck cells project to the dlPAG and amv. Following injection of retrobeads in the dlPAG, 94% of

PMd-cck cells were retrogradely labeled (Figure 1.12A-E). Additionally, in an *ex vivo* slice preparation, all recorded dlPAG cells (*n*=9) showed glutamatergic monosynaptic glutamatergic excitatory responses following optogenetic stimulation of ChR2-expressing PMd-cck axon terminals (Figure 1.12F-J). A smaller fraction of PMd cells projected to the amv, and the majority (98%) of amv-projecting PMd cells also projected to the dlPAG (Figure 1.13A-B). In the PMd, 53% of cells project only to dlPAG and 46% of cells project to both amv and dlPAG (Figure 1.13C). Thus, there are two major PMd populations: one projects exclusively to dlPAG and another that projects to both amv and dlPAG.

We next investigated the neural activity of these circuits with dual-site GCaMP6s fiber photometry recordings in the PMd-cck and dlPAG-synapsin cells (Figure 1.14A-C). These two populations showed increased correlation in activity during exposure to all three threats relative to control stimuli (Figure 1.14D-F). In contrast, PMd-cck and amv-synapsin activity were more correlated relative to control assays only in the rat and heated floor assays (Figure 1.14G-K). The correlation between the activity of these two regions had a trending decrease in the CO_2 assay (Figure 1.14K). These data suggest the PMd-cck to dlPAG projection may broadly elicit threat-induced flight. Conversely, functional connectivity in the PMd-cck-amv circuit increases selectively in assays with context-specific escape, but not during panic-induced jumps (Figure 1.14K), in line with work showing the dlPAG and amv are respectively implicated in initiating escape (Tovote et al. 2016) and in spatial navigation (Jankowski et al. 2013). Activity in all three regions also increased prior to escape during exposure to all threat assays (Figure 1.15). The slow temporal dynamics of GCaMP did not allow for the identification of a PMd-dlPAG conduction lag, as hypothalamic-PAG lags may be shorter than 15 ms (Behbehani, Park, and Clement 1988; Sakuma and Pfaff 1982).

PMd projection to thalamus is necessary only for context-specific escape, while the projection to dlPAG is required for all escapes

The photometry results (Figure 1.14F and 1.14K) indicate that PMd-cck cells projecting to the amv become selectively activated only during context-specific escapes. Conversely, PMd input to the dlPAG may be engaged during all escapes. To test these hypotheses, we recorded Ca^{2+} transients in GCaMP6s-expressing PMd-cck axon terminals (Figure 1.16A-B). Axons terminating in amv were activated only during the rat and heated plate climb escapes, but not during jumping elicited by CO_2. In contrast, axons terminating in the dlPAG were activated during escape in all assays (Figure 1.16C-D). Furthermore, relative to control assays, PMd-cck axons terminating in the amv displayed larger fluorescence peaks during the rat and heated plate assays, but not the CO_2 assay (Figure 1.16E). In contrast, axons terminating in the dlPAG showed increased activation relative to control assays in all three paradigms (Figure 1.16E). These data show amv-projecting PMd cells are a population that is selectively activated only during context-specific flight, but not panic-related jumping.

We thus hypothesized that the activity of the PMd cck-dlPAG circuit is broadly necessary for flight, while the PMd-amv projection is specifically necessary for escape requiring spatial navigation. To test these hypotheses, we expressed Arch in PMd-cck cells and delivered green light (532 nm) to PMd-cck Arch-expressing axon terminals in the dlPAG or the amv. Inhibition of the PMd-cck to dlPAG projection (Figure 1.17A) decreased escape caused by all threats (Figure 1.17B). Inhibition of PMd-cck terminals in the amv (Figure 6C) only decreased escape in the rat and heated floor assays (Figure 1.17D), but did not affect stereotyped jumping in the CO_2 assay (Figure 1.17D). These data indicate that the PMd-dlPAG projection is broadly necessary for escape, while the PMd-amv circuit is selectively engaged during context-specific escape.

FIGURES

Chapter 1: Coordination of escape and spatial navigation circuits orchestrate versatile flight from threats.

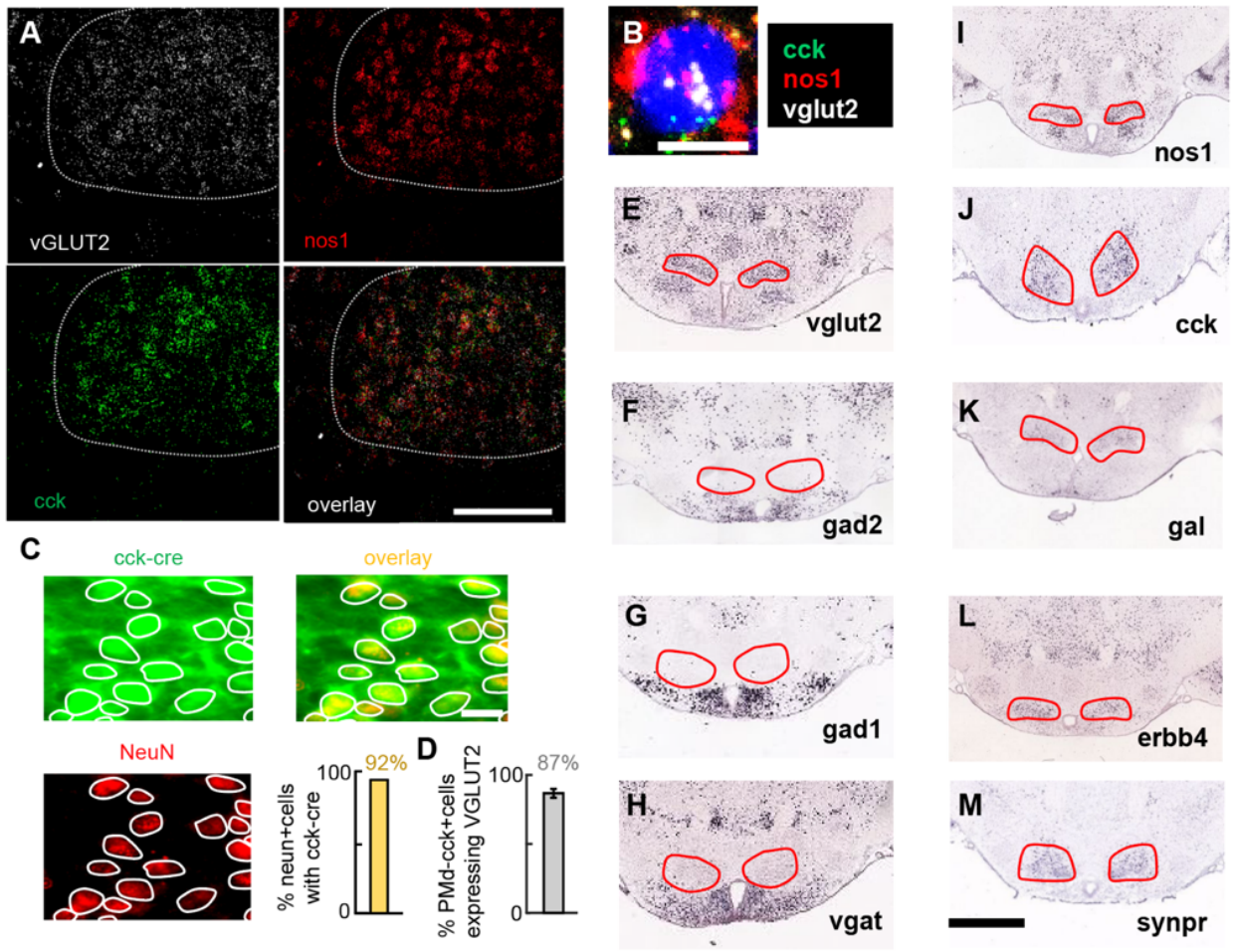

Figure 1.1. PMd cells express VGLUT2 and cck.
(A) In situ hybridizations in the PMd (PMd boundaries are shown in white dashed line) show high expression of vglut2, nos1 and cck. Scale bar: bars represent 150 μm. (B) Example neuron showing co-localization of all 3 markers. (scale bar: 10 μm) (C) cck-cre mice were injected with AAV9-EF1a-DIO-YFP in the PMd. The images show the high degree of co-localization between YFP expression and the pan-neuronal marker NeuN, indicating that the majority of PMd neurons express cck. Scale bar: 20 μm. (D) Bar depicts the percent of PMd-cck+ cells that express VGLUT2. (E-H) Images from the Allen Brain Institute gene expression database showing that glutamatergic, but not GABAergic markers are expressed in the PMd. (I-M). Genes highly expressed in the PMd include nos1, cck, gal (galanin), erbb4 and synpr.

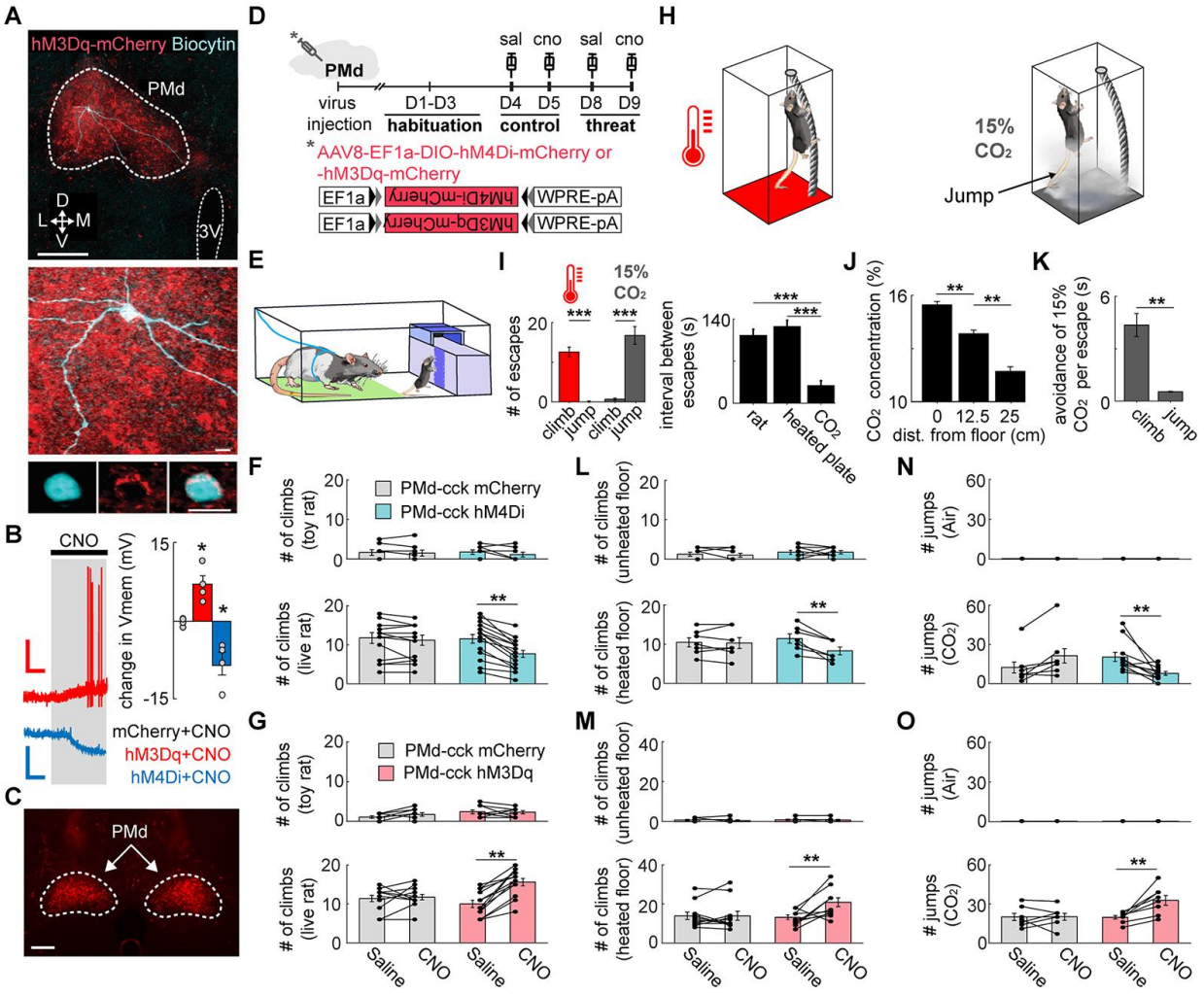

Figure 1.2. PMd-cck cells are necessary and sufficient to control context-specific and panic-related stereotyped escape.

(A) Ex vivo slices with cholecystokinin (cck) positive dorsal premammillary nucleus (PMd) cells expressing hM3Dq or hM4Di. Image shows biocytin-filled PMd-cck neuron (blue) and hM3Dq (red). (top scale bar: 200 μm; bottom scale bars: 10 μm) (B) (left) PMd-cck cells expressing hM3Dq and hM4Di receptors respectively de- and hyper-polarize with clozapine-N-oxide (CNO, 5μM). Scale bars: (red) 60s, 20 mV, (blue) 60s, 10 mV. (right) Average changes in membrane potential following CNO treatment. (mCherry n=4; hM3Dq n=4; hM4Di n=4 cells, 2 cells per mouse; one-way ANOVA followed by Tukey's test, *p<0.05) (C) Expression of hM4Dq-mcherry in PMd-cck cells for a mouse used in behavioral assays. (scale bar: 200 μm) (D) Timeline for each DREADD assay. (E) Rat assay scheme: mice were placed in the presence of an awake rat, restrained by harness to the green area. To escape, mice located and climbed a ladder (dark purple) to access a burrow. After 1 minute, mice were gently pushed towards the bottom of the ladder. The number of climbs in 20 minutes was counted. (F) Climbs away from toy rat (top) (mCherry n=7, hM4Di n=7) or live rat (bottom) (mCherry n=14, hM4Di n=16) for mice expressing mCherry or hM4Di in PMd-cck cells following treatment with saline or CNO. (G) Same as (F), but

for mice expressing mCherry or hM3Dq in PMd-cck cells. (toy rat: mCherry n=11, hM3Dq n=11; rat: mCherry n=12, hM3Dq n=13) (F,G) Chemogenetic PMd-cck inhibition and excitation respectively decreased and increased the number of escapes from rat (Two-way repeated measures ANOVA followed by Wilcoxon test, **p < 0.01). (H) Schemes for heated floor and CO_2 assays. (heated floor, left) Mice climbed a cylindrical mesh to escape a 43ºC floor, returning to the floor spontaneously. (CO_2, right) Mice jumped in the presence of 15% CO_2. (I) (left) Mice climbed more from the heated floor and jumped more in CO_2 (heated plate n=18; CO_2 n=18, Wilcoxon signed-rank test). (right) Mean interval between escapes for all assays for saline YFP sessions (rat n=27, heated plate n=17, CO_2 n=14). (J) CO_2 concentration decreases with distance from the floor (n=5, Wilcoxon signed-rank test). (K) Bars show the avoidance duration for the 15% CO_2 assay for each escape behavior (climb and jump respectively n=7 and n=9, Wilcoxon signed-rank test). (L) Climbs away from unheated (top) (mCherry n=8, hM4Di n=8) or heated floor (bottom) (mCherry n=7, hM4Di n=7) during 20 minutes in mice expressing mCherry or hM4Di in PMd-cck cells following treatment with saline or CNO. (M) Same as (L), but for mice expressing mCherry or hM3Dq in PMd-cck cells (unheated floor: mCherry n=9, hM3Dq n=9; heated floor: mCherry n=11, hM3Dq n=11). (N) Number of jumps in 10 minutes for the same groups as in (I) during exposure to air (top) (mCherry n=9, hM4Di n=9) or carbon dioxide (bottom) (mCherry n=7, hM4Di n=11). (O) Number of jumps for the same groups as in (N) during exposure to air (top) or CO_2 (bottom) (Air: mCherry n=9, hM3Dq n=9; CO_2: mCherry n=7, hM3Dq n=8). (B, F-G, I-O) Mean ± SEM.

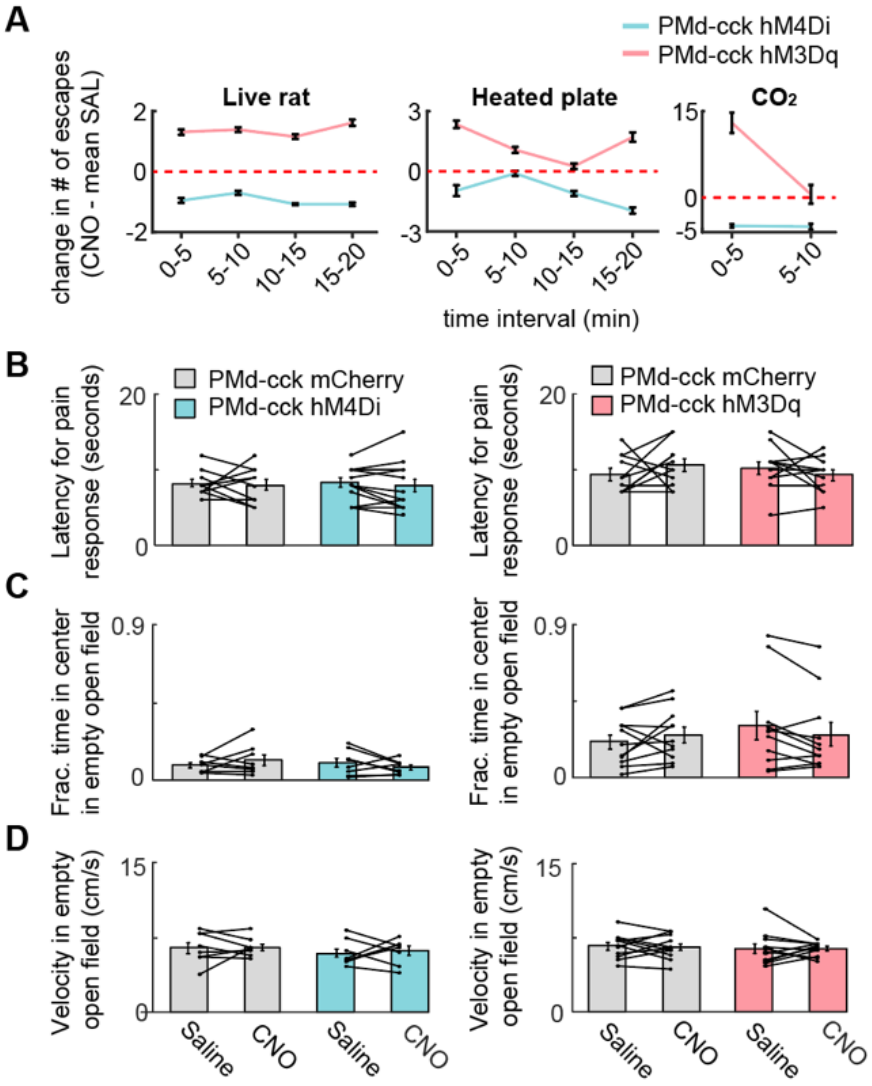

Figure 1.3. Chemogenetic manipulations in PMd-cck cells altered escape, but not pain sensitivity, anxiety or velocity.

(A) Lines show the change in the number of escapes (CNO - mean saline; +/- 1 s.e.m.) for the rat (left), heated plate (middle) and CO_2 (right) assays at consecutive time intervals. (live rat (hM4Di): mCherry n = 14, hM4Di n = 16; live rat (hM3Dq): mCherry n = 12, hM3Dq n = 13; heated floor (hM4Di): mCherry n = 7, hM4Di n = 7; heated floor (hM3Dq): mCherry n = 11, hM3Dq n = 11; CO_2 (hM4Di): mCherry n = 7, hM4Di n = 11; CO_2 (hM3Dq): mCherry n = 7, hM3Dq n = 8). (B) Mice were placed on a floor heated at 55^{O}C. The latency to show pain-related responses (jumping or paw-licking) was recorded, and then mice were moved back into their home cage. All mice displayed a pain-related response within 30 seconds. Mice-expressing hM4Di or hM3Dq in PMd-cck cells did not show altered pain responses in the hot plate test during treatment with CNO compared to saline treatment (mCherry/hM4Di n = 10, n = 13; mCherry/hM4Dq n = 11, n = 11). Mice-expressing hM4Di or hM3Dq in PMd-cck cells do not show changes in anxiety-related time

spent in center (C) or velocity (D) during treatment with CNO compared to saline treatment. (B-C) mCherry/hM4Di n = 8, n = 8; mCherry/hM4Dq n = 11, n = 11).

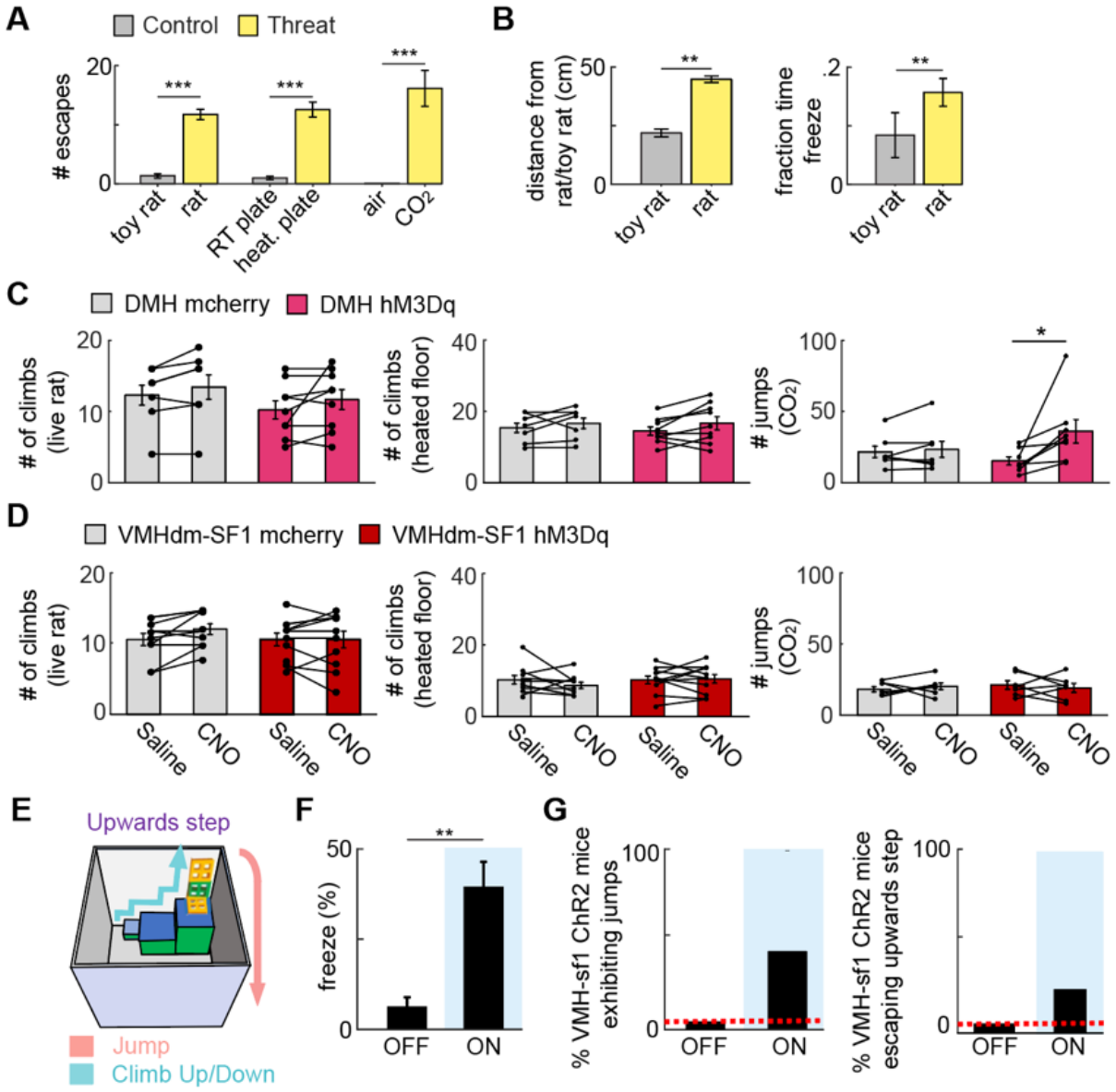

Figure 1.4. Chemogenetic excitation of dorsomedial and ventromedial hypothalamic nuclei do not elicit context-specific escape.

(A) Bars depict the number of escapes in each threat and related control assay for all mCherry saline sessions. (toy rat n=18; rat n=26; room temperature plate n=17; heated plate n=18; air n=18; CO_2 n=14)(Wilcoxon signed-rank test, ***p<0.001) (B) Bars depict the mean distance (left) of mice from the rat/toy rat and the fraction of time mice exhibited freezing behavior (right) in the rat/toy rat assays. (n same as (A)). (Wilcoxon signed-rank test, **p<0.01, ***p<0.001) (C) Mice were injected with AAV9-syn-mCherry or AAV9-syn-hM3Dq-mCherry in the dorsomedial hypothalamus (DMH). DMH-syn excitation only increased panic-related jumping to CO_2 (Two-way repeated measures ANOVA followed by Wilcoxon test, *p = 0.008), but not the more complex climbing escapes in the rat or heated floor assay. (live rat: mCherry n = 7, hM3Dq n = 9; heated

floor: mCherry n = 7, hM3Dq n = 9; CO_2: mCherry n = 7, hM3Dq n = 8). (D) Same as (C), but for but for mice injected with AAV8-EF1a-DIO-mCherry or AAV8-EF1a-DIO-hM3Dq-mCherry in the dorsomedial portion of the ventromedial hypothalamus (VMHdm) of SF1-cre mice. Excitation of VMHdm-SF1 cells did not increase escape in any assay tested. (live rat: n = 10 mCherry, 11 hM3Dq; heated plate: n = 10 mCherry, 11 hM3Dq; CO_2: n = 7 mCherry, 7 hM3Dq). (E) VMH-sf1 mice were optogenetically stimulated (3 mins OFF/3 mins ON/3 mins OFF) in the upwards step assay. (F) Bars show the % time freezing (n=5). (G) Bars depict (left) the number of mice to exhibit jumps and (right) escape the enclosure during light ON and light OFF (n=5). Mean ± SEM.

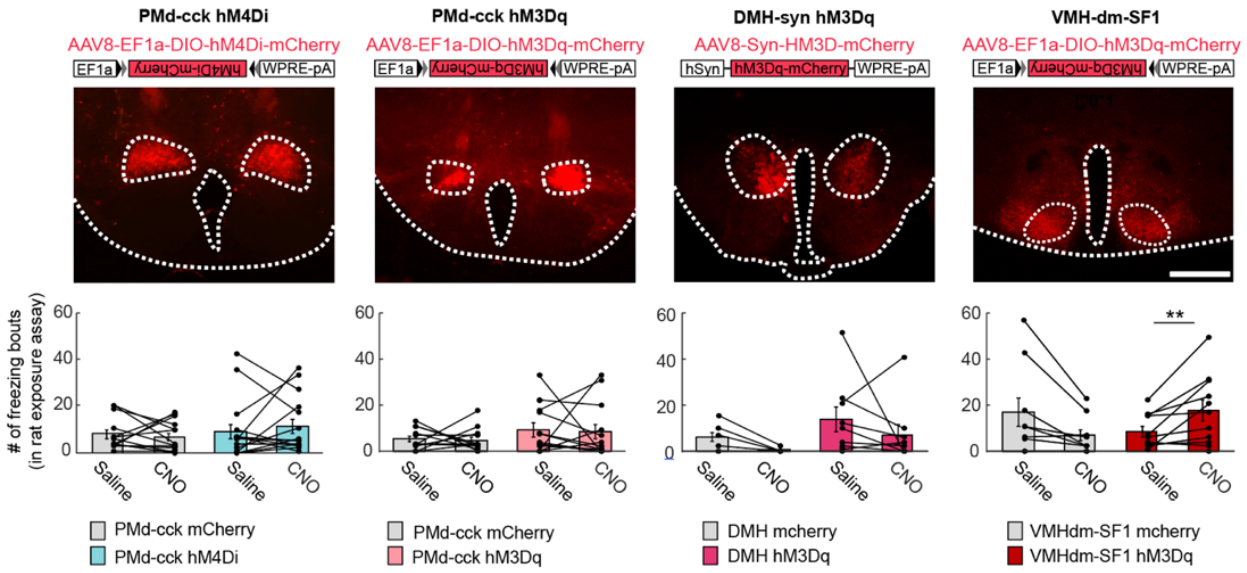

Figure 1.5. Chemogenetic activation of ventromedial hypothalamus SF1 cells increases freezing during exposure to a live rat.

Upper row: Images showing expression of excitatory and inhibitory chemogenetic modulators in PMd-cck cells, dorsomedial hypothalamus (DMH)-synapsin cells and VMHdm-SF1 cells. Scale bar: 500 µm. Lower row: Freezing bouts are increased in VMHdm-SF1 mice treated with CNO during exposure to the rat assay. (Two-Way repeated measures ANOVA followed by post hoc Wilcoxon test, **p < 0.01). n = (14 PMd-cck mCherry, 16 PMd-cck hM4Di), n = (12 PMd-cck mCherry, 13 PMd-cck hM3Dq), n = (6 DMH-syn mCherry, 9 DMH-syn hM3Dq), n = (9 VMHdm-SF1 mCherry,11 VMHdm-SF1 hM3Dq). Mean ± SEM.

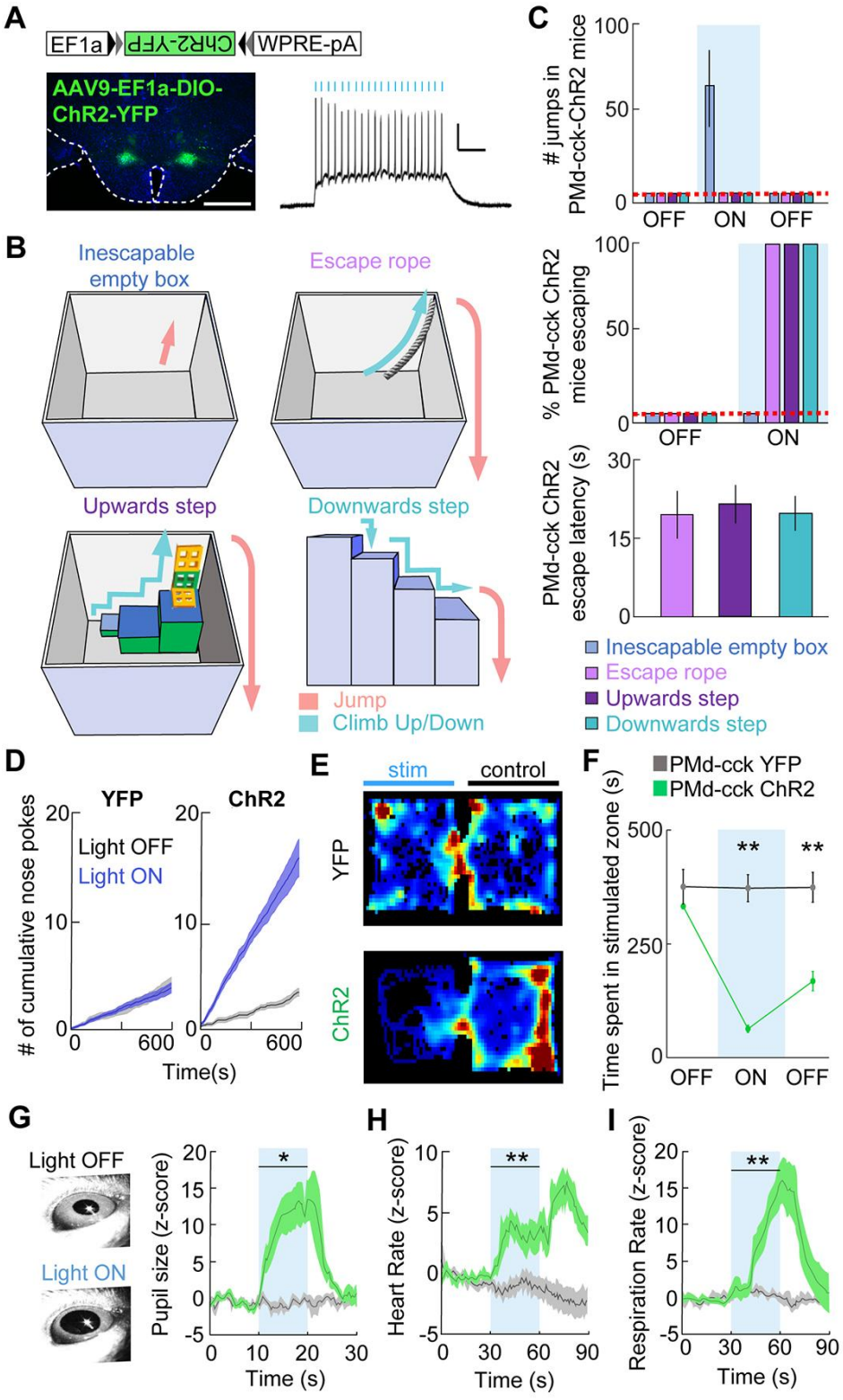

Figure 1.6. Optogenetic activation of PMd-cck cells induces versatile context-specific escape from complex environments as well as autonomic activation and aversion.

(A) Left: Expression of ChR2-YFP in PMd-cck cells. Scale bar: 1 mm. Right: Ex vivo recording showing the response of a ChR2-expressing PMd cell to a 20 Hz, 5 ms, 473 nm light train. Scale bar: 2 mV, 0.2 s. (B) Schemes showing different novel environments in which PMd-cck cells were optogenetically stimulated without any prior training or habituation. (C) (Upper panel) Number of jumps displayed during optogenetic PMd-cck stimulation in each environment. (Middle panel) Bar graph showing escape success from each of the environments (Mean±SEM) in (B) following PMd-cck optogenetic activation. During blue light delivery PMd-cck-ChR2 mice jumped to escape in an inescapable empty box. Optogenetic stimulation of the same mice induced escape using the various escape pathways when they were provided, showing PMd-cck activation induced context-specific escape. (Bottom panel) Bar graph showing the escape latency from light-on for PMd-cck ChR2 mice. All mice escaped within the first 30-second stimulation epoch (n=4). (D) Blue light stimulation was delivered to the PMd continuously and was interrupted for 5 seconds each time the animal nose-poked in a port. PMd-cck-ChR2 mice nose-poked more times than -YFP mice to stop blue light delivery to the PMd, indicating PMd-cck stimulation was aversive (YFP n=4, ChR2 n=4; Wilcoxon rank-sum test, $p < 0.001$). (E) Example heat maps showing occupancy of mice expressing either YFP (top) or ChR2-YFP (bottom) in PMd-cck cells in a real-time place preference task. (F) Average data showing occupancy of the stimulated chamber during baseline, stimulation and post-stimulation periods (respectively labeled OFF, ON and OFF). Each epoch lasted 10 minutes. The post-stimulation period occurred 10 minutes after the end of the stimulation period. Optogenetic stimulation of PMd-cck cells caused marked avoidance of the stimulated chamber during simulation and post-stimulation periods (YFP n=8, ChR2 n=8; Two-way repeated measures ANOVA followed by Wilcoxon test, $**p < 0.001$ for stimulation / post stimulation epochs). (G-I) Pupil size, heart rate and respiration rate in head-fixed mice increased during blue light delivery to PMd-cck-ChR2, but not YFP mice (YFP n=4, ChR2 n=4; Two-way repeated measures ANOVA followed by Wilcoxon test, $*p < 0.05$, $** p < 0.01$). (C,D,F,G-I) Mean ± SEM.

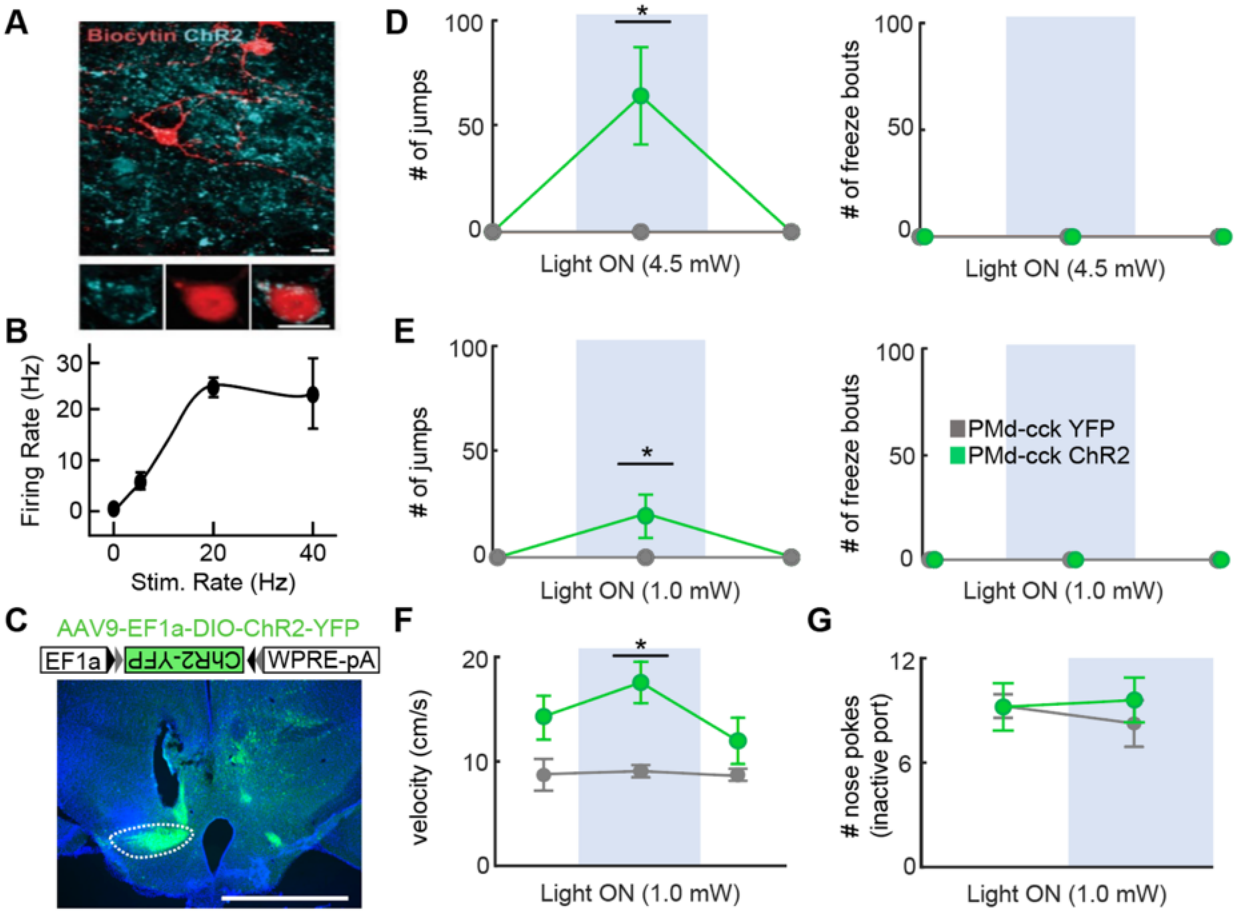

Figure 1.7. PMd-cck optogenetic activation selectively causes escape, but not other defensive behaviors.

(A) Ex vivo slices were prepared from cck-cre mice injected with AAV9-EF1a-DIO-ChR2-YFP in the PMd. Recorded PMd-cck neurons expressing ChR2 were filled with biocytin at the end of the experiment. Image showing biocytin-filled PMd-cck neuron (red) and ChR2-YFP (blue). (B) Plot showing firing rate in ChR2-expressing PMd-cck cells stimulated with blue light trains of 0, 5, 20 and 40 Hz. (A) Both scale bars represent 10 μm. (C) Image showing ChR2-GFP expression in PMd-cck cells along with fiber optic cannula track above the PMd. PMd outline is shown in white. Scale bar: 1 mm. Activation of PMd-cck cells optogenetically increased jumps, but not freezing, both at 4.5 mW (D) and 1 mW (E) stimulation intensity. (F) PMd-cck activation also increased velocity. (D-F) (For each behavioral measure, YFP n = 4, ChR2 n = 4, Wilcoxon rank-sum test, light-on epoch, *$p < 0.05$). (G) PMd-cck activation caused no change in the number of nose pokes when poke did not stop stimulation. (YFP n=4, ChR2 n=5)

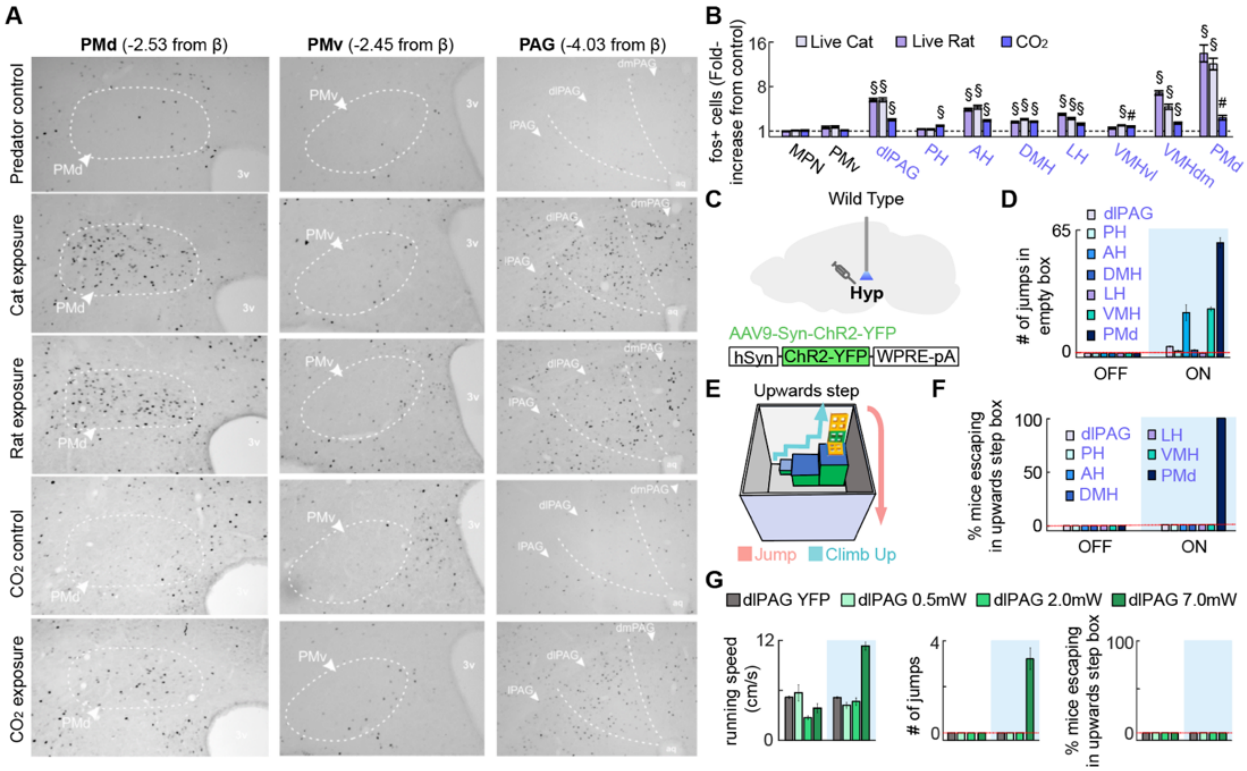

Figure 1.8. Dorsal premammillary nucleus (PMd) optogenetic stimulation induces versatile context specific escape from novel environments.

(A) Images show PMd, PMd and dlPAG sections stained with antibody against fos in mice exposed cat, rat, CO_2 and control conditions. Threat exposure increases fos in PMd and dlPAG. Abbreviations: PMd (dorsal premammillary nucleus), l, dl and dm PAG (lateral, dorsolateral and dorsomedial periaqueductal gray respectively), PMv (ventral premammillary nucleus). (B) Expression of fos in select hypothalamic and brainstem nuclei following exposure to live predators or 15% CO_2. Significantly activated regions are shown in purple. Abbreviations: MPN (median preoptic nucleus), PMv (ventral premammillary nucleus), dlPAG (dorsolateral periaqueductal gray), PH, AH, DMH and LH (posterior, anterior, dorsomedial and lateral hypothalamus, respectively), VMHvl and VMHdm (ventrolateral and dorsomedial ventromedial hypothalamus), PMd (dorsal premammillary nucleus). The PMd showed the highest fos induction during threat exposure compared to other regions (each region, n = 5, two-way independent ANOVA (rat/cat), two-tailed t-test (CO_2), § $p < 0.005$, # $p < 0.01$). (C) Mice were injected with AAV9-syn-ChR2-YFP and had fiberoptic cannulae implanted in regions that showed increased fos expression in (B). (D) These regions (D) were optogenetically activated with blue light in wild type mice in an empty open field box (473 nm, 20 Hz, 3 minutes OFF, 3 minutes ON). The number of jumps displayed is plotted. (D,F) Dashed red line indicates zero.

(E) Side view of the complex route to escape from a novel environment using upwards climbing. Mice had no exposure to this context prior to the test. (F) Regions in (D) were optogenetically

activated in the environment shown in (E) (473 nm, 20 Hz, alternating OFF-ON epochs, for a total of 5 minutes. Each OFF and each ON epoch lasted 30 seconds). Only optogenetic stimulation of the PMd caused escape from this environment before the end of the five-minute assay. (n = 5 ChR2 for each brain region). (G) Mice were injected with AAV9-syn-ChR2-YFP and had fiberoptic cannulae implanted over the dlPAG (n=5). Bars depict running speed (left), the number of jumps (middle) and the percent mice to escape the upwards step box for YFP controls and ChR2 mice at three levels of blue light intensity (0.5, 2.0 and 7.0 mW) for light OFF and light ON epochs. (B,D) Mean ± SEM.

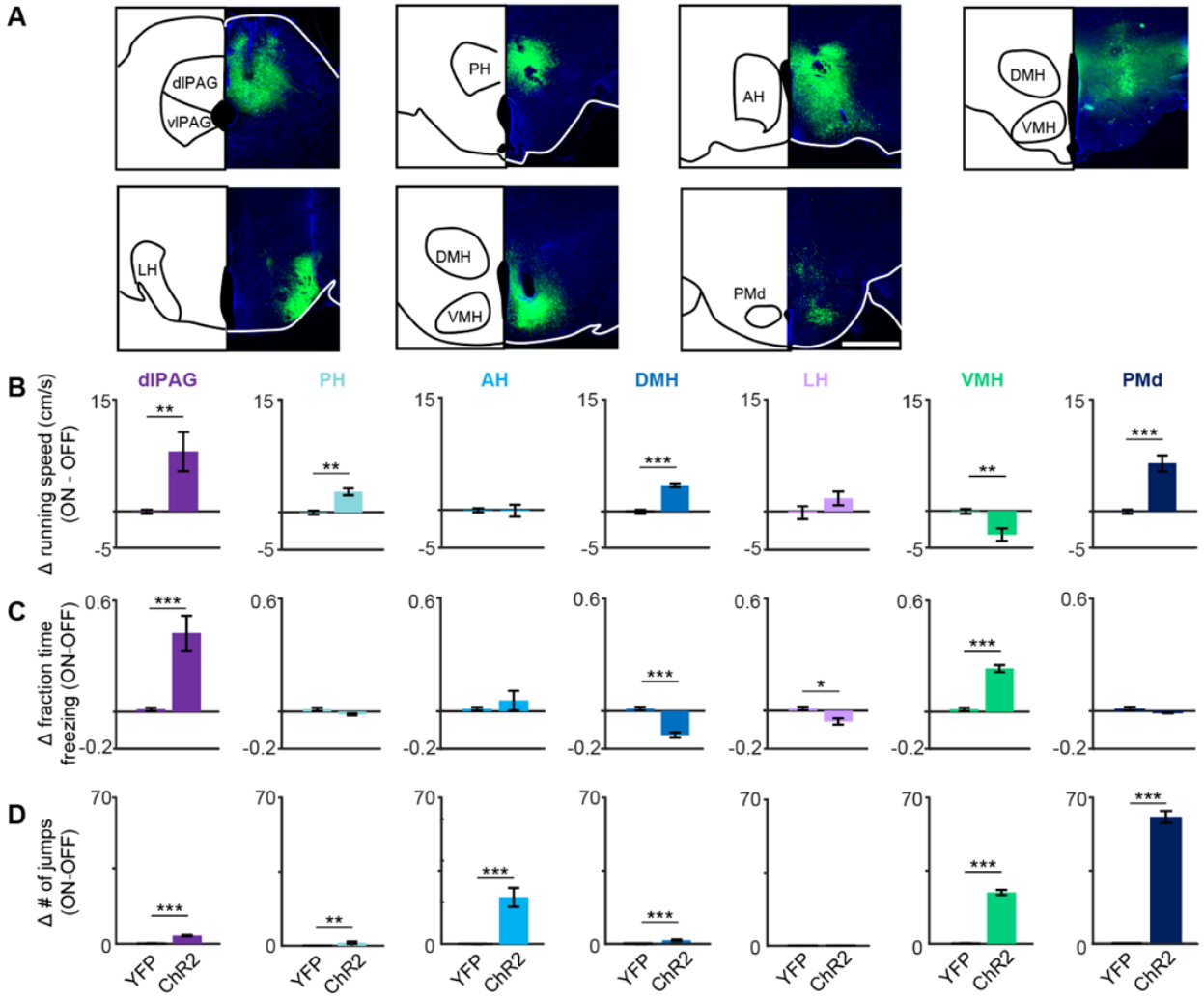

Figure 1.9. Defensive behaviors displayed during optogenetic activation of regions with threat-induced increases in fos expression.

(A) Mice were injected with AAV9-syn-YFP in various hypothalamic nuclei and the dorsal periaqueductal gray. Images show expression of YFP (green) in representative coronal sections. (scale bar: 1 mm) Abbreviations: (dorsal periaqueductal gray), PH, AH, DMH and LH (posterior, anterior, dorsomedial and lateral hypothalamus, respectively), VMHvl and VMHdm (ventrolateral and dorsomedial ventromedial hypothalamus), PMd (dorsal premammillary nucleus). (B-D) All regions showing significant increases in fos expression following exposure to threats (Supplemental Figure 6) were optogenetically activated in wild type mice in an empty open field box. Mice were injected with AAV9-syn-ChR2-YFP in the target structure and light was delivered in 20 Hz 5-ms pulses. Bar plots showing increases in running speed (B), freezing (C) and escape jumps (D) following optogenetic stimulation. YFP controls for activated nuclei did not differ in any of the measured behaviors and were thus pooled together (Pooled YFP n = 25, dlPAG n = 5, PH n = 5, AH n = 6, DMH n = 5, LH n = 5, VMH n = 5, PMd n = 5) The ON-OFF difference was

compared between YFP and ChR2 groups by two sample t-test; *p < 0.05, **p < 0.01, ***p < 0.001).

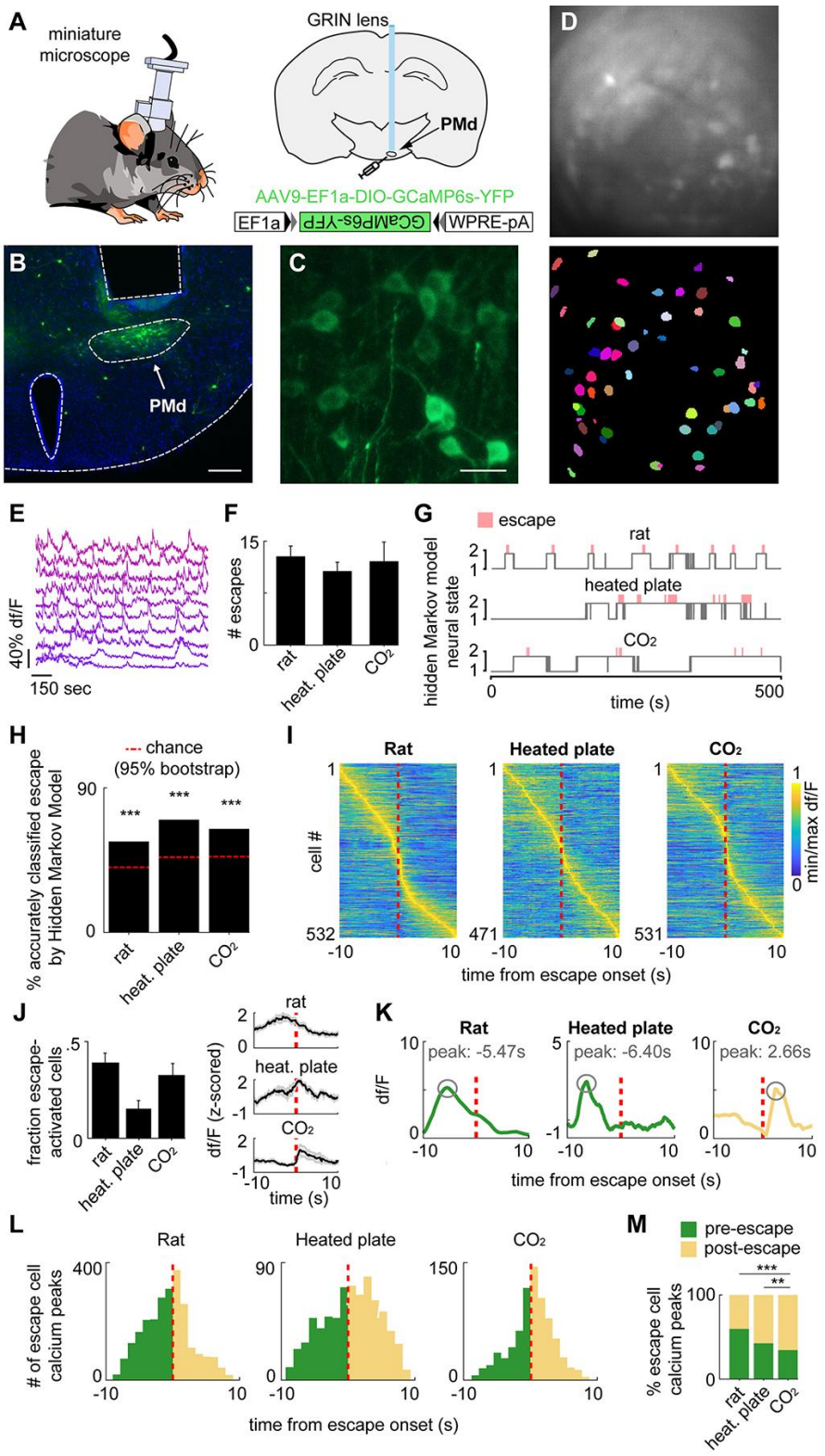

Figure 1.10. Microendoscopic recordings of the PMd reveal escape-predicting states and higher activation prior to context-specific escapes.

(A) Diagram of calcium imaging setup and GRIN lens. (B) Histology of GRIN lens implantation and GCaMP6s expression in the dorsal premammillary nucleus of the hypothalamus (PMd). (scale bar: 200 μm) (C) 40x times magnified view of histology in (B). (scale bar: 10 μm)
(D) (top) Maximum projection of the PMd field of view. (bottom) Putative cell contours for the same session. (E) Extracted calcium activity of example cells in PMd. (F) Escape count in each assay (rat n=10, heated plate n=9, CO_2 n=12). (G) States were extracted from neural data (unsupervised Hidden Markov model (HMM), 2 states). In these examples, the states (gray) separate escape from non-escape epochs (escape=red bar), even though escape information was not part of the input to the model. (H) The HMM-defined states significantly predicted escape. (chance level=red line; ***p<.001) (I) Rows depict the mean normalized escape-aligned activity of a cell during rat (left), heated plate (middle) or CO_2 (right) assays. (rat n=532; heated plate n=471; CO_2 n=531) (J) (left) Bars depict the fraction of escape-activated cells identified in each threat assay. (rat n=10, heated plate n=9, CO_2 n=12) (right) Example traces of mean escape-activated cell activity (+/-1 SEM) aligned with escape onset. (escape count: rat n=12, heated plate n=10, CO_2 n=8) (K) For each escape behavior of each escape-classified cell, the calcium peak was found and its lag, relative to escape onset, was quantified. Examples show peaks that occurred before (rat/heated plate, green) and after escape (CO_2). (L) Histograms show calcium peak count (shown in (K)) relative to escape onset for threat assays. (green=pre-escape; yellow=post-escape; Rat: pre n=1686, post n=967; Heated plate: pre n=295, post n=398; CO_2: pre n=260, post n=498) (M) Bars depict the percent of calcium peaks (shown in (K)) that occurred pre- (green) or post- (yellow) escape. (Fisher's exact test, **p<.01, ***p<.001) (K-M) Only cells significantly modulated by escape were used.

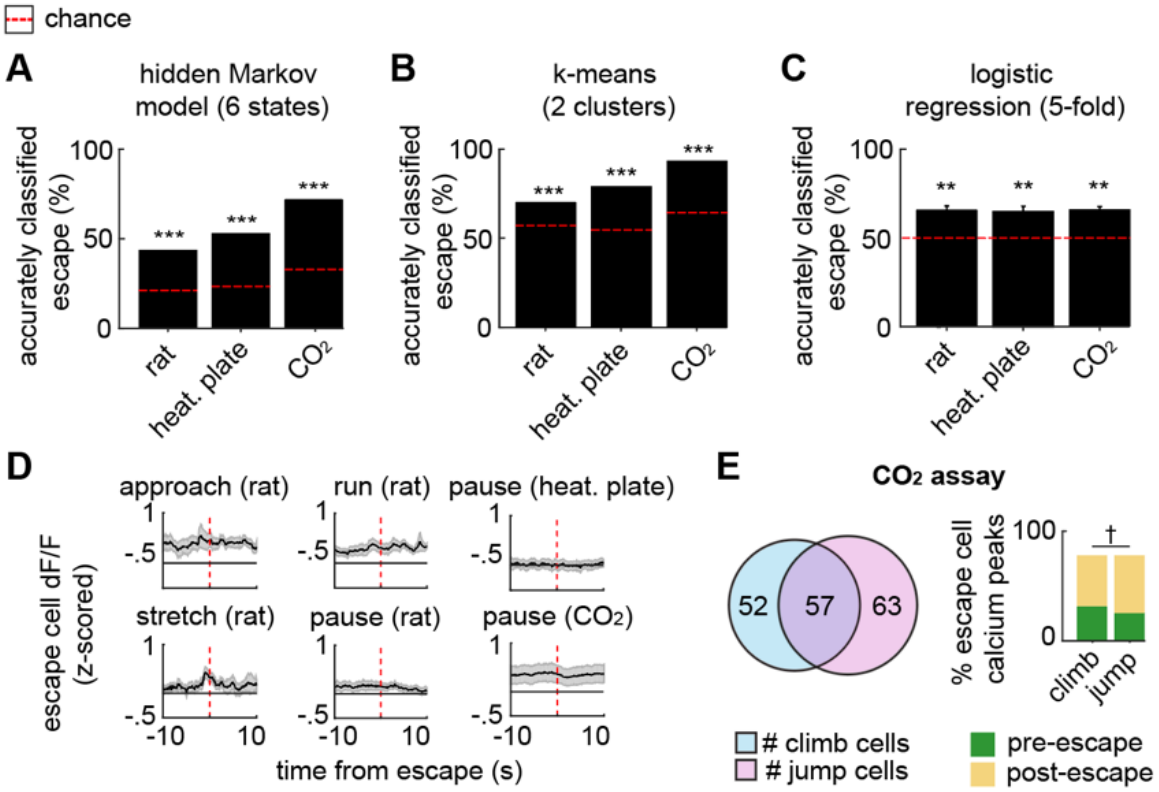

Figure 1.11. Supervised and unsupervised analyses significantly predict escape from neural data.

(A) The states extracted by hidden Markov model (6 states) predicted escape at a level significantly greater than chance (red lines) for each threat assay. ($p<.001$). (B) Similar to (A), using k-means, an alternative unsupervised technique, two clusters could predict escape at a level significantly greater than chance (red lines) for each threat assay. (C) Using 5-fold logistic regression, escape could be predicted for each assay at a level significantly greater than chance (red line) (rat n=10, heated plate n=9, CO_2 n=8. (D) Lines show the mean z-scored signal (+/- 1 s.e.m.) for escape-categorized cells, aligned to behavioral onsets occurring within -10 to 10 seconds of an escape (rat: n = 10; heated plate: n = 9; CO_2 : n = 12). (E) (left) Venn diagram depicts the overlap in climb- and jump-classified cells in the CO_2 assay (climb cell n=109, jump cell n=120, session n=9). (right) Bars depict the percentage of exclusive climb- and jump-categorized cell calcium peaks that occurred pre- (green) or post- (yellow) escape. (pre-escape n=97, post-escape n=144; jump: pre-escape n=145, post-escape n=297; Fisher's exact test, † $p=0.055$) (A-C) Mean ± SEM. (** $p<.01$, *** $p<.001$)

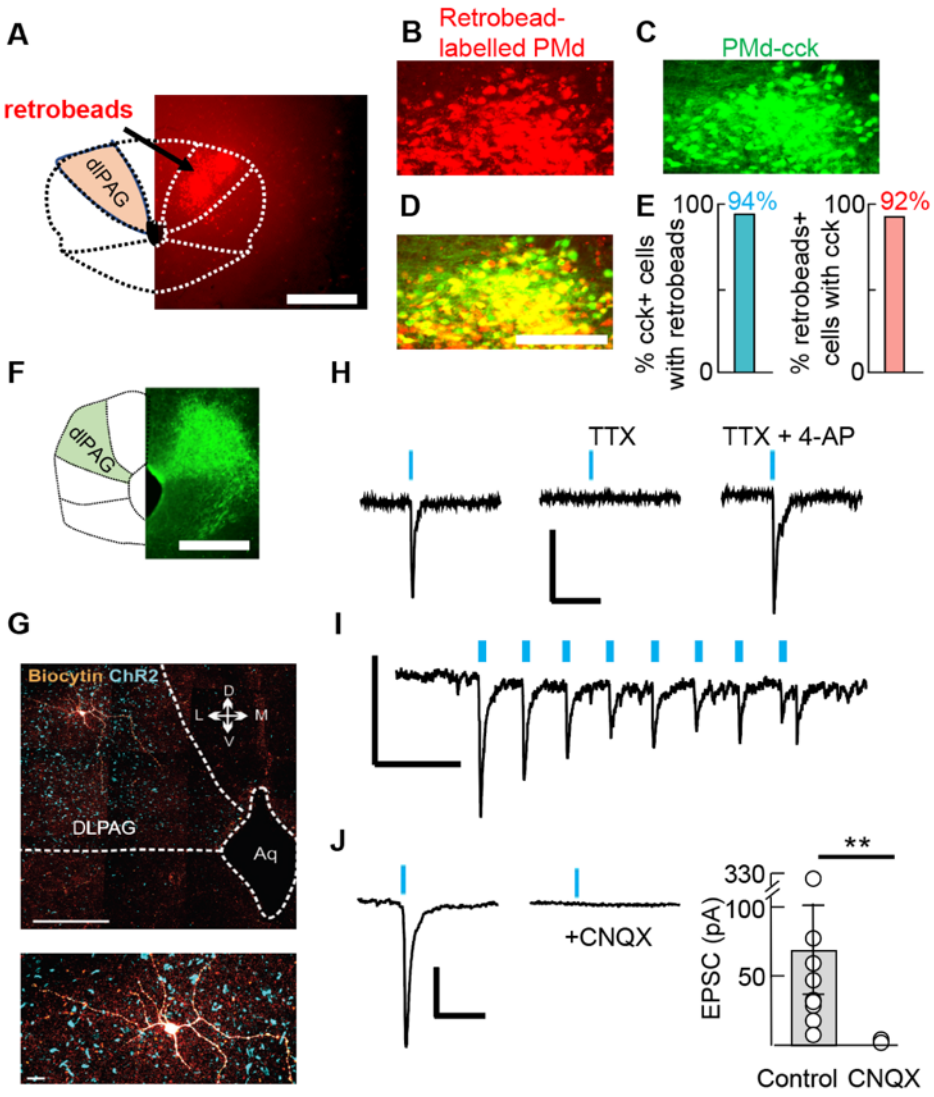

Figure 1.12. Anatomical and functional characterization of the PMd-cck to dlPAG projection.

(A) Retrobeads were injected in the dlPAG in cck-cre mice expressing cre-dependent YFP in the PMd. (scale bar: 500 μm) (B) Presynaptic dlPAG-projecting PMd cells with retrobeads. (C) YFP expression in PMd-cck cells. (D) Overlay. Scalebar: 250 μm. (E) Quantification of overlap between dlPAG-projecting and cck-cre expressing cells. (F) GFP-expressing PMd-cck axon terminals in the dlPAG. (scale bar: 500 μm) (G) Top: Photograph showing biocytin filled dlPAG neuron (orange) and ChR2-expressing PMd-cck (blue). (scale bar: 200 μm) Bottom: Higher magnification image of the dlPAG cell from the top panel. (H) Left: dlPAG cell shown in (G) showed excitatory response following blue light delivery to excite ChR2-expressing PMd-cck axon terminals in an ex vivo slice preparation. Middle: The response disappeared following application of tetrodotoxin (TTX, 0.3 μM). Right: The response was rescued following the application of the potassium channel blocker 4-aminopiridine (4-AP, 0.5 mM). (scale bar: 50 ms, 20 pA). Aq: aqueduct (I)

Overlaid traces of dlPAG cell showing responses to 20 Hz 5ms train stimulation of ChR2-expressing PMd-cck axon terminals. (scale bar: 100 ms, 20 pA) (J) dlPAG responses to stimulation of PMd-cck terminals were abolished in the presence of the glutamatergic AMPA/kainate receptor blocker cyanquixaline (CNQX, 20 μM). (scale bar: 50 ms, 20 pA) (Control n = 9, CNQX n = 9; Wilcoxon rank-sum test, **p = 0.009).

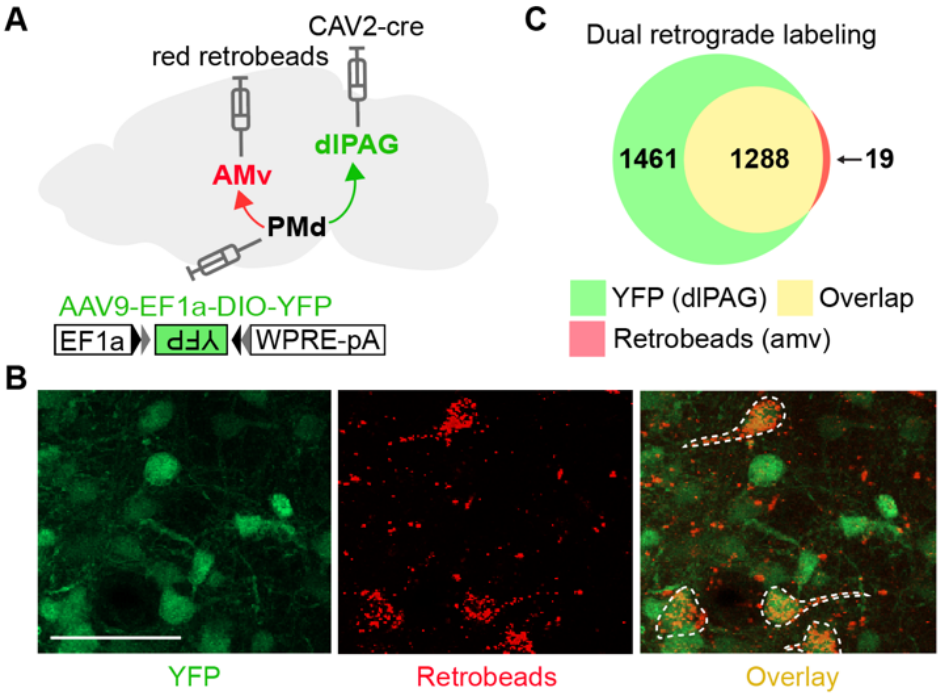

Figure 1.13. Characterization of PMd projections to amv and dlPAG.
(A) Scheme showing approach to label PMd cells projecting to amv and dlPAG. Red retrobeads were injected in the amv, retrograde CAV2-cre was injected in the dlPAG and AAV9-EF1a-DIO-YFP was injected in the PMd. (B) Representative images showing YFP-expressing and retrobead containing PMd cells, which respectively project to the dlAPG and amv. Double-labelled cells projecting to both regions are shown with a white dashed outline. (scale bar: 50 µm) (C) Venn diagram showing the overlap of YFP and retrobead-labelled cells in the PMd. (n=4 mice; 2768 cells)

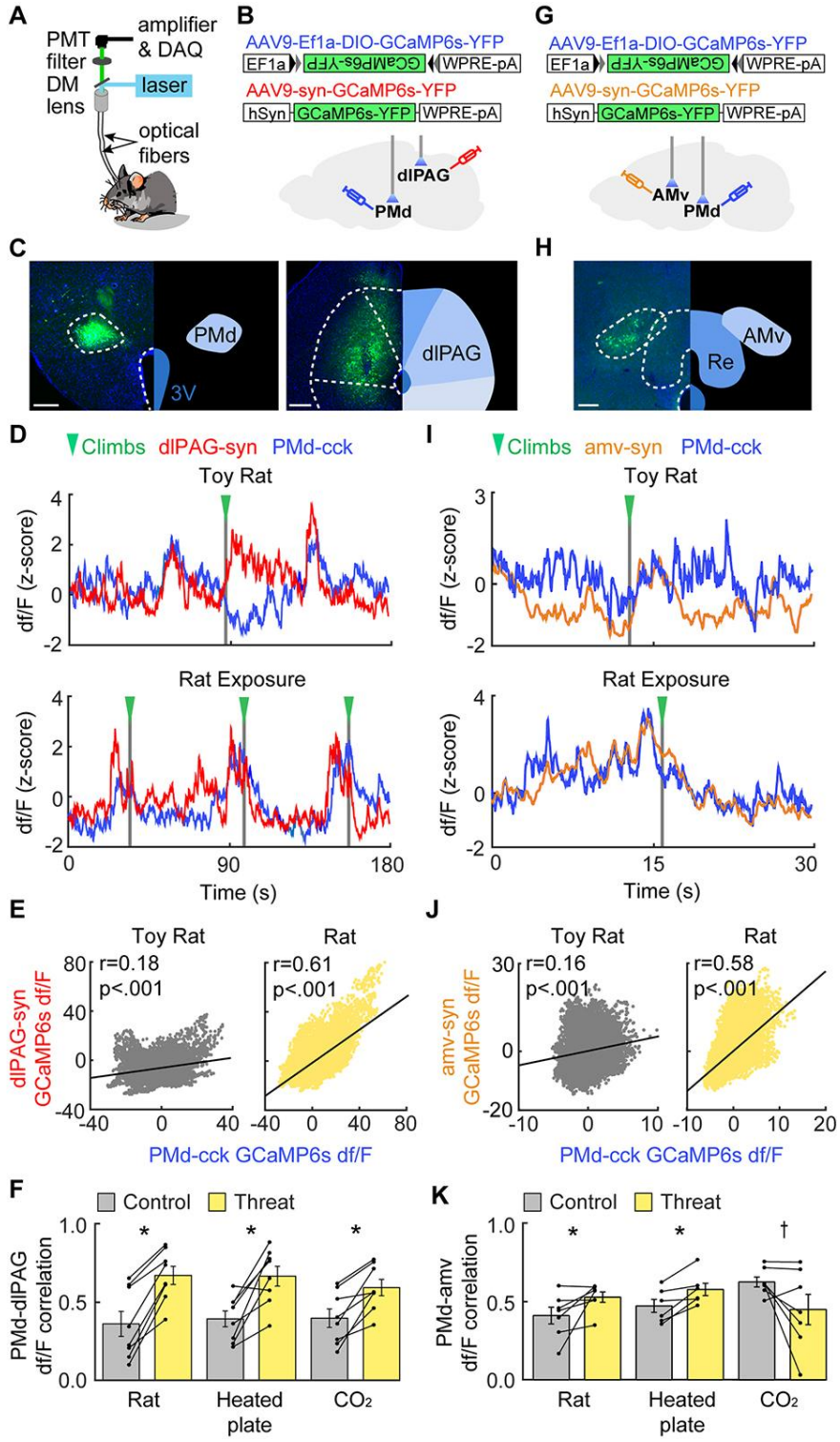

Figure 1.14. The PMd-cck→dlPAG-syn circuit becomes more synchronized during threat assays, while the PMd-cck→amv-syn circuit becomes more synchronized only in assays requiring context-specific escape.

(A) Dual-site fiber photometry setup. (B) Strategy to express CGaMP6s in PMd-cck cells and dlPAG-synapsin cells. (C) Histology of GCaMP6s expression in the PMd (left) and the dlPAG. (right; PMd scale bar: 200μm; dlPAG scale bar: 150μm) (D) PMd-cck and dlPAG traces from toy rat and rat assays. (E) PMd-cck and dlPAG signals were more correlated during rat than toy rat exposure. (Spearman correlation r_s: toy rat: r_s=.177, p<0.001; rat: r_s=.612, p<0.001)
(F) Average bar plot showing PMd-cck and dlPAG activity were more correlated during threat than control (toy rat, unheated floor and air) exposure. (n=8 threat assays, Wilcoxon rank-sum test,*p < 0.05) (G) Strategy to express CGaMP6s in PMd-cck cells and anterior medial ventral thalamus (amv)-synapsin cells. (H) Histology of GCaMP6s expression in the amv. (scale bar: 150μm) (I-K), Same as (D-F), but for mice expressing CGaMP6s in PMd-cck cells and amv-synapsin cells. (n=7 for rat, CO_2 and controls; n=6 for heated plate and control) (J) Spearman correlation r_s: toy rat: r_s=.164, p<0.001; rat: r_s=.583, p<0.001. (K) Wilcoxon rank-sum test, *p<0.05, † p=0.078.

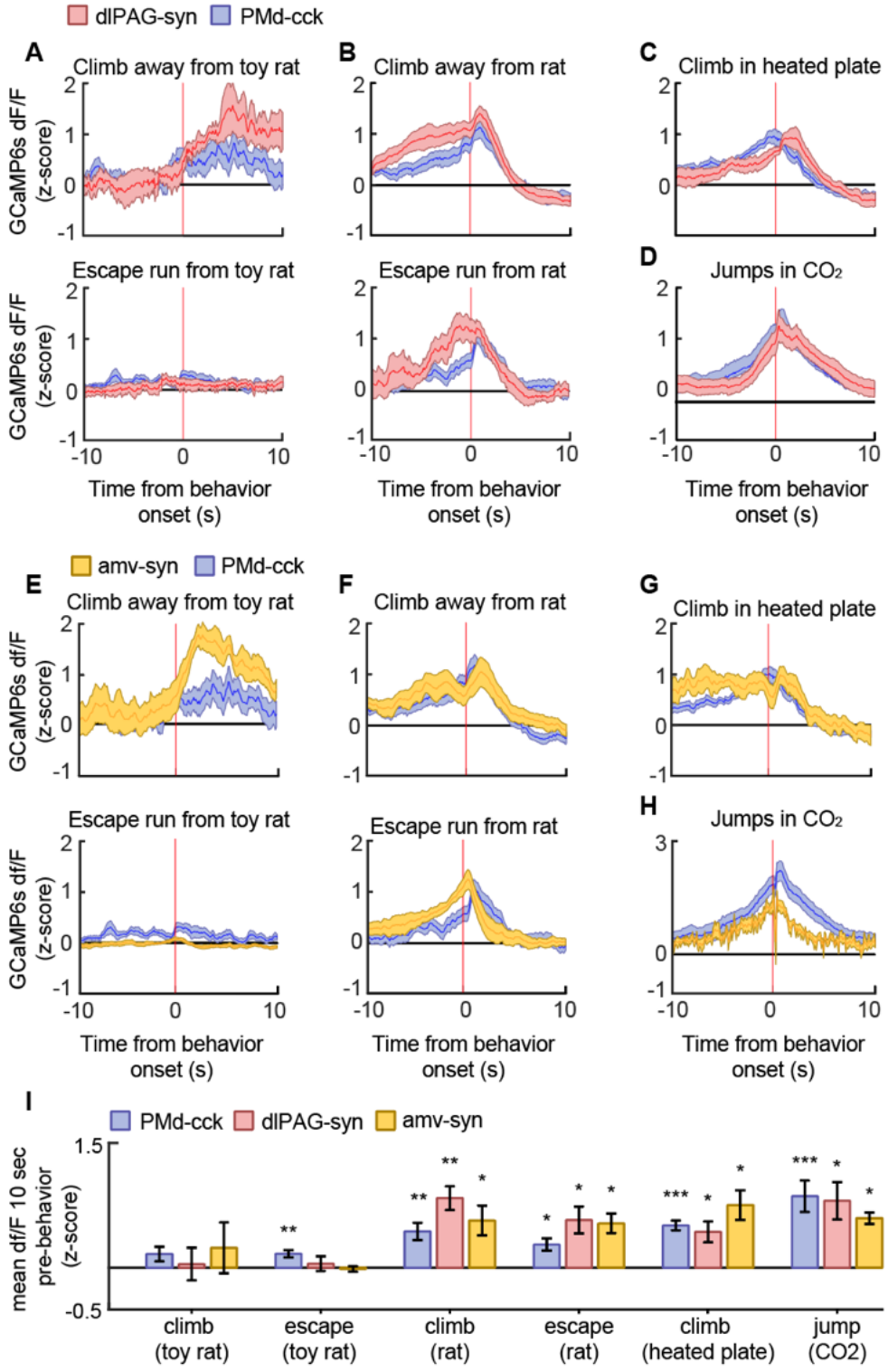

Figure 1.15. Behavior-aligned photometry signals from PMd-cck/dlPAG-syn and PMd-cck/amv-syn during escape behaviors.

(A-D) Dual-site fiber photometry recordings were performed in cck-cre mice injected with AAV9-Ef1a-DIO-GCaMP6s-YFP and AAV9-syn-GCaMP6s-YFP respectively in the PMd and the dlPAG. (A) Average photometry signals centered around climb and escape run in toy rat assay (n = 9). (B) Same as (A), but for rat exposure (n = 9). (C) Average PMd-cck and dlPAG photometry signals centered around climbs in the heated floor assay. (n = 8) (D) Same as (A) but for jumps during CO_2 exposure. (n = 9) (E-H), Same as (A-D), but for dual-site fiber photometry recordings performed in cck-cre mice injected with AAV9-Ef1a-DIO-GCaMP6s-YFP and AAV9-syn-GCaMP6s-YFP respectively in the PMd and the amv. (n = 7 for rat and CO_2 assays and controls; n = 6 for heated plate assay.) (I) In all threat assays, PMd-cck, dlPAG and amv neural activity increased prior to escape. (Wilcoxon signed-rank test, * p<.05, ** p<.01, ***p<.001) (A-H) Mean ± SE

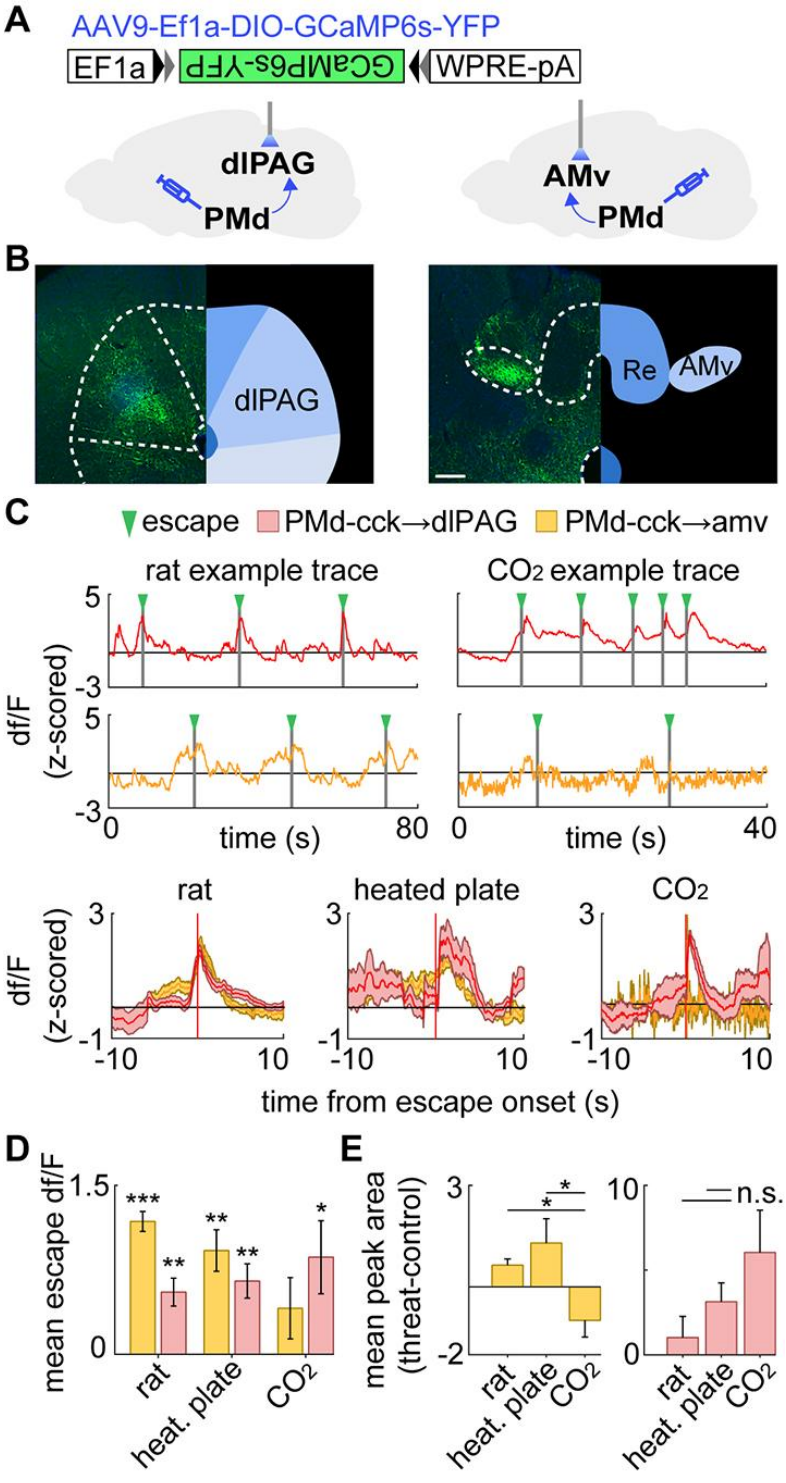

Figure 1.16. PMd axon terminals in the amv are activated only during context-specific escape while terminals in dlPAG are activated during all escapes.

(A) Recordings were obtained from GCaMP6s-expressing PMd-cck axons terminating in the dlPAG (left) or the amv (right). (B) PMd-cck GCaMP6s-expressing axons in the dlPAG (left) and amv (right). (scale bar: 150 μm) (C) (top) Example fiber photometry traces from PMd-cck axons

in the dlPAG (red) and amv (orange) in the rat and CO_2 assays. (bottom) Examples of mean escape-triggered activity from PMd-cck axon terminals in the dlPAG and amv. (escape count, rat: dlPAG n=10, amv n=10; heated plate: dlPAG n=6, amv n=8; CO_2: dlPAG n=4, amv n=5) (D) Bars show the mean df/F in a 4s window centered at escape onset for PMd-cck axons in the dlPAG or amv. (n=6 mice) (E) Bars depict the difference of mean positive df/F amplitude. (n=6 mice) ***p<0.001, **p<0.01, *p<0.05.

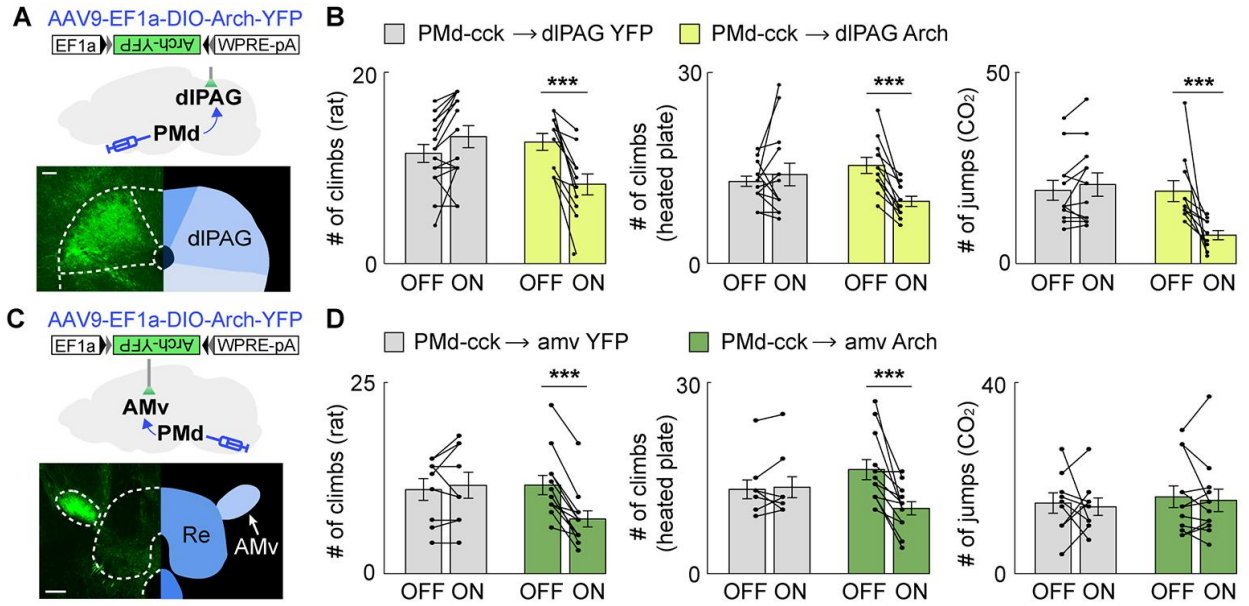

Figure 1.17. Inhibition of the PMd-cck→dlPAG projection decreases escape in all threat assays while inhibition of the PMd-cck→amv-syn projection selectively decreases context-specific escape.

(A) Strategy to optogenetically inhibit arch-expressing PMd-cck axons terminating in the dlPAG (scale bar: 100μm) (B) Optogenetic inhibition of the PMd-cck→dlPAG projection with green light (532 nm) decreased escape in all assays. (rat: YFP n=15, arch n=11; heated floor: YFP n=12, arch n=11; CO_2: YFP n=14, arch n=11, Two-way repeated measures ANOVA followed by Wilcoxon test, ***p < 0.001) (C) Similar to (A), but with fiber optic cannula implanted over the amv. (scale bar: 150μm) (D) Optogenetic inhibition of the PMd-cck→amv-syn projection with green light decreased escape count during rat (left), heated floor (middle) but not CO_2 (right) exposure. (rat: YFP n=9, arch n=12; heated floor: YFP n=9, arch n=12; CO_2: YFP n=9, arch n=12, Two-way repeated measures ANOVA followed by Wilcoxon test, ***p < 0.001) Mean ± SEM.

Chapter 2. Dorsal premammillary projection to periaqueductal gray controls escape vigor from innate and conditioned threats.

Innate and conditioned threats induce defensive behaviors.

To study the PMd's role in controlling defensive behaviors, we exposed mice to two threats: a live predatory rat or a shock grid. These two assays were used to investigate, respectively, innate and conditioned threats. For the rat assay mice were exposed either to a safe control toy rat or an awake rat in a long box (70 cm length, 26 cm width, 44 cm height) for 10 minutes. The rat was placed at one of the corners and its movement was restricted by a harness tied to a wall, restricting its range of motion to the rat area shown in pink in Figure 2.1A. Rats were screened for low aggression and predatory tendencies and thus they did not attack mice. No separating barrier was used between rats and mice allowing for close naturalistic interactions. Rat and toy rat exposures were separated by 24 hours. For the shock grid assay, mice first explored a different box for 3 consecutive days for 10-minute sessions. The shock grid was placed in one of the corners of the box, as shown in Figure 2.1A. On day 1, no shocks were given and mice freely explored the environment. On day two, a single 0.7 mA 2 sec shock was given the first time the mouse touched the shock grid. On day 3 (fear retrieval), no shocks were given. All behavioral and neural data plotted from the shock grid is from the fear retrieval day, unless otherwise noted. The pre-shock baseline was used as the control for the fear retrieval day. All sessions were separated by 24 hours (Figure 1B). Threat exposure induced distance from the threat source, freezing and stretch-attend postures (Figure 2.1C; Figure 2.2). (The mean freeze bout duration was 2.03s ± 0.15). Additionally, relative to control assays, during exposure to threat approach velocity was lower while escape velocity was higher (Figure 2.1C). These results indicate that mice slowly and cautiously approach threats and then escape in high velocity back to safer locations far from

threats. There was no significant difference in these measures for male and female cohorts (male n=17, female n=15; Wilcoxon rank-sum test, $p>0.05$).

We performed the rat exposure assay before the shock grid assay because the former is a milder experience than the latter; no actual pain is inflicted in the rat assay. We thus reasoned that the more intensely aversive assay (the shock assay) was more likely to influence behavior in the rat assay than vice-versa. Nevertheless, to determine if there could be an effect of order, we exposed two cohorts of mice to the rat and shock grid threats in a counterbalanced manner, and show that behavior in the shock grid assay is not affected by prior experience in the rat assay. (Figure 2.3). Taken together, these data show that both innate and conditioned threats induced defensive behaviors. Our data also support the view that escape velocity is a measure of threat-induced behavior. No sex differences were found in either behavioral assay (Figure 2.4).

Pmd-cck cells are activated by proximity to threat and during escape

We next investigated the activity of PMd cells during threat exposure. To do so, we used a cholecystokinin (cck)-cre line. We then injected AAV-FLEX-GCaMP6s in the PMd and implanted fiberoptic cannula above the injection site in cck-cre mice to record calcium transients in PMd-cck cells using fiber photometry (Figure 2.5A-C). Animals exhibited robust defensive behavior in the presence of threat (Figure 2.6). Examining the relationship of general locomotion and to the fiber photometry signal, we found that the signal amplitude was higher during threat exposure relative to control assays for a wide range of matched speed values (Figure 2.7). Averaged heat maps show PMd-cck activity was increased near the rat and the shock grid during fear retrieval (Figure 2.5D). Indeed, activity was increased near threats relative to control stimuli (toy rat and shock grid in pre-shock day). These comparisons were done when analyzing data at the same speed range (Figure 2.5E); thus PMd-cck cells are more active near threats independently of locomotor changes. We next studied how PMd-cck cell activity changed during defensive behaviors. A

representative trace suggests that these cells show high activity during escape (Figure 2.5F). Average data show that in both assays PMd-cck cells showed increased activation during risk-assessment stretch-attend postures and during escape, while a decrease in activity was displayed during freezing (Figure 2.5G-I). Furthermore, the total distance of each escape was correlated with PMd-cck activation during exposure to threats, but not control stimuli (Figure 2.5J). These results show that PMd-cck cells are quickly activated by proximity to threat and escape, during exposure to both innate and conditioned threats. In agreement with this view, PMd-cck cells displayed relatively high membrane input resistance (484 ± 64 MOhms) and low rheobase, which is the minimum current required to elicit an action potential (38.3 ± 6.1 pA) (Figure 2.8). These results indicate that fairly minor excitatory input is enough to activate these cells. These biophysical characteristics suggest that these cells may be rapidly activated in the presence of threats.

PMd-cck ensemble activity predicts escape occurrence and flight vigor

To analyze how PMd-cck ensemble activity encodes escape, we implanted miniature head mounted fluorescent microscopes (miniscopes) above GCaMP6s-expressing PMd-cck cells (Figure 2.9A-B). Large ensembles of PMd-cck cells were recorded in the rat and shock grid assays (Figure 2.9C-D). Using a generalized linear model (GLM), we identified a large fraction of PMd-cck cells that are active during these behaviors (Figure 2.9E). The behavior that activated the largest and smallest number of PMd-cck cells, was respectively, escape and freezing (Figure 2.9E). These data agree with our fiber photometry results showing that bulk PMd-cck activity is highest during escape and lowest during freezing. Behavior triggered averages indicate that PMd-cck cells may be significantly activated during defensive behaviors, in agreement with these results (Figure 2.9F). Further supporting a role for PMd-cck cells in escape, we show that ensemble activity could be used to decode ongoing escape, but not other behaviors (Figure 2.9G). These intriguing results raise the possibility that PMd-cck activity may be able to predict future

occurrence of escape. Indeed, PMd-cck activity could predict escape from innate and conditioned threats several seconds prior to escape onset. However, ensemble activity could not predict movement away from control stimuli (toy rat and shock grid in pre-shock day) (Figure 2.9H). These data show that PMd-cck activity can specifically predict future escape from threats, but not moving away from objects in general. Additionally, we found that PMd-cck cells represent not only future escape onset (Figure 2.9H) but also escape speed. Using the correlation of single cell activity and escape speed, we classified escape speed cells (see Methods) in the control and threat assays. A higher fraction of PMd cells showed activity significantly correlated with escape speed for threat than control stimuli (Figure 2.9I). Additionally, for these escape speed-correlated cells, the mutual information between escape speed and calcium signal is significantly greater during threat than control (Figure 2.9K). These data indicate that PMd-cck activity is related to defensive escape and speed in the presence of threat, rather than general locomotion.

Our fiber photometry results indicate that PMd-cck cells were more active during close proximity to threat (Figure 2.5D). These data suggest that PMd-cck ensemble activity may represent position in threat assays. We thus decoded position in both control and threat assays using PMd-cck ensemble activity. Strikingly, the error of position decoding was both smaller in threat than in control assays and significantly less than chance error (Figure 2.10A-B). These results show that PMd-cck cells represent distance to threat more prominently than distance to control objects.

Having observed that a greater proportion of PMd cells correlate with speed (Figure 2.9I-J), we then studied if ensemble activity could predict movement vigor, measured by velocity. Indeed, PMd-cck activity could be used to decode velocity during threat exposure with higher accuracy than during exposure to control stimuli (Figure 2.11). Furthermore, decoding of velocity in control assays was less accurate than in threat assays, for both the rat and the shock assays (Figure 2.11). Since PMd ensemble activity can predict future escape, but not approach, we hypothesized

that PMd activity could be used to decode velocity away from threats more accurately than velocity towards threats. Representative traces showing predicted and observed velocity support this hypothesis (Figure 2.10C). Indeed, averaged data across mice show that the error for predicted velocity is lower for decoding velocity away from threat compared to velocity towards threat. Moreover, only velocity away from threat can be predicted with an error significantly less than chance (Figure 2.10C-D). These data show that PMd-cck cells represent key kinematic variables related to rapid escape from threats.

PMd-cck inhibition decreases escape vigor

Recordings of PMd-cck ensemble activity revealed that these cells are highly active during escape and that their activity can be used to decode escape (but not approach) velocity. Moreover, neural activity could only decode escape, but not other behaviors. We thus hypothesized that inhibition of PMd-cck cells would decrease escape velocity without affecting other defensive behaviors. To test this view, we expressed the inhibitory receptor hM4Di in PMd-cck cells (Figure 2.12A). We confirmed that the hM4Di receptor ligand clozapine-n-oxide produced hyperpolarization (Figure 2.12B). We then exposed mice to the assays described in Figure 1A. Mice were exposed to each threat and control assay twice, following treatment with either saline or the hM4Di ligand clozapine-N-oxide (CNO) (Figure 2.12C). Inhibition of PMd-cck cells in CNO-treated mice decreased escape velocity from both threats, in line with our prediction (Figure 2.12D). Importantly, inhibiting these cells did not change velocity while mice moved away from control safe stimuli (toy rat and shock grid prior to fear conditioning) (Figure 2.13). This manipulation did not change freezing or stretch-attend postures (Figure 2.12D), showing PMd-cck activity is selectively required for escape, rather than defensive behaviors in general.

Activation of PMd-cck cells recruits a wide network of regions involved in defensive behaviors

As PMd-cck inhibition decreases escape velocity, but not other behaviors, we predicted that activating these cells would specifically induce running and escape-related motion. Indeed, optogenetic activation of ChR2-expressing PMd-cck cells caused an increase in speed, but not in the amount of freezing or stretch-attend postures (Figure 2.14A-B).

We next investigated which downstream regions are recruited following activation of PMd-cck cells. Prior studies showed that the PMd projects to several structures involved in defense, such as the dorsolateral periaqueductal gray (dlPAG) and the anterior hypothalamus. Interestingly, it also projects to the anteromedial ventral thalamus (amv) (N. S. Canteras and Swanson 1992). The amv has head direction cells (Bassett, Tullman, and Taube 2007) and is a region critical for spatial navigation (Jankowski et al. 2013) and threat-conditioned contextual memory (Carvalho-Netto et al. 2010).

We hypothesized that activation of PMd-cck cells would recruit not only these known direct downstream areas, but also other structures involved in mounting a defensive behavioral state and regions involved in escape-related motor actions. To test this hypothesis we optogenetically activated ChR2-expressing PMd-cck cells with blue light for 10 minutes (20 Hz, 5 ms pulses). Following perfusion, we performed an antibody stain against the immediate early gene cfos. PMd activation increased fos expression in regions that it projects to, such as the amv and the dlPAG. Interestingly, other nuclei critical for defensive behaviors, such as the basolateral amygdala, lateral septum and the bed nucleus of the stria terminalis were also activated (Figure 2.14C), even though they are not innervated by the PMd (N. S. Canteras and Swanson 1992). These results show that the PMd recruits not only its direct downstream outputs, but also other regions involved in threat-related defense. Striatal regions were also activated, such as the caudate nucleus, possibly due to the hyperlocomotion and escape-related actions observed during optogenetic

stimulation. Importantly, not all regions were engaged, showing functional specificity. For example, the dentate gyrus and the PMd-adjacent ventral premammillary nucleus did not show increases in fos expression following PMd stimulation (Figure 2.14D). These data show that PMd-cck cells can recruit a broad network of threat-activated regions, which may contribute to a transition to a defensive state. Despite these intriguing data, it is possible that endogenous natural PMd activation does not result in recruitment of the same nuclei seen following optogenetic PMd-cck activation.

The dorsolateral periaqueductal gray (dlPAG) is active during escape

To identify which PMd downstream targets controlled escape, we studied its two main outputs, the anteromedial ventral thalamus (amv) and the dorsolateral periaqueductal gray (dlPAG) (N. S. Canteras and Swanson 1992). The amv has head direction cells (Bassett, Tullman, and Taube 2007) and is a region critical for threat-conditioned contextual memory (Carvalho-Netto et al. 2010) and spatial navigation (Jankowski et al. 2013).

The amv is also necessary for the acquisition of contextual fear elicited by predators (Carvalho-Netto et al. 2010), demonstrating this region has a role in defensive behaviors. In contrast, the dlPAG is a critical node in the escape network (Del-Ben and Graeff 2009; Tovote et al. 2016).

To identify which of these PMd outputs control escape speed, we injected AAV9-syn-GCaMP6s in wild type mice in either the amv or the dlPAG and obtained calcium transient recordings in the rat and shock grid assays (Figure 2.15A). DLPAG activity increased during escape from the rat (Figure 2.15C), in agreement with prior work showing this region is active during escape from innate threats (Evans et al. 2018; Deng, Xiao, and Wang 2016). However, the dlPAG also showed increased activity during exposure to the fear conditioned shock grid during fear retrieval (Figure 2.15D-E). To our knowledge, there are no prior reports showing the dlPAG is active during escape

from conditioned threats. Surprisingly, like the dlPAG, the amv was also active during escape from both threat modalities (Figure 2.15G-I), even though there are no prior reports implicating the amv in escape.

Inhibition of the PMd-cck projection to the dlPAG decreases escape speed

Our fiber photometry results show that both major outputs of the PMd to the dlPAG and the amv are active during escape from threats, indicating the PMd-cck projections to these regions may control escape vigor. To identify which projection controlled escape vigor, we expressed the inhibitory opsin Arch in PMd-cck cells and implanted fiberoptic cannulae bilaterally over either the amv or the dlPAG (Figure 2.16A-C). Inhibition of the PMd-cck projection to the dlPAG with green light decreased escape velocity in both assays (Figure 2.16D). This manipulation did not alter other defensive behaviors such as freezing or stretch-attend postures (Figure 2.16D). In contrast, inhibition of the PMd-cck projection to the amv did not change any defensive behavioral measure in either assay (Figure 2.16E). These data show that the activity in the PMd-cck projection to the dlPAG, but not to the amv, is necessary for normal escape vigor during exposure to both innate and conditioned threats.

PMd and dlPAG show increased mutual information during threat exposure

Having shown that inhibition of the PMd-dlPAG projection impairs escape from threat, we hypothesized these regions show increased functional connectivity during threat exposure. To test this view, using cck-cre mice, we injected AAV-FLEX-GCaMP6s in the PMd and AAV-syn-GCaMP6s in the dlPAG contralaterally, and implanted fiber optic cannula above each injection site to monitor the simultaneous calcium activity of these regions during threat and control assays (Figure 2.17A-C). Using the mutual information metric—an information-theoretic quantity that reflects the amount of information obtained for one variable by observing another variable—we found that the mutual information between the PMd and dlPAG is higher during exposure to threat

than control assays (see Methods for details). This was also true when escapes were removed, indicating that the mutual information change seen is related to threat exposure, rather than specific defensive behaviors (Figure 2.17D).

We opted to use mutual information instead of correlation because the former, but not the latter, can quantify both linear and non-linear relationships between two variables. Importantly, these dual-site recordings were done in PMd-cck cells and dlPAG-syn cells contralaterally.

As the PMd-cck projection to the dlPAG is unilateral (Figure 2.18)(N. S. Canteras and Swanson 1992), performing contralateral recordings ensures that dlPAG-syn cell body signals are not contaminated by signals from GCaMP-expressing PMd-cck axons terminating in the dlPAG. The dlPAG does not project to the PMd (Comoli, Ribeiro-Barbosa, and Canteras 2000), thus there is no risk of recording signals from GCaMP-expressing dlPAG axons in the PMd.

Hypothalamic-PAG functional connectivity increases in humans viewing aversive images

To investigate whether a functionally similar pathway exists in humans, we examined functional connectivity (i.e., covariation of BOLD signal in the hypothalamus and PAG) as participants received aversive stimulation during fMRI scanning (N = 48). We developed a predictive model to identify a pathway between the hypothalamus (HTH) and the PAG, which consisted of a multi-voxel pattern across brain voxels in each region optimized for maximal HTH-PAG covariation (Figure 2.19, see Methods). We then tested activation in this pathway in held-out participants. This HTH-PAG pathway responded more strongly to aversive images than non-aversive images and its activation also scaled monotonically with aversiveness (Figure 2.19C). Examination of the multi-voxel patterns contributing to the HTH-PAG pathway revealed that portions of medial posterior hypothalamus (neighboring the mammillary bodies) were most consistently associated with PAG activation. We also show that activation of the HTH-PAG pathway is selective and does

not correlate with activation of a different major subcortical input pathway to the PAG, such as the amygdala-PAG pathway (Figure 2.20).

Thus, these data show that functional connectivity in a hypothalamic-PAG pathway is increased in humans during aversive situations, in agreement with our results in mice showing that the hypothalamic to brainstem PMd-dlPAG pathway is engaged during exposure to aversive threats.

FIGURES

Chapter 2: Dorsal premammillary projection to periaqueductal gray controls escape vigor from innate and conditioned threats.

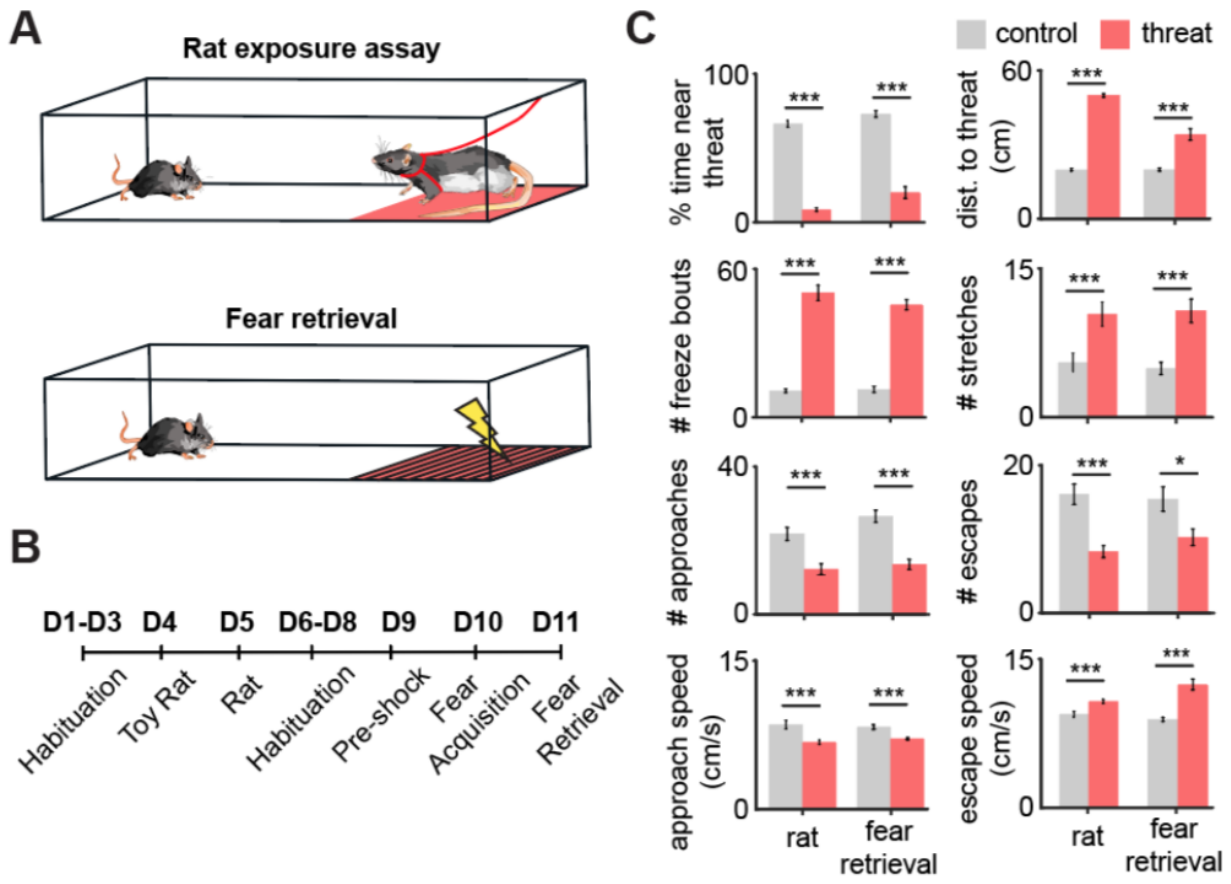

Figure 2.1. Rat and fear retrieval assays increased fear-related metrics.
(A) Schemes of (top) rat assay and (bottom) fear retrieval assay. The rat is restricted by a harness (shown in red) that is tied to the upper wall edge, and can only move in the pink area. In the shock grid assay mice freely explored a context with a shock grid for 3 daily sessions (pre-shock, fear acquisition and fear retrieval). Shocks were delivered only on fear acquisition day. All presented shock grid data is from fear retrieval. (B) Assays were performed in the order described (D=day). (C) Bars depict behavioral metrics (n=32), for rat and fear retrieval assays, both for control and threat conditions. Wilcoxon signed-rank test; *p<0.05, ***p<0.001.

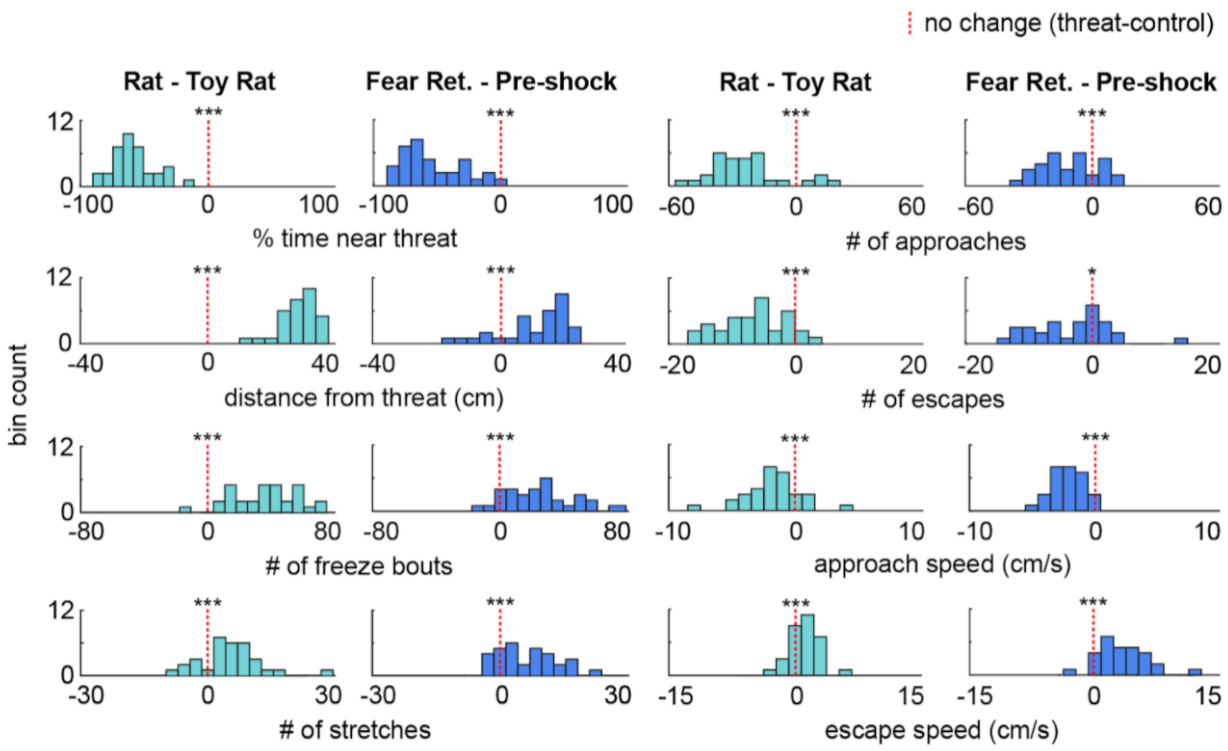

Figure 2.2. Distribution of the difference scores for threat - control assays.
Histograms depict the difference scores for all mice (threat - control) for each behavioral metric in Figure 1. (n=32 mice) * p<0.05, *** p<0.001.

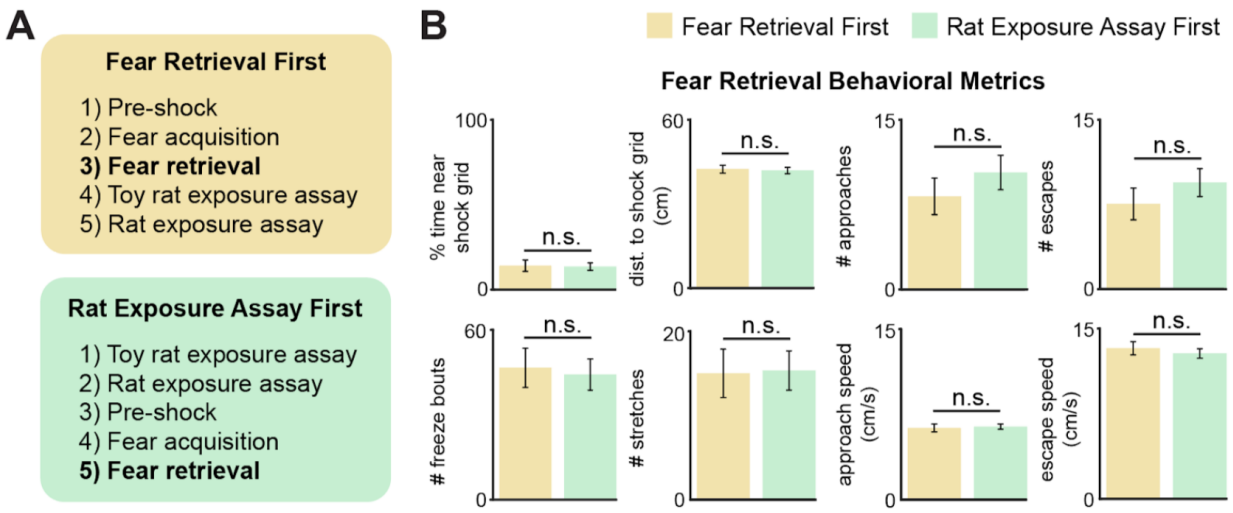

Figure 2.3. The order of threat exposure does not affect defensive behavioral metrics.
(A) Two cohorts of mice were exposed to the rat and shock grid threats in counterbalanced order, as specified in the blue and green boxes. (B) The defensive behavioral metrics of these two cohorts were compared for the fear retrieval assay. None of the tested metrics were different between groups (Wilcoxon rank-sum test; each group, n=9).

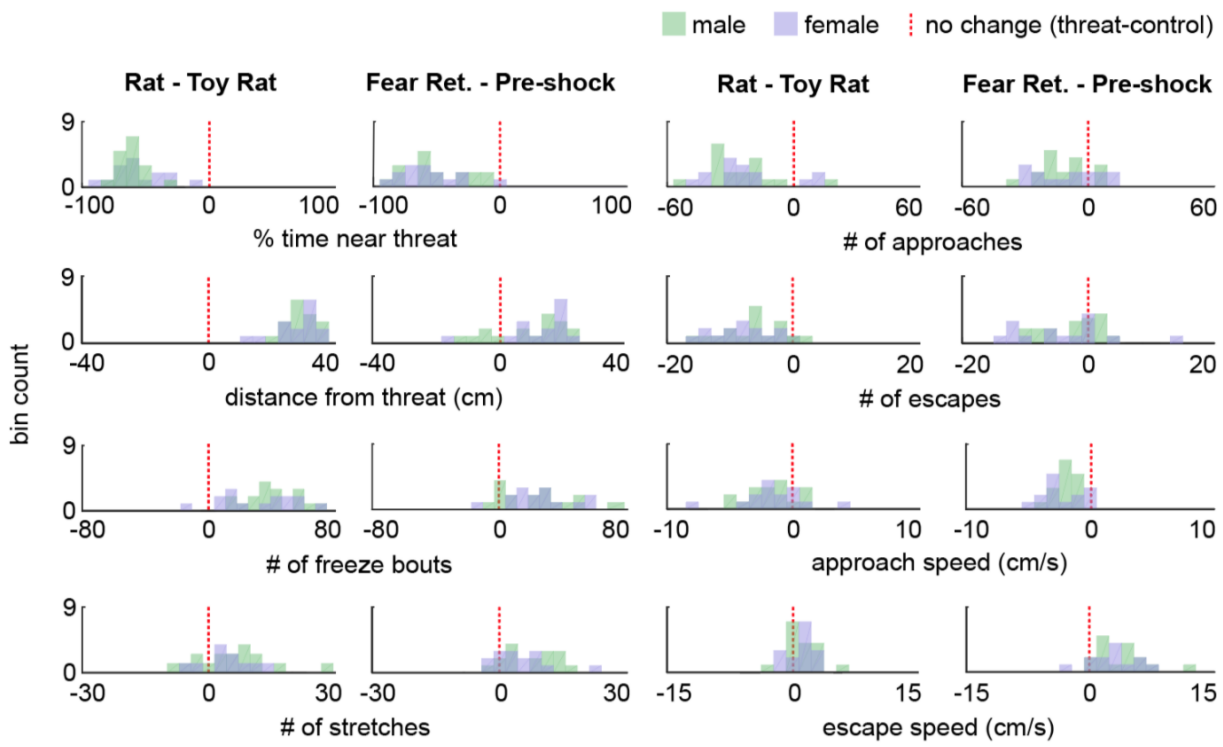

Figure 2.4. Distribution of the difference scores for threat - control assays for males and females.

Histograms depict the difference scores for all mice, threat - control, for each behavioral metric in Figure 1, separately for males (green) and females (purple). The dotted red line indicates zero, or no difference between threat and control (male n=17, female n=15). No significant differences ($p>0.05$) were found between males and females in any of the metrics plotted.

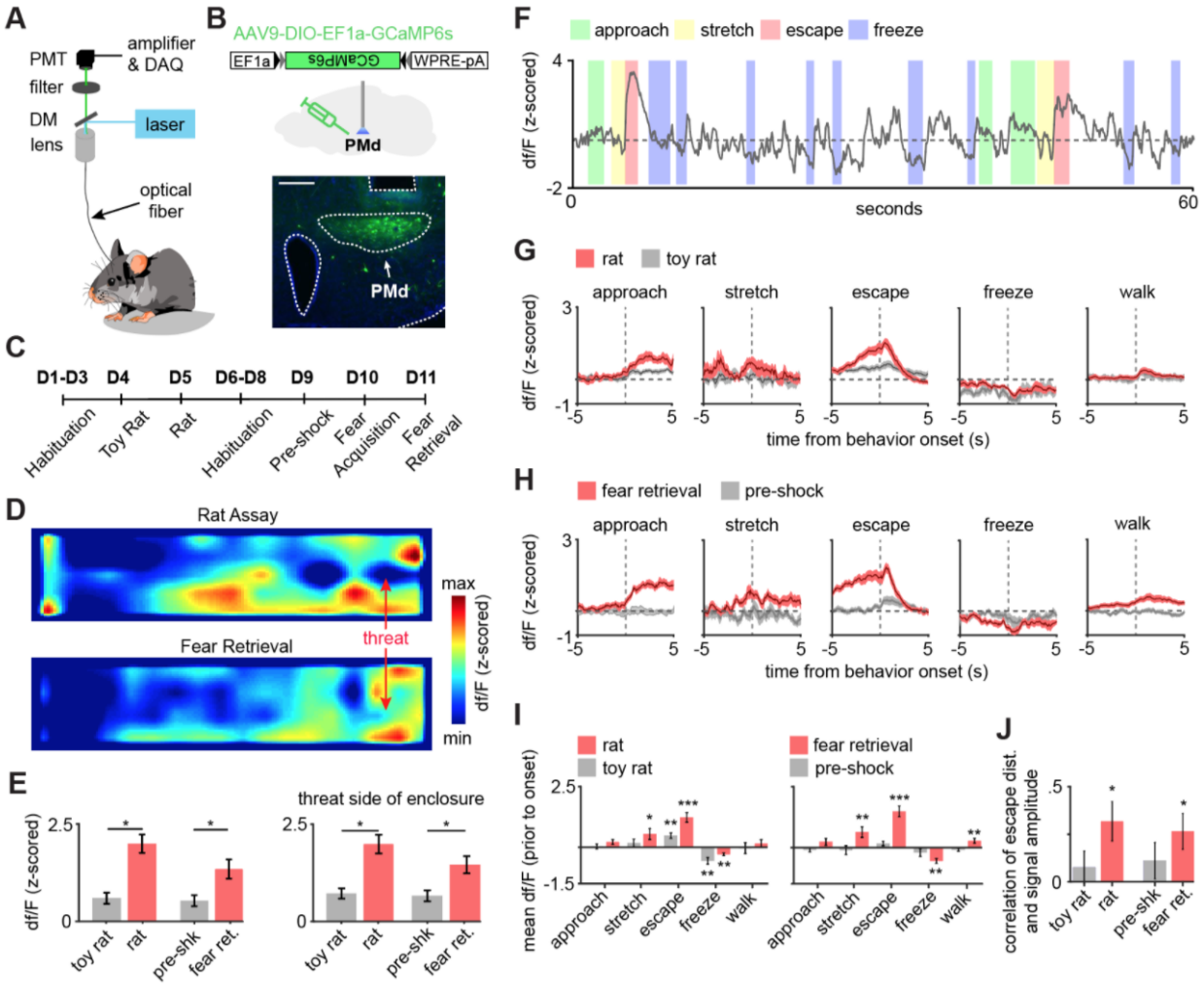

Figure 2.5. PMd-cck cells are activated by threats and escape.

(A) Scheme showing setup used to obtain fiber photometry recordings. (B) Expression of GCaMP6s in PMd-cck cells. (Scale bar: 200 μm) (C) Diagram depicts the behavioral protocol for each day (abbreviated as D). (D) Average heatmaps showing that PMd-cck cells are more active near a rat (top) and the shock grid (bottom) (for each, n=15). (E) Bar graphs quantifying average z-scored df/F during exposure to the toy rat, rat, pre-shock and fear retrieval. All data are shown for the same speed range (6-10 cm/s; Wilcoxon signed-rank test) (F) Example GCaMP6s trace from a representative mouse showing that PMd-cck cells are active during escape. (G) Behavior-triggered average showing mean PMd-cck activity during approach to rat, risk-assessment stretch-attend postures, escape and freeze. (n=15 mice) (H) Same as (G), but during exposure to the fear retrieval shock grid assay. (n=15 mice) (I) Bars show the mean df/F from -2 to 0 seconds from behavior onset for threat (red) and control (gray) assays. (Wilcoxon signed-rank test; n (left) same as (F); n (right) same as (G)) (I) Bars show the Spearman correlation of the mean fiber photometry signal amplitude and distance run for all escapes. (Wilcoxon signed-rank test). (E,I,J), n=15 mice, data is plotted as mean +/- s.e.m. *p<0.05, **p<0.01, ***p<0.001.

A

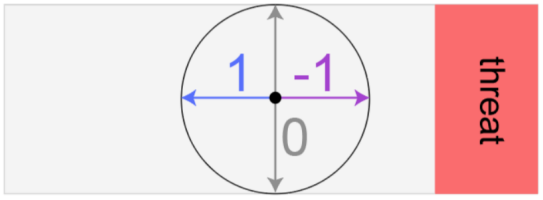

B

	Rat	Fear Retrieval
escape speed (cm/s)	11.17 ± 0.97	8.29 ± 0.63
escape duration (s)	3.13 ± 0.12	3.29 ± 0.15
escape count (#)	14.27 ± 1.92	7.33 ± 1.05
escape angle (cos(∠))	0.74 ± 0.11	0.76 ± 0.09
mean freeze bout duration (s)	2.50 ± 0.18	1.99 ± 0.13

Figure 2.6. Behavioral metrics for the PMd fiber photometry cohort during threat exposure assays.

(A) Diagram provides a description of the escape angle metric, here calculated as the cosine of the head direction in radians. A value of 1 indicates an escape parallel with the long walls of the enclosure. (B) Table shows pertinent defensive metrics during exposure to rat and fear retrieval assays for the PMd fiber photometry cohort. (n=15 mice).

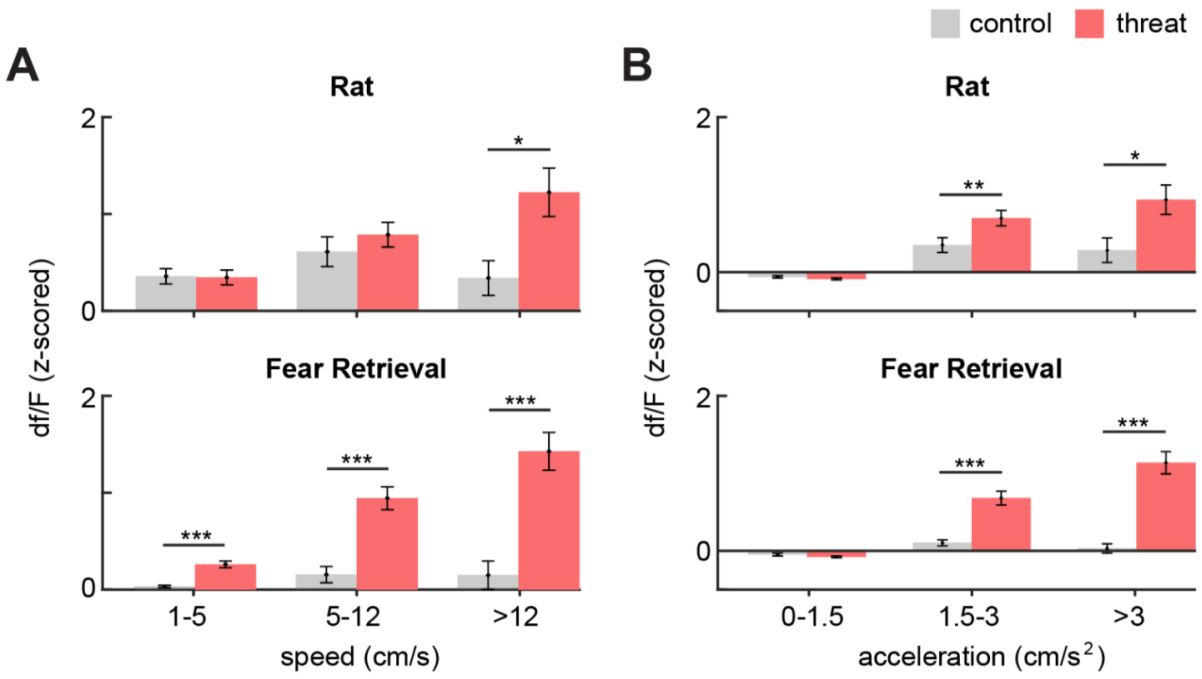

Figure 2.7. PMd-cck df/F for increasing speed and acceleration ranges.
Bars show the mean df/F (z-scored) for increasing ranges of (A) speed and (B) acceleration. (Wilcoxon signed-rank test; n=15) * p<0.05, ** p<0.01, *** p<0.001.

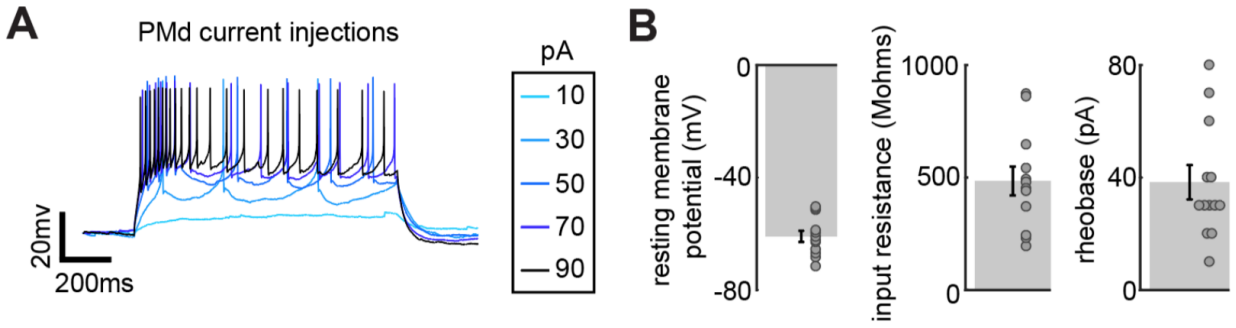

Figure 2.8. Characterization of PMd-cck cell biophysical properties in acute slices. Mice from a cck-cre driver line were injected with cre-dependent viral vectors encoding YFP in the PMd. Acute slices were prepared from these mice and YFP-expressing cells in the PMd were used to measure biophysical properties of PMd-cck cells. (A) Injection of current triggers action potentials in PMd cells. (B) Average resting membrane potential, input resistance and rheobase in PMd cells (n=12 cells).

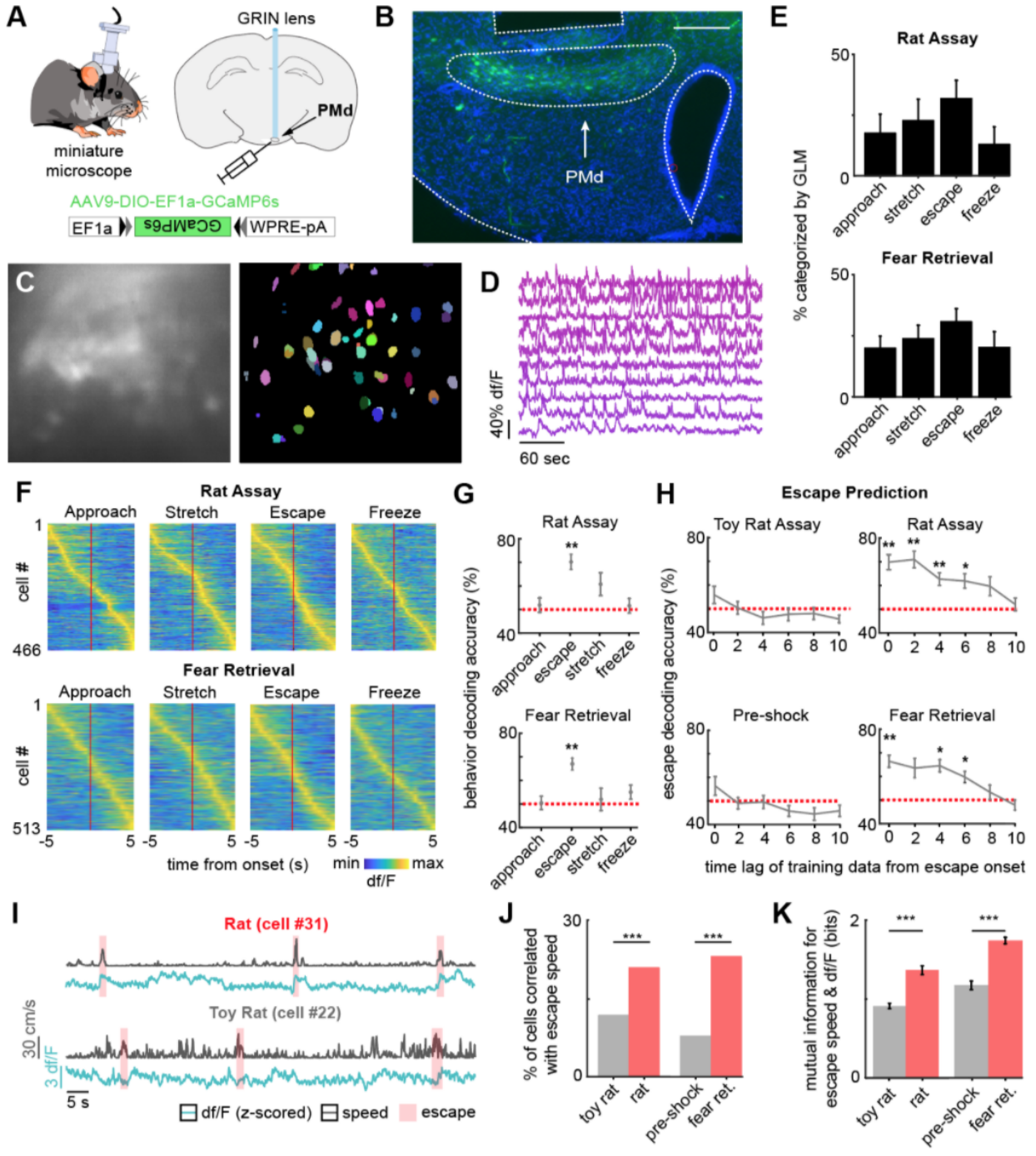

Figure 2.9. PMd-cck ensemble activity can predict escape in rat and shock grid fear retrieval assays.

(A) PMd-cck mice were injected with AAV9-DIO-EF1a-GCaMP6s in the PMd and then were implanted with a miniaturized microscope. (B) Photo of the GCaMP6s in PMd-cck cells and location of implanted GRIN lens. (Scale bar 200 μm) (C) (left) Maximum projection of the PMd field of view in an example mouse. (right) Extracted cell contours for the same session. (D) Representative traces of a subset of calcium transients from GCaMP6s-expressing PMd-cck cells

recorded in a single session. (E) Generalized linear models (GLMs) were used to determine GLM weights for defensive behaviors. Cells were classified as activated by each behavior based on their actual GLM weights compared to the distribution of weights generated by permuting the neural data. (n=9 mice) (F) Colormaps show average activation for each PMd-cck cell for each scored behavior in the rat (top) and shock grid fear retrieval (bottom) assays. Cells are sorted by time of peak activation. (G) Ongoing escape, but not other behaviors, can be decoded by PMd-cck cell activity in the rat (top) and shock grid fear retrieval assays (bottom) (Mice that displayed less than 5 instances of a given behavior were removed from the analysis: (top) approach n=7, stretch n=6, escape n=7, freeze n=6; (bottom) approach n=5, stretch n=4, escape n=5, freeze n=3; Wilcoxon signed-rank test). (H) PMd-cck cell activity can predict escape from threats, but not control stimuli, several seconds prior to escape onset. (toy rat n=8 mice, rat n=7, pre-shock n=5, fear retrieval n=5). (n=466 cells in rat assay, n=513 cells in shock grid fear retrieval assay; Wilcoxon signed-rank test) (I) Traces show the z-scored df/F (blue) and speed (gray) for one cell classified as a speed cell in the rat exposure assay (top) and one non-correlated cell from the toy rat assay (bottom). Individual escape epochs are indicated by red boxes. (J) Bars show the percentage of cells that significantly correlate with escape speed. (Fisher's exact test; toy rat: n correlated = 56, n non-correlated = 405; rat: n correlated = 100, n non-correlated = 366; pre-shock: n correlated = 50, n non-correlated = 571; fear retrieval: n correlated = 122, n non-correlated = 391) (K) Bars show the mutual information in bits between escape speed and calcium activity for cells whose signals were significantly correlated with escape speed in (J). (Wilcoxon rank sum test; toy rat n=56, rat n=100; pre-shock n=50, fear retrieval n=122). ***$p<0.001$, **$p<0.01$, *$p<0.05$.

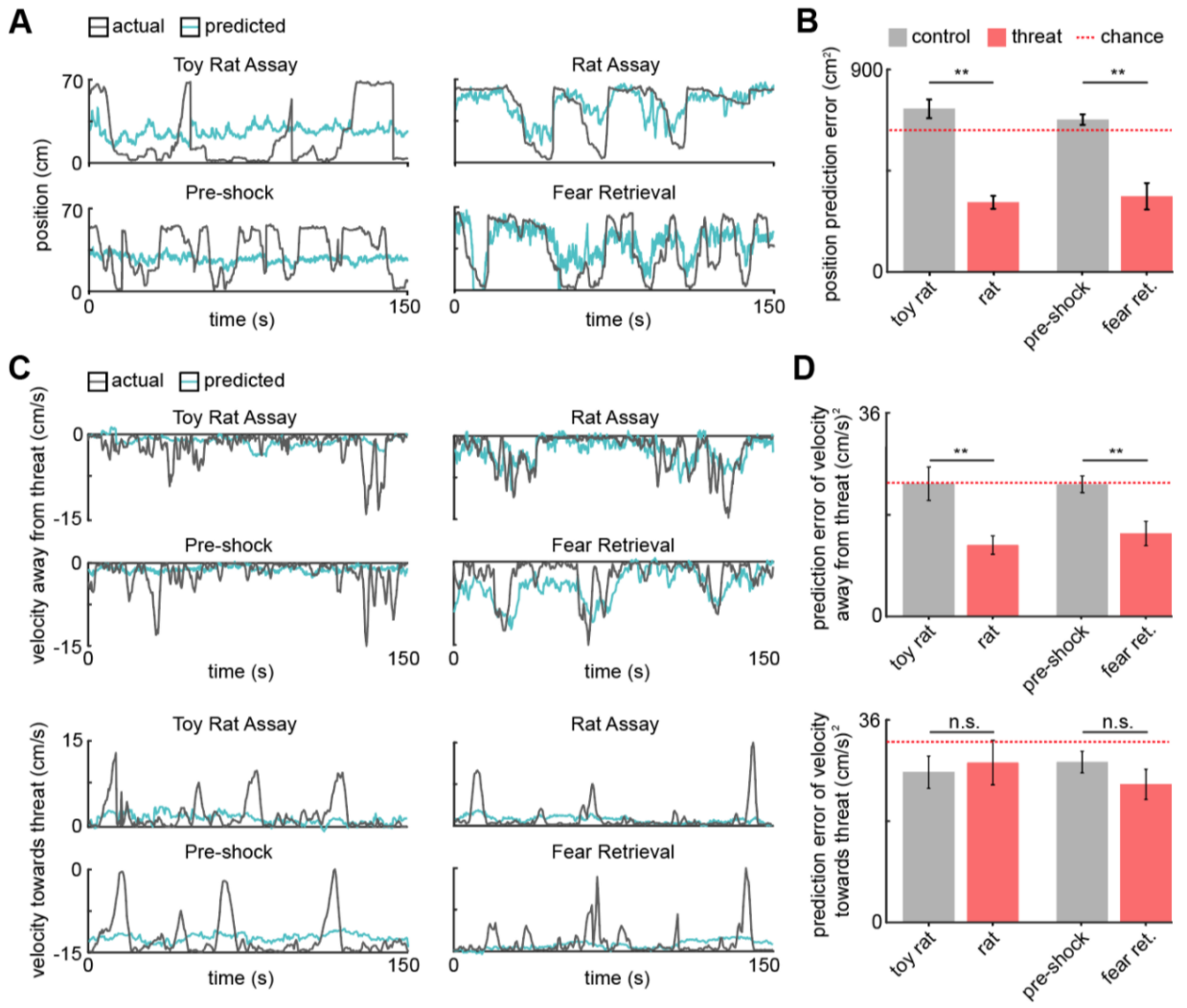

Figure 2.10. PMd ensemble activity represents distance from threat and escape velocity. (A) A general linearized model (GLM) was used to decode the position of each animal along the length of the enclosure from the neural data. The line plots depict the actual location (gray line) and GLM-predicted location (blue line) from example toy rat/rat and pre-shock/fear retrieval sessions. Note that the predicted location is more accurate for threat than control assays. (B) Bars show the mean squared error (MSE) of the GLM-predicted location from the actual location. The MSE is significantly lower for threat than control assays (Wilcoxon signed-rank test; n=9 mice). The dotted red line indicates chance error, calculated by training and testing the GLM on circularly permuted data. Only threat assay error was significantly lower than chance (Wilcoxon signed-rank test; rat $p<0.001$, fear retrieval $p=0.003$) (C) Similar to (A), a GLM was used to predict the velocity away from (top) and towards (bottom) the threat in a representative mouse. (D) Similar to (B), bars depict the MSE of the GLM-predicted velocity away from (top) and towards (bottom) the threat. The GLM more accurately decodes threat than control velocities for samples in which the mice move away from the threat (top). As in (B), only threat assay error was significantly lower than chance (Wilcoxon signed-rank test; rat $p=0.004$, fear retrieval $p=0.012$). The accuracy does not differ in threat and control assays for samples in which the mice move towards the threat (bottom). (Wilcoxon signed-rank test; n=9 mice) ** $p<0.01$.

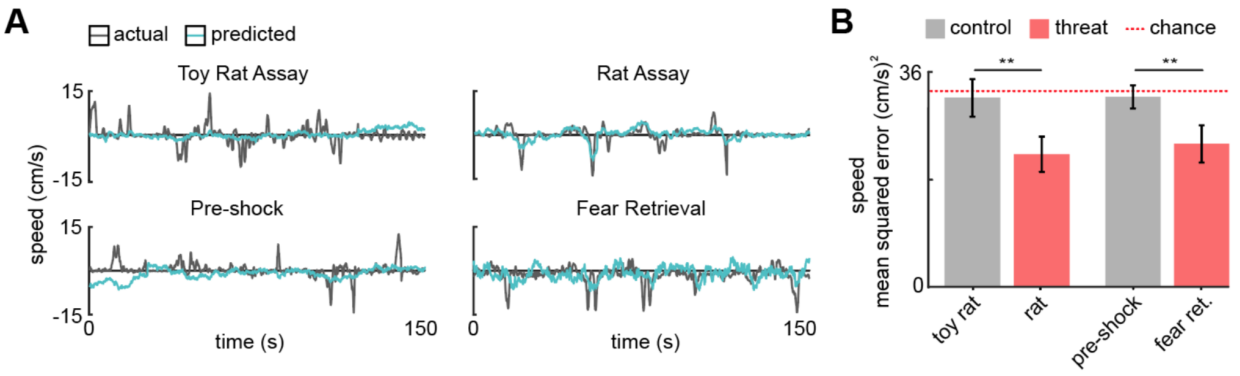

Figure 2.11. PMd ensemble activity represents speed in threat assays.
(A) A generalized linear model (GLM) was used to predict the speed of a representative mouse. (B) Bars depict the mean squared error of the GLM-predicted speed. The GLM more accurately decodes threat than control speeds. The dotted red line indicates chance error, calculated by training and testing the GLM on circularly permuted data. Only threat assay error was significantly lower than chance (rat $p<0.020$, fear retrieval $p=0.040$). (Wilcoxon signed-rank test; n=9 mice) ** $p<0.01$.

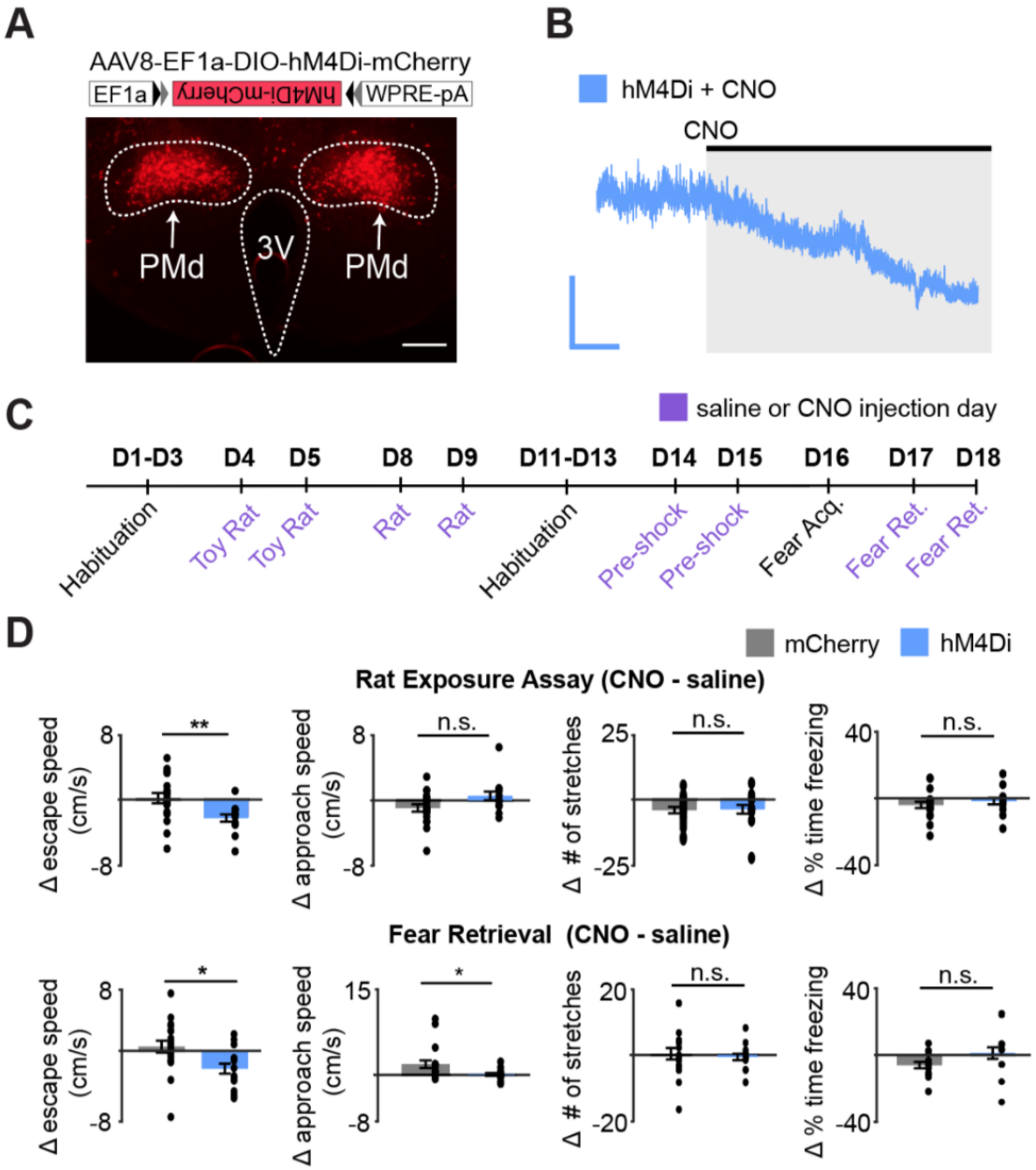

Figure 2.12. Chemogenetic inhibition of PMd-cck cells decreases escape speed from threats.

(A) Cck-cre mice were injected with cre-dependent vectors encoding hM4Di-mcherry, or -mcherry in the PMd (top). Expression of hM4Di-mcherry in PMd-cck cells (bottom). (scale bar: 200 μm) (B) Ex vivo slice recordings showing that clozapine-N-oxide (CNO) hyperpolarized PMd-cck cells expressing hM4Di. (scale bar: 60s, 10 mV) (C) Mice were exposed to each assay twice, in the order shown, after receiving i.p. injections of either saline or CNO. (D) Inhibition of hM4Di-expressing PMd-cck cells decreased escape speed in the rat and fear retrieval assays. (rat exposure assay mCherry/hM4Di n=19/n=11; fear retrieval assay mCherry/hM4Di n=19/n=12; Wilcoxon signed-rank test) **p<0.01, *p<0.05.

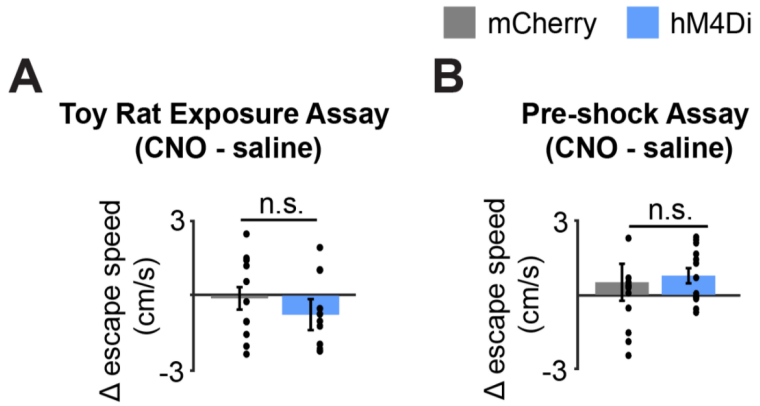

Figure 2.13. Inhibition of PMd-cck cells does not affect escape speed in control assays. (A) Bars depict the change in escape speed (CNO-saline) during toy rat exposure assay (Wilcoxon rank-sum test; mCherry/hM4Di n=7/n=8). (B) Bars depict the change in escape speed (CNO-saline) during pre-shock assay (Wilcoxon rank-sum test; mCherry/hM4Di n=7/n=12).

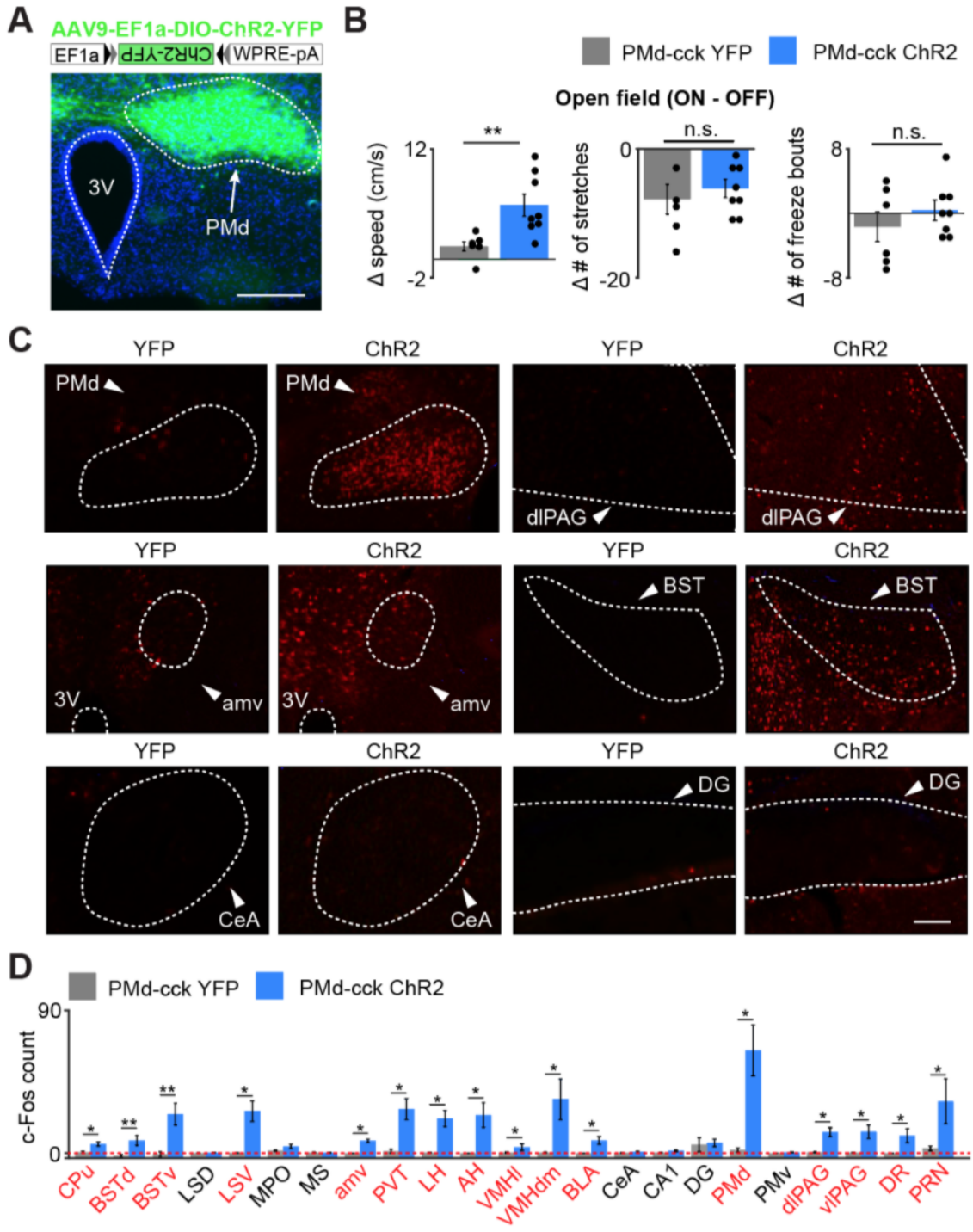

Figure 2.14. Optogenetic PMd-cck activation increases velocity and recruits widespread defensive networks.

(A) Cck-cre mice were injected with AAV9-Ef1a-DIO-ChR2-YFP in the PMd (top). Expression of Chr2-YFP in PMd-cck cells (bottom; scale bar: 200 μm) (B) Delivery of blue light increases speed in PMd-cck ChR2 mice, but not stretch-attend postures or freeze bouts. (PMd-cck YFP n=6, PMd-cck ChR2 n=8; Wilcoxon rank-sum test). (C) Following optogenetic activation of PMd-cck cells

mice were perfused and stained with antibodies against the immediate early gene cfos. Representative images show that blue light delivery caused increased fos expression in the PMd, bed nucleus of the stria terminalis (BST) and anteromedial ventral thalamus (amv). Other regions, such as the central amygdala (Cea) and the dentate gyrus (DG) did not show increased fos expression following PMD-cck optogenetic stimulation. (scale bar: 100 μm) (D) Average number of fos-expressing cells in various brain regions following light delivery to ChR2 (blue) or YFP (gray)-expressing cells. Regions for which the c-Fos count is significantly greater for ChR2 than YFP mice are labelled in red. (Wilcoxon rank-sum test; For all regions, PMd-cck YFP n=5, PMd-cck ChR2 n=4 except for BSTd and BSTv: YFP n=8, ChR2 n=8) *$p<0.05$, **$p<0.01$. Abbreviations: CPu (caudate-putamen), BSTd/v (dorsal and ventral bed nucleus of the stria terminalis), LS D/V (dorsal and ventral lateral septum), MPO (medial preoptic area), amv (anteromedial ventral thalamus), PVT (paraventricular nucleus of the hypothalamus), LH (lateral hypothalamus), AH (anterior hypothalamus), VMHvl/dm (ventrolateral and dorsomedial portions of the ventromedial hypothalamus), BLA (basolateral amygdala), CeA (central amygdala), CA1 (hippocampal cornus ammonis 1), DG (dentate gyrus), PMd (dorsal premammillary nucleus), PMv (ventral premammillary nucleus), dlPAG (dorsolateral periaqueductal gray), vlPAG (ventrolateral periaqueductal gray), DR (dorsal Raphe), PRN (pontine reticular nucleus).

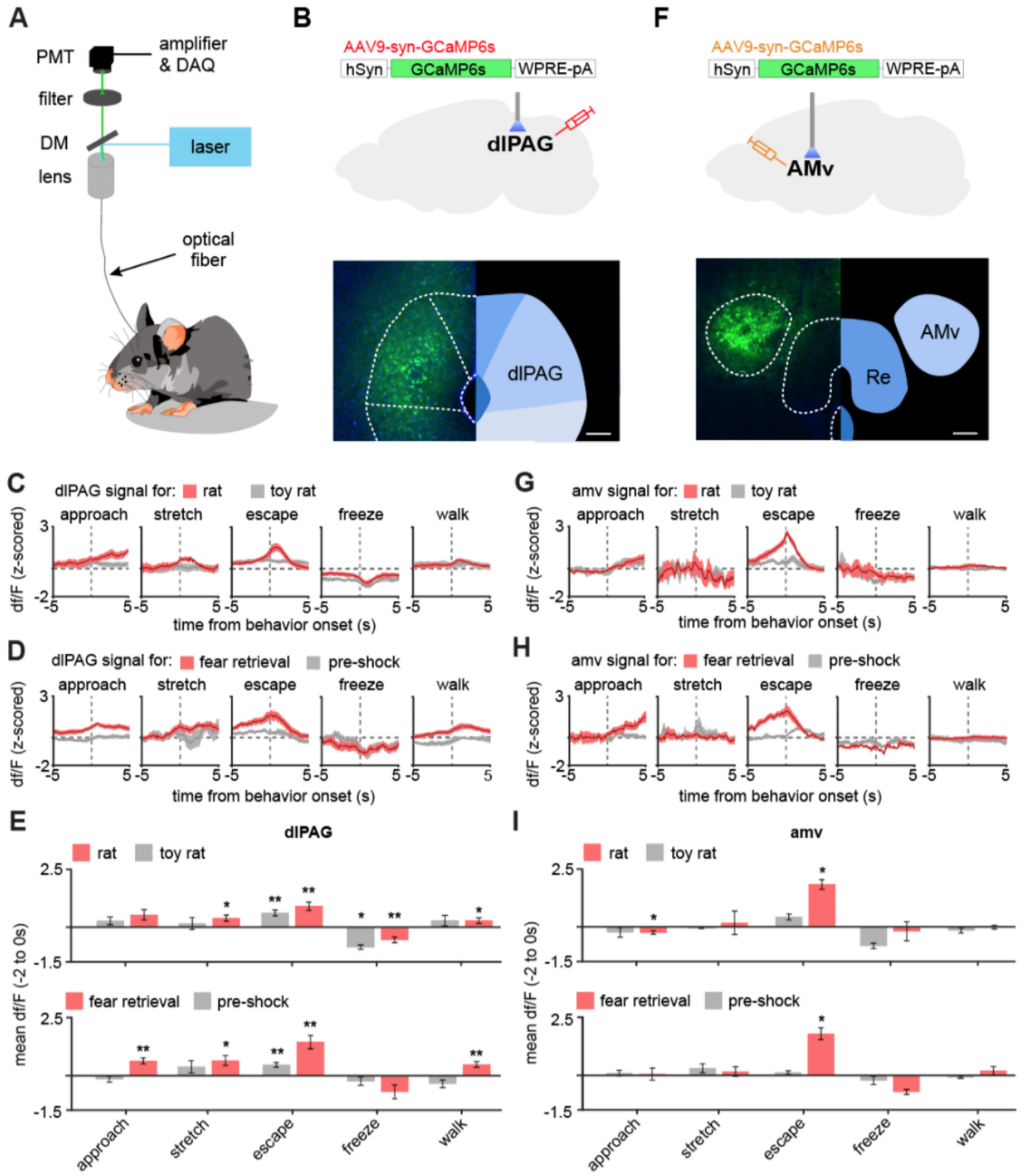

Figure 2.15. The dlPAG and AMV are activated by threats and escape.
(A) Scheme showing setup used to obtain fiber photometry recordings. (B) Expression of GCaMP6s in the dlPAG. (Scale bar: 150µm) (C) Behavior-triggered average showing mean dlPAG activity during approach to rat, risk-assessment stretch-attend postures, escape, freeze and walking perpendicularly to the rat at the safe side of the enclosure. (n=9 mice) (D) Same as (C), but during exposure to the fear retrieval shock grid assay. (n=9 mice) (E) Bars show the mean

df/F from -2 to 0 seconds from behavior onset for threat (red) and control (gray) assays. (n=9 mice). (F-I) Same as (B-E), but for the amv. (F) Scale bar: 150μm (G-I) n=6 mice. (E,F) Wilcoxon signed-rank test; **p<0.01, *p<0.05.

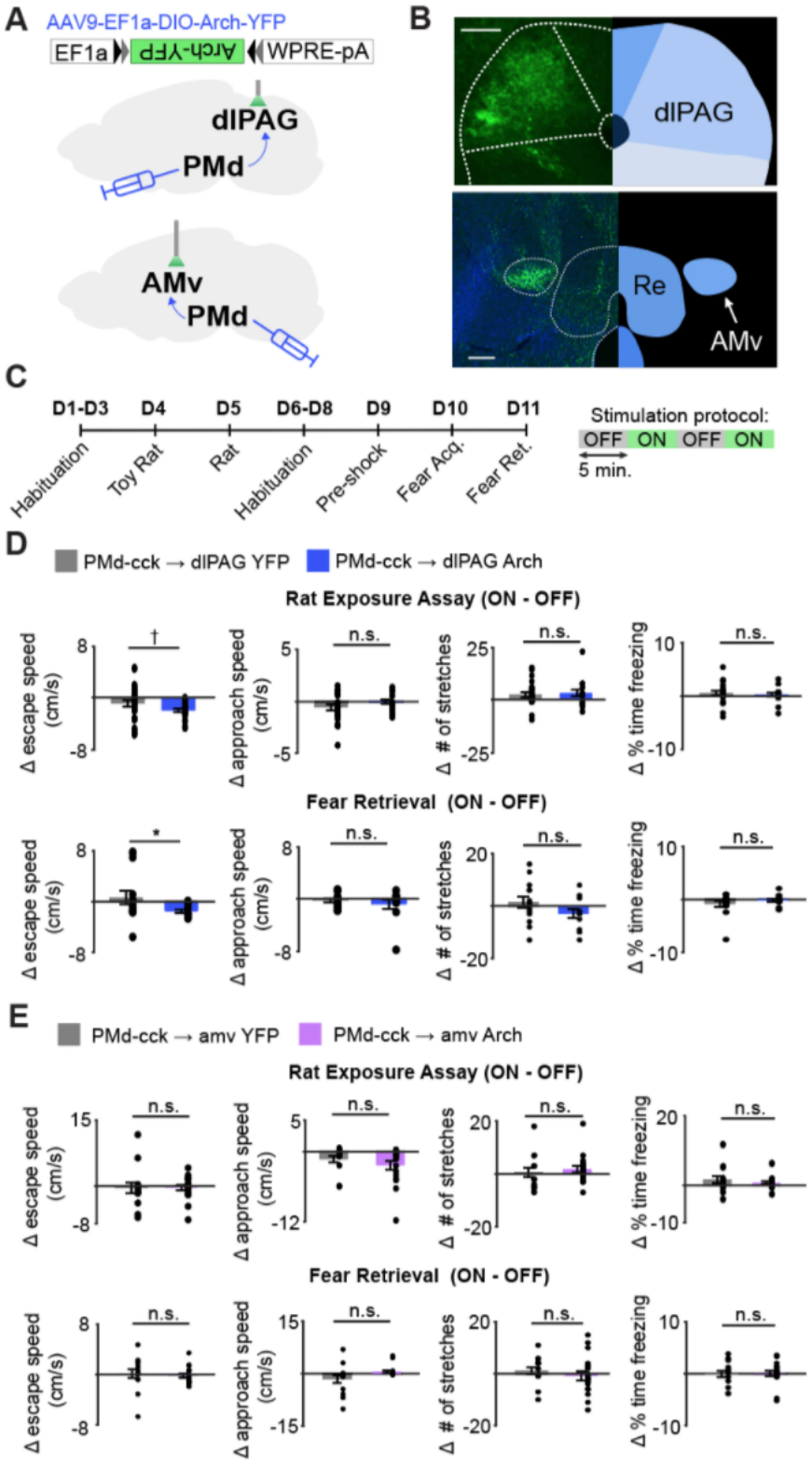

Figure 2.16. Optogenetic inhibition of the PMd-cck projection to the dlPAG, not the amv, decreases escape velocity during exposure to innate and conditioned threats.

(A) Viral vectors were used to express Arch in PMd-cck cells. Fiber optic cannula were bilaterally implanted over PMd-cck arch-expressing axon terminals in the amv or dlPAG. (B) Image showing PMd-cck axon terminals expressing arch-YFP in the dlPAG and amv. (Scale bars: 150μm) (C) Summary diagram showing order of assays and green light delivery protocol. (D) Inhibition of the PMd-cck projection to the dlPAG decreased escape speed, but not other defensive behaviors. (Wilcoxon rank-sum test; (top) rat exposure assay: YFP/Arch n=24/n=12; (bottom) fear retrieval: YFP/Arch n=14/n=11) (E) Inhibition of the PMd-cck projection to the amv did not alter any of the behavioral measures monitored. (Wilcoxon rank-sum test; (top) rat exposure assay: YFP/Arch n=12/n=18; (bottom) fear retrieval: YFP/Arch n=12/n=17), *$p<0.05$; † $p=0.058$.

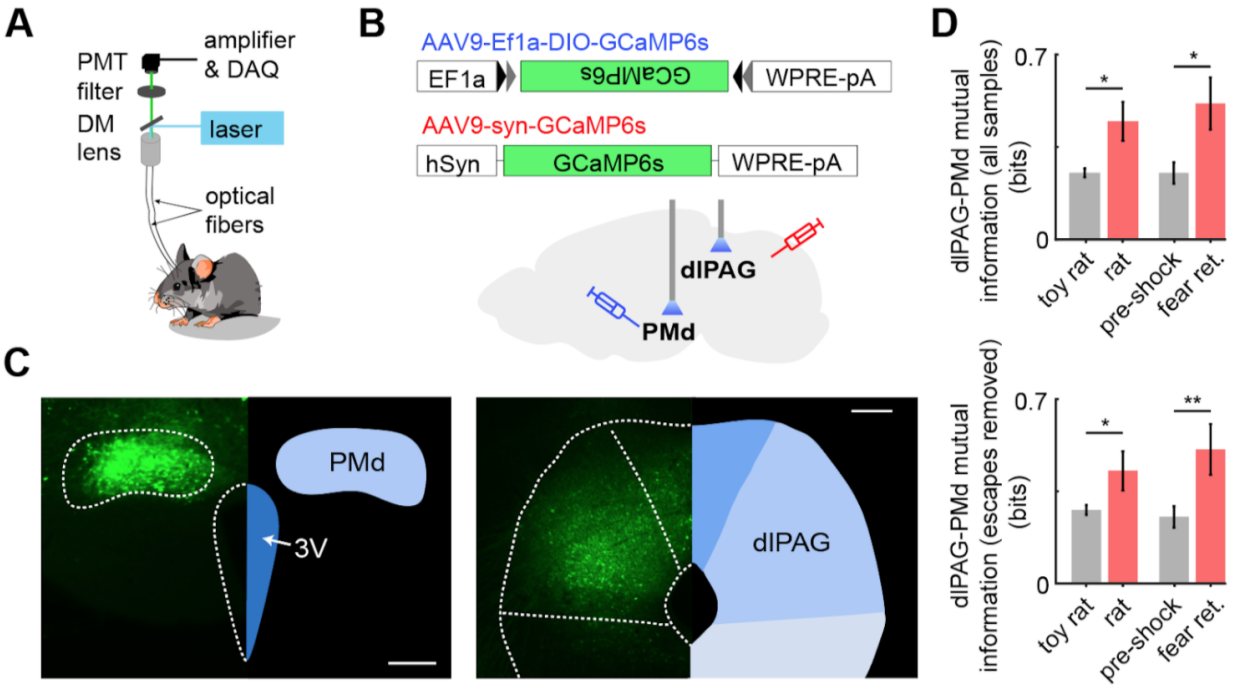

Figure 2.17. Dual fiber photometry signals from the PMd and dlPAG exhibit increased mutual information during threat exposure.

(A) Scheme showing setup used to obtain dual fiber photometry recordings. (B) PMd-cck mice were injected with AAV9-Ef1a-DIO-GCaMP6s in the PMd and AAV9-syn-GCaMP6s in the dlPAG. (C) Expression of GCaMP6s in the PMd and dlPAG. (Scale bars: (left) 200 μm, (right) 150 μm) (D) Bars show the mutual information between the dual-recorded PMd and dlPAG signals, both including (left) and excluding (right) escape epochs, during exposure to threat and control. Mutual information is an information theory-derived metric denoting the amount of information obtained for one variable by observing another variable. See Methods section for more details. * $p<0.05$, ** $p<0.01$.

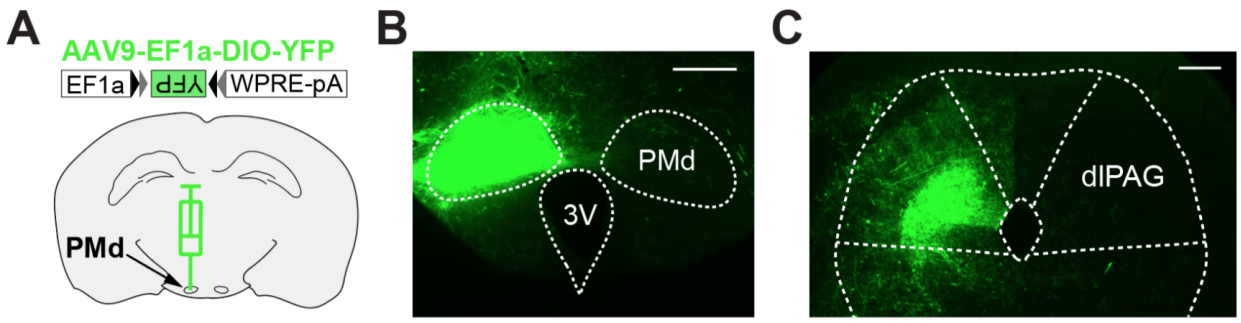

Figure 2.18. PMd-cck neurons project unilaterally to the dlPAG.
(A) Cck-cre mice were injected with AAV9-Ef1a-DIO-YFP in the left PMd. (B) Image shows the expression of YFP in PMd-cck cells only in the left side. (scale bar: 200 μm) (C) PMd-cck axon terminals unilaterally express YFP in the dlPAG only on the left side. (scale bar: 150μm).

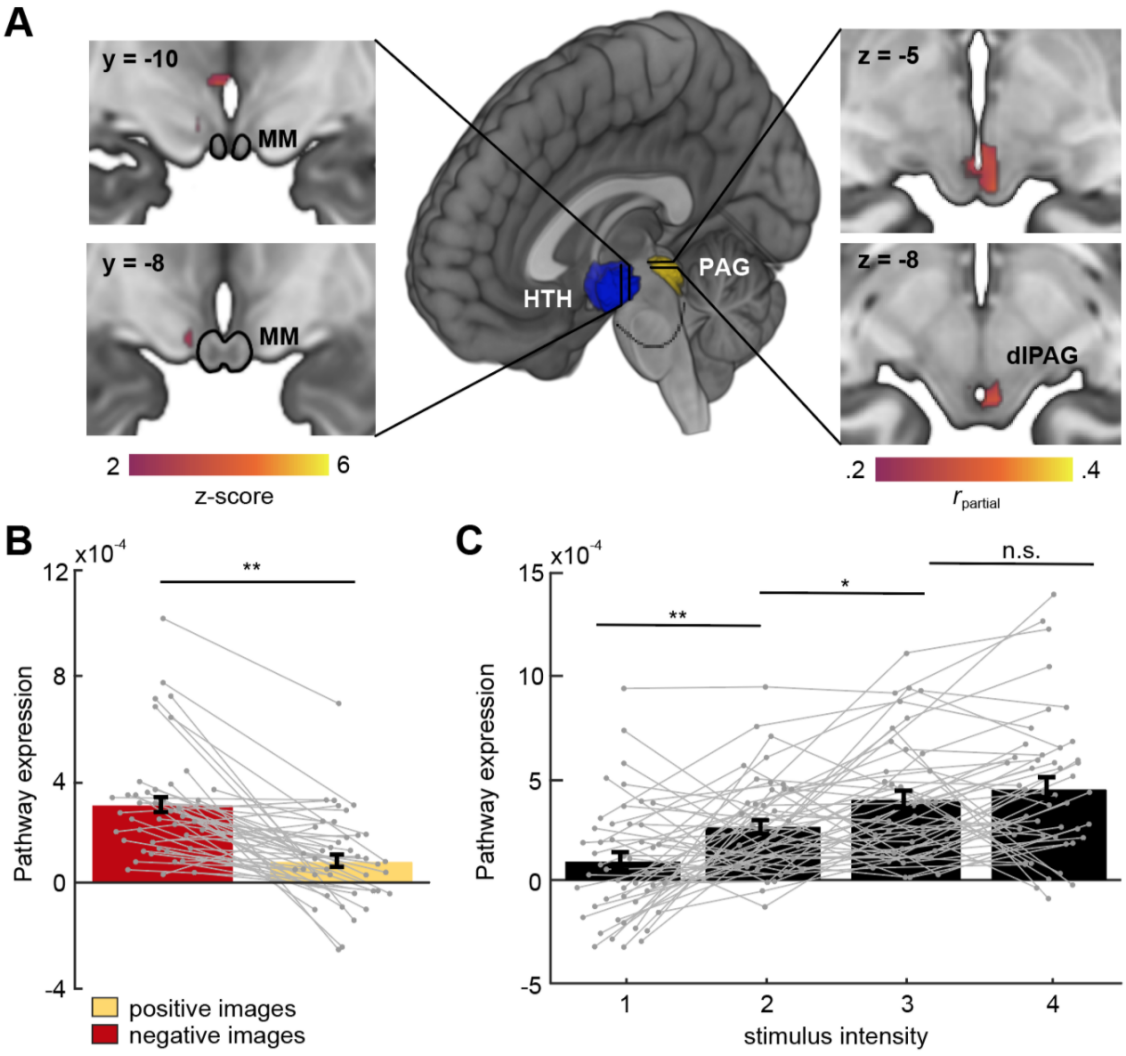

Figure 2.19. Hypothalamus(HTH)-PAG pathway is sensitive to aversive visual stimuli in humans.

(A) Multivariate brain pathway estimated using activation in the hypothalamus (HTH, rendered in blue) to predict patterns of activation in the periaqueductal gray (PAG, rendered in yellow). Inserts depict statistical maps indicating which regions of the HTH covaried most strongly with the PAG (left) and portions of dorsal PAG (dlPAG) that were explained by the HTH but not a pathway from the central amygdala. The mammillary bodies (MM) are depicted with a black outline. Note that all hypothalamus voxels are included in the model, only suprathreshold voxels are shown here. (B) Average bar plot showing that the HTH-PAG pathway was more active during exposure to threat (aversive visual images) compared to control stimuli (non-aversive, positive images). Each circle corresponds to an individual subject. (C) Pathway expression monotonically increased as a function of stimulus intensity. Inference on brain maps is based on bootstrap resampling of regression coefficients from pathway estimation (left) and partial correlation coefficients (right). All maps are thresholded at $q_{FDR} < .05$. (Wilcoxon signed-rank test, n = 48 participants) **p<0.001, *p<0.01.

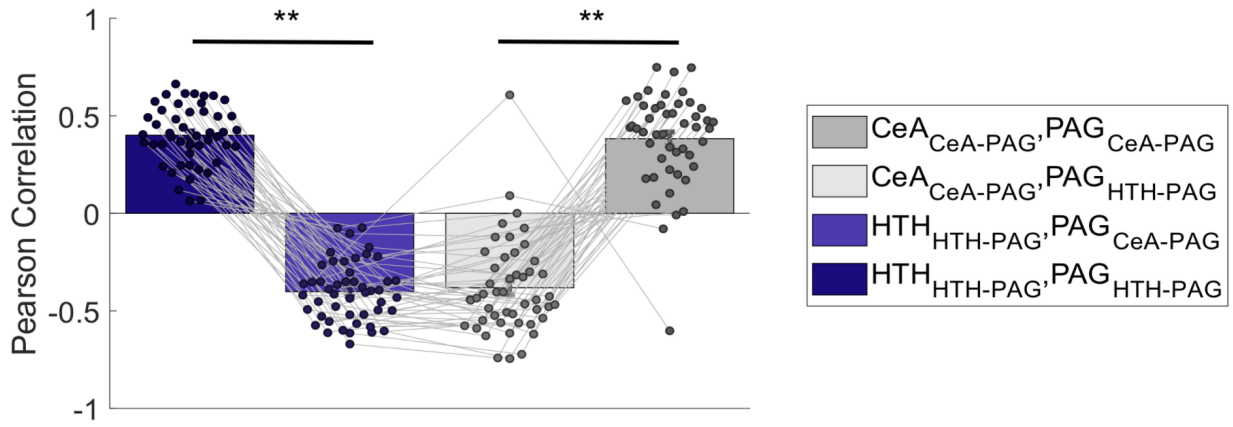

Figure 2.20. Multi-voxel response patterns in the PAG related to hypothalamus (HTH) and central amygdala (CeA) are functionally distinct.

The HTH pattern optimized for PAG connectivity ([$HTH_{HTH\text{-}PAG}$]) correlates positively with its respective PAG pattern ([$PAG_{HTH\text{-}PAG]}$) in 100% of test subjects (dark blue), but negatively with a PAG pattern optimized to covary with CeA ([$PAG_{CeA\text{-}PAG}$]; light blue). Conversely, The CeA pattern optimized for PAG connectivity ([$CeA_{CeA\text{-}PAG}$]) correlates positively with its respective PAG pattern in in >90% of test subjects ([$PAG_{CeA\text{-}PAG}$]; dark gray), but negatively with a PAG pattern optimized to covary with HTH ([$PAG_{HTH\text{-}PAG}$]; light gray). This double dissociation shows that the HTH-PAG and CeA-PAG pathways are functionally distinct in human participants, and even oppose one another. Each circle corresponds to an individual subject. Wilcoxon signed-rank test; **p<0.001. (n=48 participants)

DISCUSSION

Chapter 1. Coordination of escape and spatial navigation circuits orchestrate versatile flight from threats.

We show the PMd is critical for versatile context-specific escape. This skill is crucial for escape that requires coordination of spatial navigation and flight, such as when animals flee a predator in a jungle or humans evacuate a building in flames. The PMd is anatomically well-suited for this role, as it is interconnected with threat detection, escape and navigation-related regions (N. S. Canteras and Swanson 1992; Comoli, Ribeiro-Barbosa, and Canteras 2000). Thus, the PMd may detect multiple threat modalities and then induce context-specific escape by engaging spatial navigation nodes.

PMd induces context-specific escape by engaging thalamic and brainstem outputs

We propose the PMd engages the dlPAG to initiate escape in diverse threatening situations, and that simultaneous engagement of spatial navigation circuits via the amv leads to flexible context-specific flight. However, in the presence of overwhelming threat, the PMd no longer recruits the amv (Figure 1.14K, 1.16D and Figure 1.17D). This difference in PMd functional connectivity may be related to the shift towards panic jumping, despite the presence of a more efficient climbing route that allows longer relief from CO_2 (Figure 1.2I). Indeed, panic induces suboptimal flight (Elliott and Smith 1993; Helbing, Farkas, and Vicsek 2000; J.-Q. Shen, Wang, and Jiang 2018; Keating 1982).

The unsupervised Hidden Markov method identified a prominent network state in the PMd that predicted escape (Figure 1.10H). Remarkably, this result could be found by separating the data into only two states, showing that escape-related network states are a key feature of PMd activity.

PMd escape-modulated cells also displayed stronger activation prior to context-specific escapes compared to panic-related jumping in CO_2 (Figure 1.10M). These data may indicate that cells related to context-specific escape fire considerably prior to flight onset to provide enough time for downstream circuits to identify optimal escape routes and plan appropriate motor actions. We also observed PMd-cck cell activity peaks after jumps in the CO_2 assay (Figure 1.10K). This activity may be related to controlling escape vigor, as reported for dlPAG cells firing after escape onset (Evans et al. 2018).

Though dlPAG stimulation has analgesic properties, PMd stimulation did not alter analgesia (Figure 1.3B). PMd excitation may not activate analgesia-mediating endocannabinoid pathways in the dlPAG (Gregg et al. 2012). Indeed, defensive behaviors and analgesia are controlled by separate vlPAG neurons (Tovote et al. 2016).

The PMd is an extremely understudied nucleus, despite providing the densest known input to the panicogenic dlPAG (Del-Ben and Graeff 2009; Lovick 2000; Tovote et al. 2016). PMd activation may produce aversion and motivation to escape via the dlPAG, while activation of the amv projection may lead to mobilization of downstream cortical circuits that integrate contextual cues. This specificity arises because amv-projecting PMd cells, despite also projecting to the dlPAG (Figures 1.12,1.13), are functionally distinct from cells that exclusively project to the dlPAG. Indeed, amv-projecting cells are only active during context-specific escape, but not jumps in CO_2, while the projection to dlPAG is active during all escapes (Figure 1.16). Accordingly, inhibition of the amv projection impaired only context-specific escape, while inhibition of the dlPAG projection decreased flight in general (Figure 1.17).

Our data show that the PMd does not generate complex flight by its own temporal coding, as the same optogenetic stimulation parameters resulted in different context-specific actions (Figure 1.6B-C). Instead, downstream circuits likely generated the motor plans for context-specific escapes. The amv may serve these functions by its direct projections to navigation regions such as the entorhinal cortex and action-planning structures such as the secondary motor cortex (Jankowski et al. 2013). Indeed, the amv is necessary for the acquisition of predator-induced contextual fear (Carvalho-Netto et al. 2010), making it a good candidate to coordinate defensive responses associated with spatial memory, such as context-specific escapes. Thus, our data suggest a model according to which PMd activation creates an aversive signal via the dlPAG projection that motivates escape. A context-specific escape is induced only if the amv-projecting PMd cells are also activated, leading to the elaboration of versatile flight motor plans integrating relevant contextual cues to identify and use appropriate escape routes.

Distributed networks controlling escape

The PMd receives input from a wide variety of sources that support a role for this nucleus in context-specific escape elicited by threats such as predators or CO_2. It receives input from other predator-responsive nuclei such as the VMHdm and the anterior hypothalamus and also from CO_2 -detecting structures such as the orexinergic perifornical region (Comoli, Ribeiro-Barbosa, and Canteras 2000). Lastly, the PMd receives connections from the prefrontal cortex, which may provide input related to executive control and also from the nucleus of Gudden, a region critical for contextual memory and spatial navigation (Comoli, Ribeiro-Barbosa, and Canteras 2000). Input from these various sources may allow the PMd to detect a wide variety of threats and engage downstream dlPAG and amv outputs to produce appropriate context-specific defensive responses.

We show that inhibition and excitation of PMd-cck cells respectively decreased and increased context-specific and panic-related escape. Interestingly, DMH and VMHdm activation did not elicit context-specific escape climbing (Figures 1.4, 1.5). However, these regions control escape in simple environments (Johnson and Shekhar 2012; Johnson et al. 2008; L. Wang, Chen, and Lin 2015), indicating that the PMd's ability to mediate both context-specific and panic-related escape may be relatively unique. Indeed, though we activated several hypothalamic regions implicated in escape (Figure 1.9), only optogenetic stimulation of the PMd caused escape in a novel complex environment (Figure 1.6C). Electrical dlPAG stimulation (E. J. Kim et al. 2013) produced escape to a burrow in the end of a corridor in a simple box. However, optogenetic dlPAG stimulation did not cause escape from the complex upwards step box (Figure S5G), showing that the dlPAG may produce directed escape provided that the action is relatively simple and does not require sophisticated navigation. Similarly, stimulation of sf1+ VMHdm cells also causes escape and flight (Kunwar et al. 2015; L. Wang, Chen, and Lin 2015), in agreement with our results showing freezing and jumps during VMHdm stimulation (Figure S3E-G). These cells encode complex environments (Krzywkowski, Penna, and Gross 2020), suggesting they may control complex context-specific escape, as stimulating these cells produces flight towards a hiding area (L. Wang, Chen, and Lin 2015). Though sf1+ VMHdm stimulation did not consistently produce escape in the upwards step box (Figure 1.4G), one mouse was able to escape, indicating that direct input from these cells to the PMd may have a role in context-specific escape. Indeed, the VMHdm provides robust input to the PMd (Comoli, Ribeiro-Barbosa, and Canteras 2000) and is part of the hypothalamic predator-detection circuit with the PMd (Cezario et al. 2008; Silva et al. 2013), suggesting these two structures have related functions. Perhaps different stimulation parameters may have induced more organized escape following activation of dlPAG or sf1 VMHdm cells.

PMd-mediated escape was seen using numerous threats, different routes and distinct escape motor plans, pointing towards a general role of the PMd in versatile context-specific escape, a

vital skill needed to ensure escape and survival from imminent threats (Perusini and Fanselow 2015). We also report that the PMd recruits both escape-inducing circuits and spatial navigation networks, showing how these two functions are integrated to produce context-specific escape.

Chapter 2. Dorsal premammillary projection to periaqueductal gray controls escape vigor from innate and conditioned threats.

As previously described, the PMd is anatomically the source of the most prominent input to the dlPAG (Del-Ben and Graeff 2009; Lovick 2000; Tovote et al. 2016), and a wealth of evidence from diverse streams of data have demonstrated that the dlPAG controls escape (Del-Ben and Graeff 2009; Tovote et al. 2016). Recent work has also shown that the dlPAG controls escape vigor (Evans et al. 2018). Taken together, these data indicate that the PMd is anatomically well-situated to modulate escape vigor from threats. Furthermore, optogenetic activation of PMd-cck cells activates a broad network of regions involved in defensive behaviors (Figure 2.14D). Our fos data show PMd-cck cell optogenetic activation recruited a plethora of areas known to mediate defense, such as the basolateral amygdala, the lateral septum and the bed nucleus of the stria terminalis. These results indicate that PMd-activation potentially may affect a wide range of defensive behaviors by engaging these networks.

Our previous data in Chapter 1 showed that activation of the PMd-dlPAG pathway caused escape from innate threats (W. Wang et al. 2021). However, those data did not show if this circuit controlled escape vigor (measured by flight velocity) or if it affected escapes from conditioned threats. We now show PMd-cck cells play a key role in controlling escape vigor, during exposure to both innate and conditioned threats. We show that PMd-cck cells were activated by threat proximity (Figure 2.5E and 2.10B), and that their activity predicted future escape (Figure 2.9H) and represented escape velocity, but not approach velocity (Figure 2.10D). Furthermore,

inhibition of either PMd-cck cells (Figure 2.12) and of the PMd-cck to dlPAG inhibition decreased escape velocity (Figure 2.16). These data demonstrate the PMd-cck projection to the dlPAG is critical for modulating escape velocity from threats, which is a behavior of paramount importance for survival. Importantly, all of the results described above are novel and were not shown in prior reports about the PMd (W. Wang et al. 2021).

Interestingly, PMd-cck cells also represented distance to threat, but not distance to control stimuli (Figure 2.10). PMd input to the dlPAG may thus contribute to the encoding of distance to threat and related kinematic variables in dlPAG cells as we recently reported (Reis et al., 2021 and Reis et al., 2021). Prior work using excitotoxic PMd lesions and local infusions of muscimol in rats reported large decreases in freezing (Cezario et al. 2008). In contrast, our chemogenetic inhibition of PMd-cck cells in mice revealed only deficits in escape. These differences may be either due to differences in species or due to off-target effects of muscimol infusions in adjacent nuclei that control freezing, such as the ventromedial hypothalamus (L. Wang, Chen, and Lin 2015). Our data add to a growing stream of results showing how different components of the medial hypothalamic defense system control threat-induced behaviors, in a densely interconnected network containing the anterior hypothalamus, the ventromedial hypothalamus and the PMd (Cezario et al. 2008).

Interestingly, our data show that the PMd, as well as the dlPAG participate in defensive responses elicited by both innate and shock-based conditioned threats. The dlPAG has mostly been studied as a region that initiates escape from innate threats, such as looming stimuli (Evans et al. 2018). However, prior evidence has also implicated the dlPAG in conditioned defensive behavior. For example, the dlPAG is activated during exposure to shock-conditioned auditory tones and contexts (Carrive et al. 1997; Watson et al. 2016). Furthermore, neurotransmission of cannabinoids (Resstel et al. 2008), CRF (Borelli et al. 2013), glutamate and nitric oxide (Aguiar

et al., 2014) have been shown to be necessary for contextual freezing. However, involvement of the dlPAG or the PMd in controlling escape behavior from conditioned stimuli such as shock grids is less well-understood.

We now show that the PMd-cck projection to the dlPAG modulates escape velocity from conditioned threats, broadening the role of this circuit to include escape from learned threats. More recently, we showed that dlPAG cells represent distance from a learned conditioned threatening shock grid during fear retrieval, further supporting a role for this region in mediating defense induced by conditioned threats (Reis et al. 2021). The dlPAG is bidirectionally connected with diverse forebrain regions (Motta, Carobrez, and Canteras 2017), while the PMd receives strong input from the medial prefrontal cortex (Comoli, Ribeiro-Barbosa, and Canteras 2000), which may explain how these regions respond to conditioned threats. Intriguingly, during contextual fear retrieval tests, rats showed increased PMd fos expression if they had free access to the conditioning chamber, but not if they were confined to this chamber (Viellard, Baldo, and Canteras 2016). Information about innate predatory threats are likely conveyed to the PMd by other members of the hypothalamic predatory defense circuit, such as the VMHdm and the anterior hypothalamus (Comoli, Ribeiro-Barbosa, and Canteras 2000; Cezario et al. 2008; Silva et al. 2013). Future studies are needed to determine which specific inputs to the PMd convey information about conditioned threats. Nevertheless, our data show that the PMd-dlPAG circuit is not merely responding to external threatening sensory cues. Rather, the involvement of this circuit in escape from conditioned stimuli during fear retrieval shows that these structures can be affected by long-term fear memories, illustrating that evolutionarily ancient structures can also display experience-dependent roles in behavior.

Intriguingly, data from Chapter 1 of this manuscript show that optogenetic inhibition of the PMd-amv projection decreased the number of escapes elicited by a predator rat in environments

requiring sophisticated three dimensional spatial navigation to escape. However, PMd-amv activity was not necessary for stereotyped jumps in the presence of the panicogenic agent CO_2 (Wang et al, 2021). One interpretation of these data is that this pathway is necessary only for escape from medium intensity threat modalities (such as a rat), but not from extremely high imminence threat such as CO_2. A second interpretation is that the PMd-amv pathway is only necessary for escapes that require spatial navigation, regardless of the threat modality. We now show inhibition of the PMd-cck projection to the amv did not alter any defensive behavioral metrics induced by a rat in a simple environment (Figure 2.1), where the animal does not need a complex three-dimensional understanding of the environmental layout to escape (Figure 2.16D). In the current assay, simply running away from the rat in any direction is sufficient to escape. As inhibition of the PMd-amv projection impaired escape from a predatory rat only when flight required complex navigation, we argue that the role of this circuit is related to complex navigation during threat exposure, supporting our second interpretation above. These data are in agreement with prior work that indicate the amv's role in defensive behavior is related to contextual memory-associated behaviors rather than the execution of escape or freezing (Carvalho-Netto et al. 2010).

Intriguingly, our fMRI data indicate that a hypothalamic-PAG pathway has increased activity in humans viewing aversive images (Figure 2.19). A homologous functional pathway to the rodent PMd-dlPAG may exist in humans that is at least partially identifiable from fMRI data. We used a novel application of Partial Least Squares to identify local multi-voxel patterns that functionally connected HTH and dlPAG. In out-of-sample tests in new participants, HTH and dlPAG were positively correlated in every participant and tracked the reported intensity of negative emotion elicited by images. The resolution of imaging in humans does not allow us to specify which hypothalamic nucleus is involved. However, the location of the nucleus is in the posterior medial hypothalamus, similar to the rodent PMd, suggesting the possibility that a circuit analogous to the PMd-dlPAG projection may exist in humans. It is not feasible to directly study functional

connectivity in humans during actual escape from threats, so we were limited to collecting data during exposure to aversive images. Despite these limitations, these data are compatible with rodent data showing the PMd is activated by a wide variety of aversive stimuli such as bright lights and loud noises (D. J. Kim et al. 2017). Furthermore, the fMRI data are in agreement with our data showing in mice PMd-cck and dlPAG activity show increased mutual information in the presence of threat, relative to control conditions even after removing all samples with escape (Figure 2.17).

Taken together, our data indicate that the PMd-cck projection to the dlPAG modulates escape velocity during exposure to both innate and conditioned threats, and the results suggest a similar pathway may be active during exposure to aversive situations in humans.

METHODS

EXPERIMENTAL MODEL AND SUBJECT DETAILS

All procedures conformed to guidelines established by the National Institutes of Health and have been approved by the University of California, Los Angeles Institutional Animal Care and Use Committee, protocols 2017-011 and 2017-075.

Mice. Cck-IRES-Cre mice (Jackson Laboratory stock No. 012706), SF1-cre (Jackson Laboratory stock No. 012462) and wild type C57BL/6J mice (Jackson Laboratory stock No. 000664) were used for all experiments. Male and female mice between 2 and 6 months of age were used in all experiments. Mice were maintained on a 12-hour reverse light-dark cycle with food and water ad libitum. Sample sizes were chosen based on previous behavioral optogenetics studies on defensive behaviors, which typically use 6-15 mice per group. All mice were handled for a minimum of 5 days prior to any behavioral task.

Rats. Male Long-Evans rats (250-400 grams) were obtained from Charles River Laboratories and were individually housed on a standard 12-hour light-dark cycle and given food and water *ad libitum*. Rats were only used as a predatory stimulus. Rats were handled for several weeks prior to being used and were screened for low aggression to avoid attacks on mice. No attacks on mice were observed in this experiment.

METHOD DETAILS

Viral Vectors.

Optogenetics: The following adeno-associated viral vectors (AAV), used in the optogenetic experiments, were purchased from Addgene (Watertown, MA): AAV9.hSyn.eGFP.WPRE.bGH, AAV9.Syn.DIO.EGFP.WPRE.hGH, AAV9.hSyn.hChR2.(H134R)-eYFP.WPRE.hGH,

AAV9.EF1a.DIO.hChR2(H134R)-eYFP.WPRE.hGH, AAV9-EF1a-DIO-eYFP and AAV9-FLEX-Arch-GFP.

Chemogenetics: The following AAVs, used in the chemogenetic experiments, were purchased from Addgene: pAAV8-hSyn-DIO-hM4D(Gi)-mCherry, AAV8.Syn.DIO.HM3D(Gq)-mCherry, and AAV8.Syn.DIO.mCherry.

Fiber Photometry: AAV9.Syn.GCaMP6s.WPRE.SV40 and AAV9.Syn.FLEX.GCaMP6s.WPRE.SV40, used in the fiber photometry experiments, were purchased from Addgene.

Surgeries. Surgeries were performed as described previously (Adhikari et al. 2015). Eight-week-old mice were anaesthetized with 1.5-3.0% isoflurane and placed in a stereotaxic apparatus (Kopf Instruments). A scalpel was used to open an incision along the midline to expose the skull. After performing a craniotomy, 40 nl of AAV9.hSyn.hChR2.(H134R)-eYFP.WPRE.hGH at a titer of 2*1012 particles/ml was injected per site (PMd or other hypothalamic and brainstem nuclei) using a 10 µl nanofil syringe (World Precision Instruments) at 0.08 µl/min. The syringe was coupled to a 33-gauge beveled needle, and the bevel was placed to face the anterior side of the animal. The syringe was slowly retracted 20 minutes after the start of the infusion. Mice received unilateral viral infusion and fiber optic cannula implantation. Infusion locations measured as anterior-posterior, medial-lateral and dorso-ventral coordinates from bregma were: anterior hypothalamus (-0.7, -0.4, -5.2), dorsomedial hypothalamus (-1.94, -0.5, -5.3), ventromedial hypothalamus (-1.5, -0.4, -5.5), lateral hypothalamus (-2.46, -1.1, -5.2) dorsolateral periaqueductal gray (dlPAG) (-4.75, -0.45, -1.9), posterior hypothalamus (-2.30, -0.3, -4.5), dorsal premammillary nucleus (PMd) (-2.46, -0.5, -5.35). For arch experiments and dual photometry assays the dlPAG coordinates were (-4.6, -1.05, -2.1 using a 15-degree angle). Fiber optic cannula (0.22 NA, 200 µm diameter; Doric Lenses) were implanted unilaterally 0.15 mm above the viral infusion sites. Only mice with opsin expression restricted to the intended targets were used for behavioral assays. For

optogenetic experiments in PMd-cck mice, the same PMd coordinates were used to inject 0.16 uL of AAV9.EF1a.DIO.hChR2(H134R)-eYFP.WPRE.hGH or AAV9.EF1a.DIO.eYFP.WPRE.hGH. For chemogenetic experiments mice received 0.16 uL of pAAV8-hSyn-DIO-hM4D(Gi)-mCherry, AAV8.Syn.DIO.HM3D(Gq)-mCherry, or AAV8.Syn.DIO. mCherry in the PMd or dorsomedial hypothalamus coordinates. Similar AAV8-based vectors have been validated and used by numerous other researchers (T. A. Wang et al. 2019; Jiang-Xie et al. 2019; J. Shen et al. 2019; Hardaway et al. 2019).

For photometry experiments mice were injected with 0.16 uL of AAV9.Syn.GCaMP6s.WPRE.SV40 and AAV9.Syn.Flex.GCaMP6s.WPRE.SV40 in the dlPAG and PMd, respectively of cck-cre mice. Mice were implanted unilaterally with cannulae in the PMd and the dlPAG. A 400 μm diameter, 0.48 NA optical fiber (Neurophotometrics) was used for photometry experiments. Adhesive cement (C&B metabond; Parkell, Edgewood, NY, USA) and dental cement (Stoelting, Wood Dale, IL, USA) were used to securely attach the fiber optic cannula to the skull. Half the mice in each cage were randomly assigned to YFP/mcherry or ChR2 /Arch/hM4Di/hM3Dq groups. For miniaturized microscope experiments 40 nL of AAV9-DIO-GCaMP6s was injected in the PMd of cck-cre mice and a GRIN lens was implanted 200 uM above the infusion site. Three weeks following surgery animals were base-plated.

The rats used in this study were obtained from a partner lab and never optogenetically stimulated during the described assays. The rats had fiber optic cannulae implants from prior unrelated experiments. For details of the surgery, see (Malvaez et al., n.d.). Briefly, rats were anesthetized with isoflurane and bilaterally infused with AAV5-CaMKIIa-hChR2(H134R)-eYFP or AAV8-CaMKIIa-eYFP. Viral infusion (0.30 μl) was performed at a rate of 6 μl/hr by an infusion needle at

the lateral or medial orbitofrontal cortex. Optical fibers (200 μm core, numerical aperture 0.66; Prizmatix, Southfield, MI) positioned in ferrules (Kientec Systems Inc., Stuart, FL) were implanted 0.3 mm above the basolateral amygdala (AP −3.0 mm, ML ± 5.1, DV −7.7).

In situ hybridization. Cck-IRES-Cre mice (Jackson Laboratory stock No. 012706) were euthanized with 5% isoflurane followed by cervical dislocation. Brains were harvested and snap-frozen in 2-methylbutane at -20°C and tissue was sectioned at 18 μm. The workflow was performed in accordance with the manufacturer's protocol for the RNAScope® Multiplex Fluorescent Assay (Advanced Cell Diagnostics, Newark, CA). Riboprobes selective for sequences were labeled as follows: Cre (C1, Cat. No. 312281), nNOS with (437651-C2) and NeuN (Mm-Rbfox3-C3, Cat No. 313311-C3) or VGLUT2 (Mm-Slc17a6-C3, Cat No. 319171-C3). Images were obtained with a Leica DM5500 fluorescent microscope at 40x.

Immunostaining for NeuN. Fixed brains were kept in 30% sucrose at 4oC overnight, and then sectioned on a cryostat (40 μm) slices. Sections were washed in PBS and incubated in a blocking solution (3% normal donkey serum and 0.3% triton-x in PBS) for 1 hour at room temperature. Sections were then incubated at 4oC for 12 hours with polyclonal anti-NeuN antibody made in rabbit (1/500 dilution) (CAT# NBP1-77686SS, Novusbio) in blocking solution. Following primary antibody incubation sections were washed in PBS 3 times for 10 minutes, and then incubated with anti-rabbit IgG (H+L) antibody (1/500 dilution) conjugated to Alexa Fluor 594 (red) (CAT# 8889S, cellsignal.com) for 1 hour at room temperature. Sections were washed in PBS 3 times for 10 minutes, incubated with DAPI (1/50000 dilution in PBS), washed again in PBS and mounted in glass slides using PVA-DABCO (Sigma).

Acute brain slice preparation and electrophysiological recordings. Acute brain slices preparation and electrophysiological recordings were performed using standard methods as previously described (Nagai et al. 2019). Briefly, Cck-Cre+ mice that had received AAV microinjections into PMd were deeply anesthetized with isoflurane and decapitated with sharp shears. The brains were placed and sliced in ice-cold modified artificial CSF (aCSF) containing the following (in mM): 194 sucrose, 30 NaCl, 4.5 KCl, 1 $MgCl_2$, 26 $NaHCO_3$, 1.2 NaH2PO_4, and 10 D-glucose, saturated with 95% O_2 and 5% CO_2. A vibratome (DSK-Zero1) was used to cut 300 µm brain sections. The slices were allowed to equilibrate for 30 minutes at 32-34°C in normal aCSF containing (in mM); 124 NaCl, 4.5 KCl, 2 $CaCl_2$, 1 $MgCl_2$, 26 $NaHCO_3$, 1.2 NaH_2PO_4, and 10 D-glucose continuously bubbled with 95% O_2 and 5% CO_2. Slices were then stored at 21–23°C in the same buffer until use. All slices were used within 2-6 hours of slicing.

Slices were placed in the recording chamber and continuously perfused with 95% O_2 and 5% CO_2 bubbled normal aCSF. pCLAMP10.4 software and a Multi-Clamp 700B amplifier was used for electrophysiology (Molecular Devices). Whole-cell patch-clamp recordings were made from neurons in the PMd or dorsolateral PAG (dlPAG) using patch pipettes with a typical resistance of 4–5 MΩ. Neurons were selected based on reporter fluorescence, i.e. YFP for ChR2-YFP and mCherry for hM3Dq-mCherry or hM4Di-mCherry. The intracellular solution for recordings comprised the following (in mM) : 135 potassium gluconate, 5 KCl, 0.5 $CaCl_2$, 5 HEPES, 5 EGTA, 2 Mg-ATP and 0.3 Na-GTP, pH 7.3 adjusted with KOH. The initial access resistance values were < 20 MΩ for all cells; if this changed by > 20% the cell was discarded. Light flashes (0.2 mW/mm2) from a blue LED light source (Sutter Instruments) were delivered via the microscope optics and a 40x water immersion objective lens and controlled remotely using TTL pulses from Clampex. Cell responses were recorded in whole-cell mode and recorded using an Axopatch 700B amplifier connected via a digitizer to a computer with pCLAMP10 software. To stimulate ChR2 expressed in PMd neurons or axons, 5 ms pulses were delivered at inter-pulse intervals of 200 ms, 50 ms

or 25 ms for 5, 20 or 40 Hz optical stimulations, respectively. To assess PMd-dlPAG synaptic transmission, dlPAG neurons in the vicinity of ChR2-expressing PMd axons were patched. To isolate light-evoked EPSCs, neurons were voltage-clamped at -70 mV and pre-incubated with 10 μM bicuculline, an antagonist for $GABA_A$ receptors, for 5 minutes before recording. To block AMPA receptor-mediated EPSCs, 20 μM cyanquixaline (CNQX, 6-cyano-7-nitroquinoxaline-2,3-dione) was applied in the bath. The voltage-gated sodium channel blocker tetrodotoxin (TTX, 0.3 μM) was included in the bath to demonstrate action potential-dependent ChR2-mediated transmitter release. To examine direct (monosynaptic) release of glutamate by PMd axons to dlPAG neurons, EPSCs were measured in the presence of TTX and the voltage-gated K+ channel blocker 4-aminopyridine (4AP, 500 μM) for enhancing ChR2-mediated depolarization of terminals. 5 μM CNO was applied in the bath to stimulate Gq-DREADD hM3Dq or Gi-DREADD hM4Di expressed in PMd neurons. In some cases, 1 mg/ml biocytin (Tocris, 3349) was added to the intracellular solution to subsequently visualize patched neurons.

Immunohistochemistry (IHC) for acute sections. 300 μm fresh brain slices were placed into 10% buffered formalin overnight at 4°C and processed as follows for IHC. Sections were washed 3 times in 0.1 M PBS with 2% Triton-X 100 for five minutes each, and then incubated in a blocking solution containing 10% NGS in 0.1 M PBS with 1% Triton-X 100 for 1 hr at room temperature with gentle agitation. Sections were then incubated with streptavidin conjugated Alexa 647 (1:250) diluted in 0.1 M PBS with 0.4% Triton-X 100 for overnight at 4°C. The sections were rinsed 3 times in 0.1 M PBS for 10 minutes each before being mounted on microscope slides in fluoromount-G. Images were obtained with the confocal microscopy using a commercial confocal laser scanning microscope (FV1000, Olympus).

Behavior video capture. All behavior videos were captured at 30 frames/sec in standard definition (640x480) using a Logitech HD C310 webcam. To capture fiber-photometry

synchronized videos, both the calcium signal and behavior were recorded by the same computer using custom Matlab scripts that also collected timestamp values for each calcium sample/behavioral frame. These timestamps were used to precisely align neural activity and behavior.

Chemogenetics. Mice used for chemogenetic experiments were exposed to each threat and control stimuli twice, once following treatment with saline and once following treatment with CNO (5 mg/kg, injected intraperitoneally) 40 minutes prior to the experiment. Only one control or threat-exposure assay was performed per day with each mouse.

Rat exposure assay (Chapter 1). We used a corridor measuring (35 x 20 x 22 cm). At the end of the corridor there is a vertical wall with a wire mesh (with 1 cm x 1 cm square spaces in the mesh). Mice can use the mesh as a ladder to climb the vertical wall (22 cm height) and access a burrow. Mice were acclimated to this environment for three days for 10 minutes. Mice freely explored and independently climbed up the grid ladder. By the end of ten-minute acclimation mice climbed the ladder on their own without being touched by the experimenter's hand. The next day they were exposed either to a toy rat or a live rat for 20 minutes. The rat is restrained to the corner opposite to the mesh grid by a harness attached to a string that is taped to the wall. Mice could climb to avoid the rat and hide in the burrow. After reaching the burrow mice were given 1 minute of hiding time in the burrow. They were then gently placed back in the bottom floor of the context in the same level as the rat (or toy rat). The number of climbs performed during 20 minutes was recorded. This length of 20 minutes includes the 1-minute hiding periods in the burrow.

Heated floor exposure assay. The assay was done on top of a metallic heating plate (14 x 14 cm) (Faithful Magnetic Stirrer model SH-3) that was heated at either 43°C or was at room temperature (20-25°C). A transparent box (14 x 14 x 24 cm) was placed on top of the heated

plate. A cylindrical metal mesh was placed that could be used for the mouse to climb to avoid the heat. The mouse was acclimated to this environment for three days (20-minute exposure). The next day the mouse was placed in this environment in either heated or room temperature floor. Mice climb the cylinder to avoid the heat and then go back to the heated floor as they cannot support their weight while hanging on the cylinder for extended time periods. The number of climbs performed in 20 minutes was measured. We chose 43°C because it is a temperature that caused escape climbs but that is not sufficient to cause pain or skin damage. No pain-related reactions such as paw licking were observed in any of the mice.

Carbon Dioxide exposure assay. Animals were placed in a similar transparent box as the heated floor assay. Mice were acclimated to the environment for three days (10 minutes exposure). The next day mice were exposed either to infusions of air or of 15% CO_2. The concentration of CO_2 was measured and dynamically adjusted by the ProCO_2 120 controller (Biospherix, Parish, NY, USA) so that CO_2 levels are maintained at 15%. This concentration of CO_2 elicited escape jumps in all mice tested. The number of escape jumps in 10 minutes was recorded.

Heated floor pain sensitivity assay. We used the same apparatus described for the Heated floor exposure assay above. For this assay the floor was heated at 55^{o}C, which is sufficient to cause pain-related reactions in most mice (paw licking or jumping) within one minute. The latency to display a pain-related reaction was recorded. All mice showed pain responses within 30 seconds.

Rat Exposure Assay (Chapter 2). Mice were accustomed to handling prior to any behavioral assay. On day 1, mice were habituated to a rectangular box (70 cm length, 26 cm width, 44 cm height) for 20 minutes. This environment consisted of a large aquarium made of glass. Sheets of

paper lined the outside glass surface. The box was cleaned with ethanol between mice. Twenty-four hours later, mice were exposed to the same environment but in the presence of a toy rat for 20 minutes. Mice were then exposed to an adult rat or a toy rat in this environment on the two following days. The rat was secured by a harness tied to one of the walls and could freely ambulate only within a short radius of approximately 20 cm. The mouse was placed near the wall opposite to the rat and freely explored the context for 20 minutes. No separating barrier was placed between the mouse and the rat, allowing for close naturalistic encounters that can induce a variety of robust defensive behaviors.

Contextual Fear Conditioning Test. To better evaluate a broader species-specific defense repertoire in face of a conditioned stimulus, we used a modified version of the standard contextual fear conditioning method (Schuette et al. 2020). Pre-shock, fear conditioning and retrieval sessions were performed in a context (70 cm length x 17 cm width x 40 cm height) with an evenly distributed light intensity of 40 lux and a Coulbourn shock grid (19.5 cm x 17 cm) set at the extreme end of the enclosure. The fear conditioning environment is made of laminated white foam board. The box was cleaned with ethanol between mice. Forty-eight hours after rat exposure, mice were habituated to this context and could freely explore the whole environment for 20 minutes. On the following day, the grid was activated, such that a single 0.7 mA foot shock was delivered for 2 seconds only on the first time the mouse fully entered the grid zone. Twenty-four hours later, retrieval sessions were performed in the same enclosure but without shock. Mice could freely explore the context for 20 minutes during pre-shock habituation, fear conditioning and retrieval sessions.

Light Delivery for optogenetics. For PMd-cck ChR2 mice, blue light was generated by a 473 nm laser (Dragon Lasers, Changchun Jilin, China) at 4.5 mW unless otherwise indicated. Light power was decreased to 2 mW in the nose poke assay to avoid overt escape behaviors. For

Figure S7 5 mW was used. For Figure S6G we used 0.5, 2 and 7 mW to test a wide variety of light powers to study dlPAG-induced escape in the upwards step box. Green light was generated by a 532 nm laser (Dragon Lasers), and bilaterally delivered to mice at 10 mW. A Master-8 pulse generator (A.M.P.I., Jerusalem, Israel) was used to drive the blue laser at 20 Hz. This stimulation pattern was used for all ChR2 experiments. The laser output was delivered to the animal via an optical fiber (200 μm core, 0.22 numerical aperture, Doric Lenses, Canada) coupled to the fiberoptic implanted on the animals through a zirconia sleeve.

Escape from custom-built contexts. All measurements are written as length x width x height in cm. In the empty box assay mice were placed in an empty open field (46 x 46 x 36 cm). Mice were unable to escape from the empty open field as the walls are too high to be jumped over. In the rope climb assay a climbing rope was attached to the same open field used in the empty box assay, connecting the floor to the top of the wall. In the upwards climb assay the rope was removed and an escape path using plastic blocks was placed in the open field. For the rope climb and upwards climb assays the final step in the escape required jumping from the top of the open field (36 cm high) to the floor. For the downwards escape assay blocks were arranged in a staircase-type pattern, and required a jump to exit the last block and land on the floor. The last block was 20 cm higher than the floor. For all escapable assays, a successful escape was recorded only when the mouse was no longer present in the context at the end of 5 minutes. The animals had no habituation, familiarization or training in any of these assays prior to the experiments. For the inescapable empty box, blue light stimulation to PMd-cck mice expressing cre-dependent YFP or ChR2 was done in alternating 3 minute light ON and OFF epochs for a total of 9 minutes (total of 1 ON and 2 OFF epochs). In all other escape assays, blue light stimulation was done in alternating 30 seconds light ON and OFF epochs (total of five ON and five OFF epochs).

Nose-poke assay. An Arduino board was programmed to trigger 20 Hz 5ms laser trains (473 nm, Dragon Lasers) continuously, unless PMd-cck mice expressing ChR2 nose-poked into a port. Pokes were detected by an infrared beam break sensor (Adafruit, cat# 2168, New York City. NY, USA) that is coupled to the Arduino board. When a beam break occurs due to a nose poke the Arduino board halts triggering laser pulses for 5 seconds. Nose poke times were outputted by the Arduino board to a desktop running Coolterm (https://freeware.the-meiers.org/) to record arduino time point outputs.

Place aversion test. Mice were placed in a two-chamber context (20 x 42 x 27 cm) for 10 minutes to freely explore the environment. Both chambers are identical. During the next 10 minutes blue light was delivered to the PMd of cck-cre mice expressing either ChR2 or YFP (20 Hz 5ms pulses, 4.5 mW) when they entered one of the chambers. The chamber preferred by the animal during baseline exploration was chosen as the stimulated chamber. Laser stimulation was only delivered during exploration of the simulation chamber. Following 10 minutes of rest in the home cage mice were reintroduced to the context for 10 minutes to measure if PMd stimulation conditioned aversion to the stimulated chamber. The amount of time mice explored both chambers was tracked across all three epochs (baseline, stimulation and post-stimulation epochs).

Pupil size measurements. Pupil size was measured with the same set up and methods described previously (Lovett-Barron et al. 2017). Briefly, a camera (AVT Manta, G-032B) coupled to a24 mm/F1.4 lens was used to image the eye under infrared illumination (Thorlabs M780F2). Video was acquired at 60 Hz using pymba, a Python wrapper for AVT camera control. Frame acquisition times and the behavioral task were synchronized with a National Instruments DAQ (NI PCIe-6323). Pupil size was measured from the video using custom-written Matlab scripts. Each trial lasted 30 seconds. Blue light was delivered to the PMd at 20 Hz, 5ms pulses for 10 seconds following a 10 second baseline recording. Another 10 seconds were recorded post-stimulation.

Respiratory and heart rate measurements. Respiratory rate and heart rate were measured with pulse oximetry as described elsewhere (Adhikari et al. 2015) (MouseOx Plus; Starr Life Sciences, Alllison Park, PA, USA). Data was collected on a computer with MouseOx Plus software. Mice were shaved in the area surrounding the neck and acclimated to moving with the collar sensor used to by the pulse oximeter for four days. Additionally, mice were handled for three days prior to experimenting. Respiratory rate was recorded as a moving average of 10 measurements recorded at 1 Hz. Heart rate was recorded as a moving average of 5 heart beats. Recordings were obtained in head-fixed mice under very light (0.2%) isoflurane anesthesia to avoid motion artifacts in the signal.

Cat Exposure Test for fos expression. The experimental apparatus was made of clear Plexiglas and consisted of a 20 × 30 × 40 cm home cage connected to another 40 × 30 × 40 cm chamber (the food compartment) by a hallway that was 10 cm wide, 25 cm long, and 25 cm high. Between the home cage and the hallway, there was a sliding door that remained closed most of the time, except when the animals were enabled to explore the rest of the apparatus. For 10 days before the cat exposure, each animal was isolated and remained in the home cage. During the middle of the light phase, the home cage door was opened, and the animals were allowed to explore the rest of the apparatus and obtain food pellets stored in the food compartment (habituation). On the 11th day, a neutered 2-year-old male cat was placed and held in the food compartment by an experimenter as the mouse's home cage door was opened, and the animals were exposed for 10 minutes to the cat. Animals exposed to the cat presented clear innate defensive responses: at the beginning of the test, they explored the apparatus, presenting clear risk assessment responses, and the animals immediately fled back to the home cage, where they largely stayed frozen for the remainder of the test. The control group was handled identically as the cat-exposed group, but on the 11th day, the food compartment was empty, and the mice were not exposed to

the cat. No food pellets were offered during the test period. Ninety minutes after ending the behavioral testing, the animals were deeply anesthetized with sodium pentobarbital (Cristalia; Itapira, SP, Brazil; 40 mg/kg, i.p.), and the brains were processed for histology and Fos immunohistochemistry

Rat Exposure Test for fos expression. The experimental protocol was very similar to the cat exposure test. In brief, instead of the cat, we used two male adult Long-Evans rats with their bedding in the food compartment. The mice also displayed innate defensive behaviors and they were perfused ninety minutes after ending the behavioral test. Since the behavioral apparatus and procedures were the same for the cat and rat exposure test, the control group (already described) was used as reference for both experimental groups.

Hypercapnia Test for fos expression. For this test, after being habituated during 10 days in the hypercapnia box under room air conditions (0.04% CO_2, 21% O_2), the mice were submitted to hypercapnia conditions (15% CO_2, 21% O_2) for 10 minutes. The control group was just exposed to room air conditions. The animals were perfused ninety minutes after the test.

Fos Immunohistochemistry and Histology. Animals were perfused and the brains later frozen and cut on a sliding microtome in the frontal plane. One series of sections was processed for immunohistochemistry with anti-Fos antiserum raised in rabbit (c-fos(Ab-5); EMD Millipore;#PC38) at a dilution of 1:20 000. The primary antiserum was detected using a variation of the avidin–biotin complex system. In brief, sections were incubated for 90 minutes at room temperature in a solution of biotinylated goat antirabbit IgG (Vector Laboratories,#BP-9100) and then placed in the mixed avidin–biotin horseradish peroxidase complex solution (ABC Elite Kit; Vector Laboratories,#PK-6105) for the same period. The peroxidase complex was visualized by a five-minute exposure to a chromogen solution containing 0.02% 3,30 diaminobenzidine

tetrahydrochloride (DAB; Sigma) with 0.3% nickel–ammonium sulfate in 0.05 M Tris buffer (pH 7.6) followed by incubation for 20 minutes in chromogen solution with hydrogen peroxide (1:3000), which produced a blue–black product. The reaction was stopped by extensive washing in 0.02 M KPBS (pH 7.4). Sections were mounted on gelatin-coated slides and then dehydrated and coverslipped with DPX (Sigma). An adjacent series was always stained with thionin to serve as a reference series for cytoarchitectonic purposes.

Quantification of Fos-Labeled Cells. The density of Fos immunoreactive neurons was evaluated by an observer without knowledge of the animal's experimental group. Images were generated for selected regions using the 10x objective of a Nikon Eclipse 80i (Nikon Corporation, ChiyodaKu, Tokyo-To, Japan) microscope equipped with a Nikon digital camera DXM1200F (Nikon Corporation). To quantify the density of Fos labeling, we first delineated the borders of the selected regions in a given section as defined in adjoining Nissl stained sections. Fos-labeled cells were then counted therein. Only darkly labeled oval nuclei that fell within the borders of a region of interest were counted. The density of Fos labeling was determined by dividing the number of Fos-immunoreactive cells by the area of the region of interest. Both cell counting and area measurements were performed with the aid of a computer program (Image-Pro Plus, version 4.5.1; Media Cybernetics, Silver Spring, MD, USA). Cell densities were obtained on both sides of the brain and averaged for each mouse. The brain regions examined in the present investigation followed the Brain Maps: Structure of the Rat Brain.

Miniscope video capture. All videos were recorded at 30 frames/sec using a Logitech HD C310 webcam and custom-built head-mounted UCLA miniscope (Cai et al. 2016). Open-source UCLA Miniscope software and hardware (http://miniscope.org/) were used to capture and synchronize neural and behavioral video (Cai et al. 2016).

Retrobead tracing. Retrobeads (LumaFluor) (30 nL) were injected in the dlPAG diluted 6 times using a 10 µl nanofil syringe (World Precision Instruments) at 40 nl/min. The syringe was coupled to a 33-gauge beveled needle, and the bevel was placed to face the anterior side of the animal. The syringe was slowly retracted 20 minutes after the start of the infusion.

Fiber photometry. Photometry was performed as described in detail previously (C. K. Kim et al. 2016). Briefly, we used a 405-nm LED and a 470-nm LED (Thorlabs, M405F1 and M470F1) for the Ca^{2+}-dependent and Ca^{2+}independent isosbestic control measurements. The two LEDs were bandpass filtered (Thorlabs, FB410-10 and FB470-10) and then combined with a 425-nm longpass dichroic mirror (Thorlabs, DMLP425R) and coupled into the microscope using a 495-nm longpass dichroic mirror (Semrock, FF495-Di02-25 ×36). Mice were connected with a branched patch cord (400 µm, Doric Lenses, Quebec, Canada) using a zirconia sleeve to the optical system. The signal was captured at 20 Hz (alternating 405-nm LED and 470-nm LED). To correct for signal artifacts of a non biological origin (i.e. photobleaching and movement artifacts), custom Matlab scripts leveraged the reference signal (405-nm), unaffected by calcium saturation, to isolate and remove these effects from the calcium signal (470-nm).

Fiber Photometry behavior-triggered averaging. To plot the behavior-triggered averages, only mice that displayed a minimum of three behavioral instances were included in the corresponding behavioral figure. Moreover, event-triggered averages were only calculated from behavioral instances that were separated from other classified behavioral instances by a minimum of 5 seconds.

Perfusion and histological verification. Mice were anesthetized with Fatal-Plus and transcardially perfused with phosphate buffered saline followed by a solution of 4% paraformaldehyde. Extracted brains were stored for 12 hs at 4°C in 4% paraformaldehyde. Brains were then placed in sucrose for a minimum of 24 hs. Brains were sectioned in the coronal plane in a cryostat, washed in phosphate buffered saline and mounted on glass slides using PVA-DABCO. Images were acquired using a Keyence BZ-X fluorescence microscope with a 10 or 20X air objective.

QUANTIFICATION AND STATISTICAL ANALYSIS

Behavioral quantification. To extract the pose of freely-behaving mice in the described assays, we implemented DeepLabCut (Nath et al. 2019), an open-source convolutional neural network-based toolbox, to identify mouse nose, ear and tailbase xy-coordinates in each recorded video frame. These coordinates were then used to calculate velocity and position at each timepoint, as well as classify behaviors such as climbs, jumps, escape runs and freezes in an automated manner using custom Matlab scripts. Specifically:

Rat Assay (Chapter 1):

'Climbs' were classified as epochs for which (1) the vertical speed of the mouse nose and tailbase exceeded 2 cm/s, as this threshold correctly identified all empirically observed climbs, and (2) the start and end points of these epochs, defined by mouse nose coordinates, were respectively below and above an experimenter-defined climbing area bounding box.

'Escape runs' were defined as epochs for which (1) the mouse was not located in the upper burrow or ladder area and (2) the mouse speed away from the rat or toy rat exceeded 2 cm/s. As there was little room for acceleration between the rat and opposite wall, the speed threshold was set to this relatively low value.

'Stretch-attend postures' were defined as epochs for which (1) the distance between mouse nose and tailbase exceeded a distance of approximately 1.2 mouse body lengths and (2) mouse tailbase speed fell below 1 cm/s.

Heated Plate and CO_2:

'Climbs' were identified as epochs for which (1) the vertical speed of the mouse nose and tailbase coordinates both exceeded 2 cm/s within an experimenter-defined cylindrical mesh bounding box, and fell below 10 cm/s to exclude higher velocity jumps, and (2) the start and end points of these epochs, defined by mouse nose and tailbase coordinates, were respectively below and above the lower edge of this bounding box.

CO_2:

'Jumps' were identified as epochs for which (1) the vertical speed of the mouse nose and tailbase exceeded 15 cm/s and (2) the start and end points of these epochs, defined by mouse nose and tailbase coordinates, were respectively below and above an experimenter-defined bounding box of the enclosure floor.

'Escapes' were defined as epochs for which (1) the mouse speed away from the threat or control threat exceeded 2 cm/s (As there was little room for acceleration between the threat zone and opposite wall, the speed threshold was set to this relatively low value.), (2) movement away from the threat was initiated at a minimum distance-from-threat of 30 cm and (3) the distance traversed from escape onset to offset was greater than 10 cm. Thus, escapes were required to begin near the threat and lead to a substantial increase in distance from the threat.

'Pauses' were defined as periods for which mouse tailbase speed fell below 1 cm/s for at least 0.33 s.

'Freezes' were defined as periods for which mouse nose and tailbase speed fell below 0.25 cm/s for at least 0.33 s (Schuette et al. 2020).

Rat Assay (Chapter 2) and Fear Conditioning Assay:

'Escape speed' was defined as the average speed from escape onset to offset.

'Escape angle' was defined as the cosine of the mouse head direction in radians, such that the values ranged from -1 (facing towards the threat) to 1 (facing away from the threat). Mouse head direction was determined by the angle of the line connecting a point midway between the ears and the nose.

'Approaches' were defined as epochs for which (1) the mouse speed towards the threat or control threat exceeded 2 cm/s, and (2) the distance traversed from approach onset to offset was greater than 10 cm.

'Walks' were defined as epochs for which (1) movements along the safe wall of the enclosure, perpendicular to the threat, exceeded 2 cm/s and (2) the distance traversed from walk onset to offset was greater than 5 cm.

‘Freezes’ and ‘stretches’ were defined as described above.

All behaviors were manually checked by the experimenters for error.

Miniscope postprocessing. The open-source UCLA miniscope analysis package (https://github.com/daharoni/Miniscope_Analysis) (Aharoni and Hoogland 2019) was used to

motion correct miniscope videos. They were then temporally downsampled by a factor of four and spatially downsampled by a factor of two. The cell activity and footprints were extracted using the open-source package Constrained Nonnegative Matrix Factorization for microEndoscopic data (CNMF-E; https://github.com/zhoupc/CNMF_E) (Zhou et al. 2018; Schuette et al. 2020). Only cells whose variance was greater than or equal to 25% of the maximum variance among non-outliers were used in the analysis.

Neural state identification. A Hidden Markov Model (HMM) was used to identify escape-related states from the neural data in an unsupervised manner (For the code, see 'Expectation-Maximization for HMMs using real-values Gaussian observations' at Zoubin Ghahramani's code base: http://mlg.eng.cam.ac.uk/zoubin/software.html). This unsupervised approach identifies 'hidden states,' or states that are strongly represented in the neural data, without any additional information about animal behavior. We implemented the model by specifying either two or six of these 'hidden states.' The state with the most corresponding escapes was labelled the 'escape state.' All sessions for each assay were concatenated, and accuracy was calculated as the percent of escape indices to co-occur with this escape state. To determine chance level, we built a bootstrapped distribution of accuracies (1000 iterations), randomly selecting indices (the same number as escape indices) and calculating the percent that co-occurred with the escape cluster by chance. Chance level was defined as the 95th percentile of the resulting distribution.

To determine whether the HMM results agree with those of other unsupervised techniques, we also implemented k-means clustering to identify escape-related clusters in the neural data. We used the *k*-means algorithm (*k*=2) to cluster the top principal components of the neural data (accounting for >=80% of the total variance). The escape cluster, escape prediction accuracy, and chance accuracy were calculated as described above for the HMM analysis.

Behavior decoding using PMd neural data. Discrete classification of escape behavior was performed using multinomial logistic regression. Timepoints following escape by 2 seconds were labelled 'escape,' and a matched number of non-escape timepoints were randomly selected for training and validation. Each time point was treated as an individual data point. Training and validation were performed using 5-fold cross-validation, with a minimum of 10 seconds between training and validation sets. As equal numbers of escape and non-escape samples were used to build the training and validation sets, chance accuracy was 50%. Sessions with less than 5 escapes were excluded from the analysis. The same analysis was performed for approach, stretch-attend postures, and freeze. To predict escape at negative time lags from behavior onset, the same analysis procedure was implemented, using 2-second epochs preceding escape by 2, 4, 6, 8 and 10 seconds.

Behavior cell classification. We used a generalized linear model (GLM) to identify cells that showed increased calcium activity during approach, stretch-attend, escape and freeze behaviors. We fit this model to each cell's activity, with behavior indices as the predictor variable and behavior coefficients as the measure of fit. Behavior onset times were then randomized 100 times and a bootstrap distribution built from the resulting GLM coefficients. A cell was considered a behavior-categorized cell if its coefficient exceeded 95% of the bootstrap coefficient values.

Calcium peak identification. For calcium data preceding and following escape by 10 seconds, peaks were identified as samples that were larger than their neighboring samples by a specified amount (Matlab function 'findpeaks' with 'MinPeakProminence' set to 0.4).

Dual photometry correlation analysis. The nonparametric Spearman method was used to correlate the session length PMd/dlPAG and PMd/amv fiber photometry signals in threat and control assays.

Speed cell classification. Speed cells were classified using the method described in (Iwase, Kitanishi, and Mizuseki 2020). Briefly, we calculated the Pearson product-moment correlation coefficient between each cell's firing rate and the animal's running speed. The chance distribution was determined using a shuffling procedure whereby the calcium data was time-shifted in a circular manner relative to speed by a random duration between 30s and the total duration of the assay minus 30s. This was repeated 100 times for each cell. Thus, a cell was categorized as a 'speed cell' if the absolute value of its Pearson product-moment correlation exceeded the 95th percentile of distribution of speed scores from the chance distribution of all cells recorded in the PMd. Escape speed cells were classified in an identical manner, using only timepoints classified as escape.

Position and speed decoding. To predict position and speed from neural data, the data dimensionality was reduced by principal component analysis, such that the top principal components, representing at least 80% of the total variance, were used in the following decoding analysis. This output and the related position/speed data were then separated into alternating 60s training and testing blocks, with 10s of separation between blocks. Odd blocks were used to train a generalized linear regression model (GLM; Matlab function 'glmfit') and withheld even blocks were used to test the resulting model. Accuracies of this withheld testing block were reported as mean squared error. The level of chance error was calculated as the mean testing error of the GLM on circularly permuted data (100 iterations per session) across animals.

Mutual information analyses. Mutual information is an information theory-derived metric reflecting the amount of information obtained for one variable by observing another variable. In the case of the fiber photometry analysis, the related variables were the simultaneously-recorded PMd and dlPAG signals. Mutual information was calculated using custom Matlab code (Delpiano 2021) for all samples where the speed was greater than 1 cm/s. Calculating mutual information requires computing the joint distribution over the PMd and dlPAG fiber photometry signals. This distribution was calculated using a histogram count after discretizing PMd and dlPAG fiber photometry signals each into 20 bins. The same approach was used for the miniscope mutual information analysis, for which this metric was computed for all escape samples between the calcium signal of individual PMd-cck cells and speed.

Immunostaining for cfos. Fixed brains were kept in 30% sucrose at 4°C overnight, and then sectioned on a cryostat (40 µm) slices. Sections were washed in PBS and incubated in a blocking solution (3% normal donkey serum and 0.3% triton-x in PBS) for 1 hour at room temperature. Sections were then incubated at 4oC for 12 hours with polyclonal anti-fos antibody made in rabbit (1/500 dilution) (c-Fos (9F6) Rabbit mAb CAT#2250, Cell Signalling Technology) in blocking solution. Following primary antibody incubation sections were washed in PBS 3 times for 10 minutes, and then incubated with anti-rabbit IgG (H+L) antibody (1/500 dilution) conjugated to Alexa Fluor 594 (red) (CAT# 8889S, cellsignal.com) for 1 hour at room temperature. Sections were washed in PBS 3 times for 10 minutes, incubated with DAPI (1/50000 dilution in PBS), washed again in PBS and mounted in glass slides using PVA-DABCO (Sigma).

Functional Magnetic Resonance Imaging (fMRI) methods

Participants. This study included 48 adult participants (mean ± SD age: 25.1 ± 7.1; 27 male, 21 female; 7 left-handed; 40 white and 8 non-white (1 Hispanic, 5 Asian, 1 Black and 1 American

Indian)). All participants were healthy, with normal or corrected to normal vision and normal hearing, and with no history of psychiatric, physiological or pain disorders and neurological conditions, no current pain symptoms and no MRI contraindications. Eligibility was assessed with a general health questionnaire, a pain safety screening form and an MRI safety screening form. Participants were recruited from the Boulder/Denver Metro Area. The institutional review board of the University of Colorado Boulder approved the study, and all participants provided written informed consent.

Experimental Paradigm. Participants received five different types of aversive stimulation (mechanical pain, thermal pain, aversive auditory, aversive visual, and pleasant visual), each at four stimulus intensities. 24 stimuli of each type (6 per intensity) were presented over six fMRI runs in random order. Following stimulation on each trial, participants made behavioral ratings of their subjective experience. Participants were instructed to answer the question 'How much do you want to avoid this experience in the future?'. Ratings were made with a non-linear visual analog rating scale, with anchors 'Not at all' and 'Most' displayed at the ends of the scale.

Stimuli. Visual stimulation was administered on the MRI screen and included normed images from the International Affective Picture System (IAPS) database (Lang, Bradley, and Cuthbert 2008). To induce four 'stimulus intensity levels' we selected four groups of 7 images based on their normed aversiveness ratings (averaged across male and female raters) available in the IAPS database and confirmed by *N* = 10 lab members (5 male, 5 female) in response to 'How aversive is this image? 1-100'. Selected images included photographs of animals (n=7), bodily illness and injury (n=12), industrial and human waste (n=9). Four stimulus levels were delivered to participants for 10 sec each.

MRI data acquisition and preprocessing. Whole-brain fMRI data were acquired on a 3T Siemens MAGNETOM Prisma Fit MRI scanner at the Intermountain Neuroimaging Consortium

facility at the University of Colorado, Boulder. Structural images were acquired using high-resolution T1 spoiled gradient recall images (SPGR) for anatomical localization and warping to standard MNI space. Functional images were acquired with a multiband EPI sequence (TR = 460 ms, TE = 27.2 ms, field of view = 220 mm, multiband acceleration factor = 8, flip angle = 44°, 64 × 64 image matrix, 2.7 mm isotropic voxels, 56 interleaved slices, phase encoding posterior >> anterior). Six runs of 7.17 mins duration (934 total measurements) were acquired. Stimulus presentation and behavioral data acquisition were controlled using Psychtoolbox.

FMRI data were preprocessed using an automated pipeline implemented by the Mind Research Network, Albuquerque, NM. Briefly, the preprocessing steps included: distortion correction using FSL's top-up tool (https://fsl.fmrib.ox.ac.uk/fsl/), motion correction (affine alignment of first EPI volume (reference image) to T1, followed by affine alignment of all EPI volumes to the reference image and estimation of the motion parameter file (sepi_vr_motion.1D, AFNI, https://afni.nimh.nih.gov/), spatial normalization via subject's T1 image (T1 normalization to MNI space (nonlinear transform), normalization of EPI image to MNI space (3dNWarpApply, AFNI, https://afni.nimh.nih.gov/), interpolation to 2 mm isotropic voxels and smoothing with a 6 mm FWHM kernel (SPM 8, https://www.fil.ion.ucl.ac.uk/spm/software/spm8/).

Prior to first level (within-subject) analysis, we removed the first four volumes to allow for image intensity stabilization. We also identified image-wise outliers by computing both the mean and the standard deviation (across voxels) of intensity values for each image for all slices to remove intermittent gradient and severe motion-related artifacts (spikes) that are present to some degree in all fMRI data.

fMRI data analysis. Data were analyzed using SPM12 (http://www.fil.ion.ucl.ac.uk/spm) and custom MATLAB (The MathWorks, Inc., Natick, MA) code available from the authors' website (http://github.com/canlab/CanlabCore). First-level general linear model (GLM) analyses were

conducted in SPM12. The six runs were concatenated for each subject. Boxcar regressors, convolved with the canonical hemodynamic response function, were constructed to model periods for the 10-second stimulation and 4-7 second rating periods. The fixation cross epoch was used as an implicit baseline. A high-pass filter of 0.008 Hz was applied. Nuisance variables included (a) “dummy” regressors coding for each run (intercept for each run); (b) linear drift across time within each run; (c) the six estimated head movement parameters (x, y, z, roll, pitch, and yaw), their mean-centered squares, their derivatives, and squared derivative for each run (total 24 columns); and (d) motion outliers (spikes) identified in the previous step. A “single-trial model” was used to uniquely estimate the response to every stimulus in order to assess functional connectivity.

Functional connectivity analysis. Functional connectivity between the hypothalamus and PAG was estimated using Partial Least Squares (PLS) (Wold, Sjöström, and Eriksson 2001) regression, which identifies latent multivariate patterns that maximize the covariance between two blocks of data (i.e., BOLD activity in hypothalamus and PAG voxels). Here, data comprised single trial estimates of brain activation in response to aversive thermal, mechanical, auditory, and visual stimuli, in addition to a set of pleasant visual stimuli which were used as a control. For the PLS model, the predictor block of variables included all voxels in an anatomically defined mask of the hypothalamus (Pauli, Nili, and Tyszka 2018) (337 voxels) and the outcome block included all voxels in the PAG (Kragel et al. 2019) (42 voxels). Localization of the hypothalamus signal that covaries with the PAG responses was performed by bootstrapping the PLS regression and examining the distribution of PLS regression coefficients and their deviation from zero (using normal approximation for inference). Hyperalignment of fMRI data (Haxby et al. 2011) was conducted separately for each region as a preprocessing step, and leave-one-subject-out cross-validation was performed to estimate the strength of functional connections (i.e., the Pearson

correlation between the first ‘X score’ and ‘Y score’ estimated by PLS, similar to the canonical correlation (Hardoon, Szedmak, and Shawe-Taylor 2004).

A benefit of the pathway-identification model we employed is that it can, in principle, identify HTH and PAG patterns that distinctly participate in the HTH-PAG pathway. For example, the central nucleus of the amygdala (CeA) projects to both the hypothalamus and the PAG (E. J. Kim et al. 2013), and could indirectly explain variation in BOLD signals in the PAG. To test pathway specificity, we separately modeled a pathway between the CeA and the PAG using the approach described above. This allowed us to evaluate how much variation in PAG activity the HTH-PAG pathway explained above and beyond the CeA-PAG pathway. To evaluate this, we computed the partial correlation between latent sources in the hypothalamus and PAG, controlling for the latent source in the CeA.

Statistics. Nonparametric Wilcoxon signed-rank or rank-sum tests were used, unless otherwise stated. Two-tailed tests were used throughout with $\alpha=0.05$. Non-parametric tests were used because normality tests are severely underpowered for $n<100$, indicating that, with small n, normality tests will often fail to detect non-normal distributions (Razali, Wah, and Others 2011). However, by necessity rodent cohorts are much smaller than n=100. Thus, to avoid unwarranted normality assumptions about our data, we used non-parametric tests. Asterisks in the Figures indicate the *p* values. Standard error of the mean was plotted in each Figure as an estimate of variation. Multiple comparisons were adjusted with the false discovery rate (FDR) method.

REFERENCES

Adhikari, Avishek, Talia N. Lerner, Joel Finkelstein, Sally Pak, Joshua H. Jennings, Thomas J. Davidson, Emily Ferenczi, et al. 2015. “Basomedial Amygdala Mediates Top-down Control of Anxiety and Fear.” *Nature* 527 (7577): 179–85.

Aguiar, Daniele Cristina, and Francisco Silveira Guimarães. 2009. “Blockade of NMDA Receptors and Nitric Oxide Synthesis in the Dorsolateral Periaqueductal Gray Attenuates Behavioral and Cellular Responses of Rats Exposed to a Live Predator.” *Journal of Neuroscience Research* 87 (11): 2418–29.

Aharoni, Daniel, and Tycho M. Hoogland. 2019. “Circuit Investigations With Open-Source Miniaturized Microscopes: Past, Present and Future.” *Frontiers in Cellular Neuroscience* 13 (April): 141.

Bassett, Joshua P., Matthew L. Tullman, and Jeffrey S. Taube. 2007. “Lesions of the Tegmentomammillary Circuit in the Head Direction System Disrupt the Head Direction Signal in the Anterior Thalamus.” *The Journal of Neuroscience: The Official Journal of the Society for Neuroscience* 27 (28): 7564–77.

Behbehani, M. M., M. R. Park, and M. E. Clement. 1988. “Interactions between the Lateral Hypothalamus and the Periaqueductal Gray.” *The Journal of Neuroscience: The Official Journal of the Society for Neuroscience* 8 (8): 2780–87.

Blanchard, D. C., G. Griebel, and R. J. Blanchard. 2001. “Mouse Defensive Behaviors: Pharmacological and Behavioral Assays for Anxiety and Panic.” *Neuroscience and Biobehavioral Reviews* 25 (3): 205–18.

Blank, D. A. 2018. “Escaping Behavior in Goitered Gazelle.” *Behavioural Processes*. https://doi.org/10.1016/j.beproc.2017.12.021.

Borelli, Karina G., Lucas Albrechet-Souza, Alessandra G. Fedoce, Denise S. Fabri, Leonardo B. Resstel, and Marcus L. Brandão. 2013. “Conditioned Fear Is Modulated by CRF Mechanisms

in the Periaqueductal Gray Columns." *Hormones and Behavior* 63 (5): 791–99.

Cai, Denise J., Daniel Aharoni, Tristan Shuman, Justin Shobe, Jeremy Biane, Weilin Song, Brandon Wei, et al. 2016. "A Shared Neural Ensemble Links Distinct Contextual Memories Encoded Close in Time." *Nature* 534 (7605): 115–18.

Canteras, Newton S., Juliana A. V. Kroon, Fabrício H. M. Do-Monte, Eloisa Pavesi, and Antonio P. Carobrez. 2008. "Sensing Danger through the Olfactory System: The Role of the Hypothalamic Dorsal Premammillary Nucleus." *Neuroscience and Biobehavioral Reviews* 32 (7): 1228–35.

Canteras, N. S., and L. W. Swanson. 1992. "The Dorsal Premammillary Nucleus: An Unusual Component of the Mammillary Body." *Proceedings of the National Academy of Sciences of the United States of America* 89 (21): 10089–93.

Carrive, P., P. Leung, J. Harris, and G. Paxinos. 1997. "Conditioned Fear to Context Is Associated with Increased Fos Expression in the Caudal Ventrolateral Region of the Midbrain Periaqueductal Gray." *Neuroscience* 78 (1): 165–77.

Carvalho-Netto, Eduardo F., Raquel C. R. Martinez, Marcus Vinicius C. Baldo, and Newton Sabino Canteras. 2010. "Evidence for the Thalamic Targets of the Medial Hypothalamic Defensive System Mediating Emotional Memory to Predatory Threats." *Neurobiology of Learning and Memory* 93 (4): 479–86.

Cezario, A. F., E. R. Ribeiro-Barbosa, M. V. C. Baldo, and N. S. Canteras. 2008. "Hypothalamic Sites Responding to Predator Threats--the Role of the Dorsal Premammillary Nucleus in Unconditioned and Conditioned Antipredatory Defensive Behavior." *The European Journal of Neuroscience* 28 (5): 1003–15.

Chou, Xiao-Lin, Xiyue Wang, Zheng-Gang Zhang, Li Shen, Brian Zingg, Junxiang Huang, Wen Zhong, Lukas Mesik, Li I. Zhang, and Huizhong Whit Tao. 2018. "Inhibitory Gain Modulation of Defense Behaviors by Zona Incerta." *Nature Communications* 9 (1): 1151.

Comoli, Eliane, Érika Renata Ribeiro-Barbosa, and Newton Sabino Canteras. 2000. "Afferent

Connections of the Dorsal Premammillary Nucleus." *The Journal of Comparative Neurology* 423 (1): 83–98.

Del-Ben, Cristina Marta, and Frederico Guilherme Graeff. 2009. "Panic Disorder: Is the PAG Involved?" *Neural Plasticity*. https://doi.org/10.1155/2009/108135.

Delpiano, J. 2021. "Fast Mutual Information of Two Images or Signals." Matlab File Exchange. 2021. https://www.mathworks.com/matlabcentral/fileexchange/13289-fast-mutual-information-of-two-images-or-signals.

Deng, Hanfei, Xiong Xiao, and Zuoren Wang. 2016. "Periaqueductal Gray Neuronal Activities Underlie Different Aspects of Defensive Behaviors." *The Journal of Neuroscience: The Official Journal of the Society for Neuroscience* 36 (29): 7580–88.

Elliott, Dominic, and Denis Smith. 1993. "Football Stadia Disasters in the United Kingdom: Learning from Tragedy?" *Industrial & Environmental Crisis Quarterly* 7 (3): 205–29.

Evans, Dominic A., A. Vanessa Stempel, Ruben Vale, Sabine Ruehle, Yaara Lefler, and Tiago Branco. 2018. "A Synaptic Threshold Mechanism for Computing Escape Decisions." *Nature*. https://doi.org/10.1038/s41586-018-0244-6.

Faturi, C. B., M. J. Rangel Jr, M. V. C. Baldo, and N. S. Canteras. 2014. "Functional Mapping of the Circuits Involved in the Expression of Contextual Fear Responses in Socially Defeated Animals." *Brain Structure & Function* 219 (3): 931–46.

Gregg, Laura C., Kwang-Mook Jung, Jessica M. Spradley, Rita Nyilas, Richard L. Suplita 2nd, Andreas Zimmer, Masahiko Watanabe, et al. 2012. "Activation of Type 5 Metabotropic Glutamate Receptors and Diacylglycerol Lipase-α Initiates 2-Arachidonoylglycerol Formation and Endocannabinoid-Mediated Analgesia." *The Journal of Neuroscience: The Official Journal of the Society for Neuroscience* 32 (28): 9457–68.

Hardaway, J. Andrew, Lindsay R. Halladay, Christopher M. Mazzone, Dipanwita Pati, Daniel W. Bloodgood, Michelle Kim, Jennifer Jensen, et al. 2019. "Central Amygdala Prepronociceptin-Expressing Neurons Mediate Palatable Food Consumption and Reward." *Neuron* 102 (5):

1088.

Hardoon, David R., Sandor Szedmak, and John Shawe-Taylor. 2004. “Canonical Correlation Analysis: An Overview with Application to Learning Methods.” *Neural Computation* 16 (12): 2639–64.

Haxby, James V., J. Swaroop Guntupalli, Andrew C. Connolly, Yaroslav O. Halchenko, Bryan R. Conroy, M. Ida Gobbini, Michael Hanke, and Peter J. Ramadge. 2011. “A Common, High-Dimensional Model of the Representational Space in Human Ventral Temporal Cortex.” *Neuron* 72 (2): 404–16.

Hedenström, Anders, and Mikael Rosén. 2001. “Predator versus Prey: On Aerial Hunting and Escape Strategies in Birds.” *Behavioral Ecology: Official Journal of the International Society for Behavioral Ecology* 12 (2): 150–56.

Heithaus, Michael R., Aaron J. Wirsing, Derek Burkholder, Jordan Thomson, and Lawrence M. Dill. 2009. “Towards a Predictive Framework for Predator Risk Effects: The Interaction of Landscape Features and Prey Escape Tactics.” *The Journal of Animal Ecology* 78 (3): 556–62.

Helbing, D., I. Farkas, and T. Vicsek. 2000. “Simulating Dynamical Features of Escape Panic.” *Nature* 407 (6803): 487–90.

Iwase, Motosada, Takuma Kitanishi, and Kenji Mizuseki. 2020. “Cell Type, Sub-Region, and Layer-Specific Speed Representation in the Hippocampal–entorhinal Circuit.” *Scientific Reports*. https://doi.org/10.1038/s41598-020-58194-1.

Jankowski, Maciej M., Kim C. Ronnqvist, Marian Tsanov, Seralynne D. Vann, Nicholas F. Wright, Jonathan T. Erichsen, John P. Aggleton, and Shane M. O’Mara. 2013. “The Anterior Thalamus Provides a Subcortical Circuit Supporting Memory and Spatial Navigation.” *Frontiers in Systems Neuroscience*. https://doi.org/10.3389/fnsys.2013.00045.

Jiang-Xie, Li-Feng, Luping Yin, Shengli Zhao, Vincent Prevosto, Bao-Xia Han, Kafui Dzirasa, and Fan Wang. 2019. “A Common Neuroendocrine Substrate for Diverse General Anesthetics

and Sleep." *Neuron*. https://doi.org/10.1016/j.neuron.2019.03.033.

Johnson, Philip L., Stephanie D. Fitz, Jacob H. Hollis, Rosario Moratalla, Stafford L. Lightman, Anantha Shekhar, and Christopher A. Lowry. 2011. "Induction of c-Fos in 'panic/defence'-Related Brain Circuits Following Brief Hypercarbic Gas Exposure." *Journal of Psychopharmacology*. https://doi.org/10.1177/0269881109353464.

Johnson, Philip L., and Anantha Shekhar. 2012. "An Animal Model of Panic Vulnerability with Chronic Disinhibition of the Dorsomedial/perifornical Hypothalamus." *Physiology & Behavior*. https://doi.org/10.1016/j.physbeh.2012.03.016.

Johnson, Philip L., William A. Truitt, Stephanie D. Fitz, Christopher A. Lowry, and Anantha Shekhar. 2008. "Neural Pathways Underlying Lactate-Induced Panic." *Neuropsychopharmacology*. https://doi.org/10.1038/sj.npp.1301621.

Keating, J. P. 1982. "The Myth of Panic." *Fire Journal* 147: 57–61.

Kim, Christina K., Samuel J. Yang, Nandini Pichamoorthy, Noah P. Young, Isaac Kauvar, Joshua H. Jennings, Talia N. Lerner, et al. 2016. "Simultaneous Fast Measurement of Circuit Dynamics at Multiple Sites across the Mammalian Brain." *Nature Methods* 13 (4): 325–28.

Kim, D. J., A. S. Lee, A. A. Yttredahl, R. Gómez-Rodríguez, and B. J. Anderson. 2017. "Repeated Threat (without Direct Harm) Alters Metabolic Capacity in Select Regions That Drive Defensive Behavior." *Neuroscience* 353 (June): 106–18.

Kim, Eun Joo, Omer Horovitz, Blake A. Pellman, Lancy Mimi Tan, Qiuling Li, Gal Richter-Levin, and Jeansok J. Kim. 2013. "Dorsal Periaqueductal Gray-Amygdala Pathway Conveys Both Innate and Learned Fear Responses in Rats." *Proceedings of the National Academy of Sciences of the United States of America* 110 (36): 14795–800.

Kobes, Margrethe, Ira Helsloot, Bauke de Vries, and Jos G. Post. 2010. "Building Safety and Human Behaviour in Fire: A Literature Review." *Fire Safety Journal* 45 (1): 1–11.

Kragel, Philip A., Marta Bianciardi, Ludger Hartley, Gordon Matthewson, Ji-Kyung Choi, Karen S. Quigley, Lawrence L. Wald, Tor D. Wager, Lisa Feldman Barrett, and Ajay B. Satpute. 2019.

"Functional Involvement of Human Periaqueductal Gray and Other Midbrain Nuclei in Cognitive Control." *The Journal of Neuroscience: The Official Journal of the Society for Neuroscience* 39 (31): 6180–89.

Krzywkowski, Piotr, Beatrice Penna, and Cornelius T. Gross. 2020. "Dynamic Encoding of Social Threat and Spatial Context in the Hypothalamus." *eLife* 9 (September). https://doi.org/10.7554/eLife.57148.

Kunwar, Prabhat S., Moriel Zelikowsky, Ryan Remedios, Haijiang Cai, Melis Yilmaz, Markus Meister, and David J. Anderson. 2015. "Ventromedial Hypothalamic Neurons Control a Defensive Emotion State." *eLife* 4 (March). https://doi.org/10.7554/eLife.06633.

Lang, Peter J., Margaret M. Bradley, and Bruce N. Cuthbert. 2008. "International Affective Picture System (IAPS): Affective Ratings of Pictures and Instruction Manual. University of Florida, Gainesville." Tech Rep A-8.

Lecca, Salvatore, Frank Julius Meye, Massimo Trusel, Anna Tchenio, Julia Harris, Martin Karl Schwarz, Denis Burdakov, Francois Georges, and Manuel Mameli. 2017. "Aversive Stimuli Drive Hypothalamus-to-Habenula Excitation to Promote Escape Behavior." *eLife*. https://doi.org/10.7554/elife.30697.

Li, Yi, Jiawei Zeng, Juen Zhang, Chenyu Yue, Weixin Zhong, Zhixiang Liu, Qiru Feng, and Minmin Luo. 2018. "Hypothalamic Circuits for Predation and Evasion." *Neuron* 97 (4): 911–24.e5.

Lovett-Barron, Matthew, Aaron S. Andalman, William E. Allen, Sam Vesuna, Isaac Kauvar, Vanessa M. Burns, and Karl Deisseroth. 2017. "Ancestral Circuits for the Coordinated Modulation of Brain State." *Cell* 171 (6): 1411–23.e17.

Lovick, T. A. 2000. "Panic Disorder-A Malfunction of Multiple Transmitter Control Systems within the Midbrain Periaqueductal Gray Matter?" *The Neuroscientist: A Review Journal Bringing Neurobiology, Neurology and Psychiatry* 6 (1): 48–59.

Malvaez, Melissa, Christine Shieh, Michael D. Murphy, Venuz Y. Greenfield, and Kate M. Wassum. n.d. "Distinct Cortical-Amygdala Projections Drive Reward Value Encoding and

Retrieval.” https://doi.org/10.1101/299958.

Martinez, Raquel C. R., Eduardo F. Carvalho-Netto, Vanessa C. S. Amaral, Ricardo L. Nunes-de-Souza, and Newton S. Canteras. 2008. “Investigation of the Hypothalamic Defensive System in the Mouse.” *Behavioural Brain Research*. https://doi.org/10.1016/j.bbr.2008.03.042.

Mendes-Gomes, Joyce, Simone Cristina Motta, Ricardo Passoni Bindi, Amanda Ribeiro de Oliveira, Farhad Ullah, Marcus Vinicius C. Baldo, Norberto Cysne Coimbra, Newton Sabino Canteras, and D. Caroline Blanchard. 2020. “Defensive Behaviors and Brain Regional Activation Changes in Rats Confronting a Snake.” *Behavioural Brain Research* 381 (March): 112469.

Motta, Simone C., Antônio P. Carobrez, and Newton S. Canteras. 2017. “The Periaqueductal Gray and Primal Emotional Processing Critical to Influence Complex Defensive Responses, Fear Learning and Reward Seeking.” *Neuroscience and Biobehavioral Reviews* 76 (Pt A): 39–47.

Nagai, Jun, Abha K. Rajbhandari, Mohitkumar R. Gangwani, Ayaka Hachisuka, Giovanni Coppola, Sotiris C. Masmanidis, Michael S. Fanselow, and Baljit S. Khakh. 2019. “Hyperactivity with Disrupted Attention by Activation of an Astrocyte Synaptogenic Cue.” *Cell* 177 (5): 1280–92.e20.

Nath, Tanmay, Alexander Mathis, An Chi Chen, Amir Patel, Matthias Bethge, and Mackenzie Weygandt Mathis. 2019. “Using DeepLabCut for 3D Markerless Pose Estimation across Species and Behaviors.” *Nature Protocols* 14 (7): 2152–76.

Pauli, Wolfgang M., Amanda N. Nili, and J. Michael Tyszka. 2018. “A High-Resolution Probabilistic in Vivo Atlas of Human Subcortical Brain Nuclei.” *Scientific Data* 5 (April): 180063.

Perusini, Jennifer N., and Michael S. Fanselow. 2015. “Neurobehavioral Perspectives on the Distinction between Fear and Anxiety.” *Learning & Memory* 22 (9): 417–25.

Razali, Nornadiah Mohd, Yap Bee Wah, and Others. 2011. “Power Comparisons of Shapiro-Wilk, Kolmogorov-Smirnov, Lilliefors and Anderson-Darling Tests.” *Journal of Statistical Modeling and Analytics* 2 (1): 21–33.

Reis, Fernando M. C. V., Jinhan Liu, Peter J. Schuette, Johannes Y. Lee, Sandra Maesta-Pereira, Meghmik Chakerian, Weisheng Wang, Newton S. Canteras, Jonathan C. Kao, and Avishek Adhikari. 2021. “Shared Dorsal Periaqueductal Gray Activation Patterns during Exposure to Innate and Conditioned Threats.” *The Journal of Neuroscience: The Official Journal of the Society for Neuroscience*, April. https://doi.org/10.1523/JNEUROSCI.2450-20.2021.

Resstel, L. B. M., S. F. Lisboa, D. C. Aguiar, F. M. A. Corrêa, and F. S. Guimarães. 2008. “Activation of CB1 Cannabinoid Receptors in the Dorsolateral Periaqueductal Gray Reduces the Expression of Contextual Fear Conditioning in Rats.” *Psychopharmacology* 198 (3): 405–11.

Sakuma, Y., and D. W. Pfaff. 1982. “Properties of Ventromedial Hypothalamic Neurons with Axons to Midbrain Central Gray.” *Experimental Brain Research. Experimentelle Hirnforschung. Experimentation Cerebrale* 46 (2): 292–300.

Schuette, Peter J., Fernando M. C. V. Reis, Sandra Maesta-Pereira, Meghmik Chakerian, Anita Torossian, Garrett J. Blair, Weisheng Wang, et al. 2020. “Long-Term Characterization of Hippocampal Remapping during Contextual Fear Acquisition and Extinction.” *The Journal of Neuroscience: The Official Journal of the Society for Neuroscience* 40 (43): 8329–42.

Shang, Congping, Zijun Chen, Aixue Liu, Yang Li, Jiajing Zhang, Baole Qu, Fei Yan, et al. 2018. “Divergent Midbrain Circuits Orchestrate Escape and Freezing Responses to Looming Stimuli in Mice.” *Nature Communications*. https://doi.org/10.1038/s41467-018-03580-7.

Shen, Jia-Quan, Xu-Wen Wang, and Luo-Luo Jiang. 2018. “The Influence of Panic on the Efficiency of Escape.” *Physica A: Statistical Mechanics and Its Applications* 491: 613–18.

Shen, Jia, Depeng Wang, Xinxing Wang, Shashank Gupta, Bhargav Ayloo, Song Wu, Paras Prasad, Qiaojie Xiong, Jun Xia, and Shaoyu Ge. 2019. “Neurovascular Coupling in the

Dentate Gyrus Regulates Adult Hippocampal Neurogenesis." *Neuron* 103 (5): 878–90.e3.

Silva, Bianca A., Camilla Mattucci, Piotr Krzywkowski, Rachel Cuozzo, Laura Carbonari, and Cornelius T. Gross. 2016. "The Ventromedial Hypothalamus Mediates Predator Fear Memory." *The European Journal of Neuroscience* 43 (11): 1431–39.

Silva, Bianca A., Camilla Mattucci, Piotr Krzywkowski, Emanuele Murana, Anna Illarionova, Valery Grinevich, Newton S. Canteras, Davide Ragozzino, and Cornelius T. Gross. 2013. "Independent Hypothalamic Circuits for Social and Predator Fear." *Nature Neuroscience* 16 (12): 1731–33.

Tovote, Philip, Maria Soledad Esposito, Paolo Botta, Fabrice Chaudun, Jonathan P. Fadok, Milica Markovic, Steffen B. E. Wolff, et al. 2016. "Midbrain Circuits for Defensive Behaviour." *Nature* 534 (7606): 206–12.

Viellard, Juliette, Marcus Vinicius C. Baldo, and Newton Sabino Canteras. 2016. "Testing Conditions in Shock-Based Contextual Fear Conditioning Influence Both the Behavioral Responses and the Activation of Circuits Potentially Involved in Contextual Avoidance." *Behavioural Brain Research* 315 (December): 123–29.

Wang, Li, Irene Z. Chen, and Dayu Lin. 2015. "Collateral Pathways from the Ventromedial Hypothalamus Mediate Defensive Behaviors." *Neuron* 85 (6): 1344–58.

Wang, Tongfei A., Chin Fen Teo, Malin Åkerblom, Chao Chen, Marena Tynan-La Fontaine, Vanille Juliette Greiner, Aaron Diaz, Michael T. McManus, Yuh Nung Jan, and Lily Y. Jan. 2019. "Thermoregulation via Temperature-Dependent PGD2 Production in Mouse Preoptic Area." *Neuron* 103 (2): 349.

Wang, Weisheng, Peter J. Schuette, Jun Nagai, Brooke Christine Tobias, Fernando Midea Cuccovia V Reis, Shiyu Ji, Miguel A. X. de Lima, et al. 2021. "Coordination of Escape and Spatial Navigation Circuits Orchestrates Versatile Flight from Threats." *Neuron*, April. https://doi.org/10.1016/j.neuron.2021.03.033.

Watson, Thomas C., Nadia L. Cerminara, Bridget M. Lumb, and Richard Apps. 2016. "Neural

Correlates of Fear in the Periaqueductal Gray." *The Journal of Neuroscience: The Official Journal of the Society for Neuroscience* 36 (50): 12707–19.

Wold, Svante, Michael Sjöström, and Lennart Eriksson. 2001. "PLS-Regression: A Basic Tool of Chemometrics." *Chemometrics and Intelligent Laboratory Systems* 58 (2): 109–30.

Woodbury, Patrick B. 1986. "The Geometry of Predator Avoidance by the Blue Crab, Callinectes Sapidus Rathbun." *Animal Behaviour* 34 (February): 28–37.

Xiong, Xiaorui R., Feixue Liang, Brian Zingg, Xu-Ying Ji, Leena A. Ibrahim, Huizhong W. Tao, and Li I. Zhang. 2015. "Auditory Cortex Controls Sound-Driven Innate Defense Behaviour through Corticofugal Projections to Inferior Colliculus." *Nature Communications*. https://doi.org/10.1038/ncomms8224.

Zhou, Pengcheng, Shanna L. Resendez, Jose Rodriguez-Romaguera, Jessica C. Jimenez, Shay Q. Neufeld, Andrea Giovannucci, Johannes Friedrich, et al. 2018. "Efficient and Accurate Extraction of in Vivo Calcium Signals from Microendoscopic Video Data." *eLife* 7 (February). https://doi.org/10.7554/eLife.28728.